UNIVERSITY OF OKLAHOMA

GRADUATE COLLEGE

MULTIPLE-STAGE INTERBAND CASCADE PHOTOVOLTAIC DEVICES USING 6.1 Å SEMICONDUCTOR MATERIALS

A DISSERTATION

SUBMITTED TO THE GRADUATE FACULTY

in partial fulfillment of the requirements for the

Degree of

DOCTOR OF PHILOSOPHY

By

ROBERT THOMAS HINKEY
Norman, Oklahoma
2013

MULTIPLE-STAGE INTERBAND CASCADE PHOTOVOLTAIC DEVICES USING 6.1 Å SEMICONDUCTOR MATERIALS

A DISSERTATION APPROVED FOR THE
DEPARTMENT OF ENGINEERING PHYSICS

BY

_____
Dr. Michael B. Santos, Chair

_____
Dr. Rui Q. Yang

_____
Dr. Kieran Mullen

_____
Dr. Sheena Q. Murphy

_____
Dr. Eric R. I. Abraham

_____
Dr. Hjalti Sigmarsson

To my parents, Thomas and Sharon Hinkey, and my brother, Peter Hinkey.

Acknowledgements

I would like to acknowledge the sources that have provided me with funding during my graduate career. In my first two years, I was partially supported by a University of Oklahoma Lin Fellowship. I was also partially supported by the Robert L. Hughes Centennial Fellowship from the Fall of the 2010 semester to the Spring of 2013. I am also grateful for funding from grants from the AFOSR (Award No. FA9550-12-1-0260) for research on mid-wave infrared detectors, the National Science Foundation (Award No. ECCS-1202318) for research on long-wavelength infrared detectors, and the Department of Energy EPSCoR program (Award No. DE-SC0004523) for basic research on interband cascasde photovoltaic devices.

I would like to thank the many individuals who made significant contributions to this work. First and foremost, I would like to thank my advisor, Prof. Rui Q. Yang. He provided me with a dissertation topic that was both interesting and heretofore unexplored. For the past six years, he has been very gracious in offering his time and engaging in many long discussions with me. It has been a privilege to learn from someone who has experience in fostering new technology from its initial conception to implementation. I would also like to thank Dr. Zhaobing Tian. I worked closely with him for several of my early years, and he was kind enough to devote much of his time in helping me get started in research. I would also like to thank Dr. Lu Li and Hao Ye who performed the material growth and fabrication for many of the devices presented in this work. During my last year I was fortunate to work closely with Hossein Lotfi. He was very helpful in carrying out characterization measurements for many devices. In addition, I had many insightful discussions with him on the nature of our research.

Debating with him was always a challenge, and these discussions helped refine many of the ideas presented in this work. I would also like to thank Lin Lei for performing some device characterization measurements. I also enjoyed personal interactions with Yuchao Jiang, SM Shazzad Rassel, and Lihau Zhao.

I am also appreciative to our group's collaborators. In particular, I would like to thank Prof. Matthew Johnson and Dr. Joel Keay for several insightful conversations and for providing our group both resources and expertise in device fabrication and material characterization. Additionally, I would also like to thank Dr. John Klem of Sandia National Laboratories who performed the MBE growth of several of the samples that are presented in this work. I would like to thank Prof. Michael Santos for chairing my committee, and for providing the resources for our group to grow our material. I also thank Profs. Kieran Mullen, Sheena Murphy, Eric Abraham, and Hjalti Sigmarsson for serving on my committee.

I am very grateful to the Homer L. Dodge Department of Physics and Astronomy for accepting me into their graduate program. The skills and knowledge I developed during the coursework in my early years were invaluable in my later years doing research. I appreciate how seriously the faculty took the responsibility of providing students with a solid foundation in physics.

Lastly, I would like to thank my parents and my brother, Peter. I have been very fortunate to be part of a family that has provided me with unconditional support over the years.

Publication List

Note that much of the work presented in this dissertation has already been disseminated in the publications marked with (*):

[1] R.Q. Yang, Z. Tian, **R.T. Hinkey**, F. Zhao, K. Mansour, C.J. Hill, and Y. Qiu, "Recent Progress in Interband Cascade Lasers with Separate Confinement Layers," Proc. SPIE **7230**, 7300S (2009).

[2] Z. Tian, **R. Hinkey**, F. Zhao, R.Q. Yang, K. Mansour, and C.J. Hill, "Interband cascade lasers with separate-confinement layers," 2008 Annual LEOS Meeting, Nov. 9-13, 2008, Newport Beach, CA, USA (pp. 749-750 in its Proceedings)

[3] Z. Tian, R. Q. Yang, T. D. Mishima, M. B. Santos, **R. T. Hinkey**, M. E. Curtis, and M. B. Johnson, "Plasmon waveguide interband cascade lasers", paper CThAA7 at The Conference on Lasers and Electro-Optics (CLEO) and the Quantum Electronics and
Laser Science Conference (QELS), Baltimore, MD, May 31-June 5, 2009.

[4] Z. Tian, R.Q. Yang, T.D. Mishima, M.B. Santos, **R.T. Hinkey**, M.E. Curtis, and M.B. Johnson, "InAs-based interband cascade lasers near 6 μm," Electron. Lett. **45**, 48-49 (2009).

[5] **R.T. Hinkey** and R.Q. Yang, "Total transmission of electrons in semiconductor heterostructures at oblique incidence," J. Appl. Phys. **106**, 073719 (2009).

[6] **R.T. Hinkey**, Z. Tian, R.Q. Yang, T.D. Mishima, and M.B. Santos, "Reflectance spectrum of plasmon waveguide interband cascade lasers and observation of the Berreman effect," J. Appl. Phys. **110**, 043113 (2011).

[7] Z. Tian, **R.T. Hinkey**, R.Q. Yang, D. Lubyshev, Y. Qiu, J.M. Fastenau, W.K. Liu, and M.B. Johnson, "InAs-based mid-infrared interband cascade lasers near 5.3 μm," J. Quantum Electron. **48**, 915-921 (2012).

[8] *Z. Tian, **R.T. Hinkey**, R.Q. Yang, J.F. Klem, and M.B. Johnson, "Mid-IR photovoltaic devices based on interband cascade structures," in *Proc. 38th IEEE Photovoltaic Spec. Conf.*, 2012, pp. 001560-001565.

[9] Y. Jiang, L. Li, Z. Tian, **R. T. Hinkey**, R. Q. Yang, T. D. Mishima, M. B. Santos, M. B. Johnson, and K. Mansour, "Room-Temperature InAs-based Interband Cascade Lasers," paper CF3K.1 at The Conference on Lasers and Electro-Optics (CLEO) and the Quantum Electronics and Laser Science Conference (QELS), San Jose, CA, May 6-11,2012.

[10] ***R.T. Hinkey**, Z.-B. Tian, S.M. Shazzad S. Rassel, R.Q. Yang, J.F. Klem, and M.B. Johnson "Interband cascade photovoltaic devices for conversion of mid-IR radiation," IEEE J. Photovolt. **3**, 745-752 (2013).

[11] R.Q. Yang, L. Li, L. Zhao, Y. Jiang, Z. Tian, H. Ye, **R.T. Hinkey**, C. Niu, T.D. Mishima, M.B. Santos, J.C. Keay, M.B. Johnson, K. Mansour, "Recent progress in development of InAs-based interband cascade lasers," Proc. SPIE **8640**, 86400Q (2013).

[12] H. Ye, L. Li, **R.T. Hinkey**, R.Q. Yang, T.D. Mishima, J.C. Keay, and M.B. Santos, "MBE growth optimization of InAs (001) homoepitaxy," J. Vac. Sci. Technol. B **31**, 03C135 (2013).

[13] H. Lotfi, **R.T. Hinkey**, L. Li, R.Q. Yang, J.F. Klem, and M.B. Johnson, "Narrow-bandgap photovoltaic devices operating at room temperature and above with high open-circuit voltage," Appl. Phys. Lett. **102**, p. 211103 (2013).

[14] ***R.T. Hinkey**, H. Lotfi, L, Lu, R. Q. Yang, J. F. Klem, J. C. Keay, M. B. Johnson, "Interband cascade thermophotovoltaic devices with type-II superlattice absorbers of ~0.4 eV bandgap," to be published in *Proc. 39th IEEE Photovoltaic Spec. Conf.*

[15] ***R.T. Hinkey** and R.Q. Yang, "Theory of multiple-stage interband photovoltaic devices and ultimate performance limit comparison of multiple-stage and single-stage interband infrared detectors," J. Appl. Phys. **114**, 104506 (2013).

[16] ***R.T. Hinkey**, H. Lotfi, L. Li, H. Ye, L. Lei, R.Q. Yang, J. Keay, T.D. Mishima, M.B. Santos, and M.B. Johnson "Interband cascade photodetectors with InAs/GaSb superlattice abosrbers," Proc. SPIE 8868, 886805 (2013).

[17] ***R.T. Hinkey** and R.Q. Yang, "Comparison of ultimate limits of interband cascade infrared photodetectors and single-absorber detectors," Proc SPIE 8868, 886804 (2013).

Table of Contents

List of Tables

List of Figures

Abstract

Interband cascade photovoltaic (IC PV) structures are an attractive alternative to the conventional long-absorber diode structures currently used for mid-infrared photovoltaic devices. The unique feature of IC PV devices is that they utilize a multiple-stage architecture. This sort of design is made possible by the type-II broken-gap alignment between InAs and GaSb. In a multiple-stage device, electrons must be excited several times by above-bandgap photons in order to pass between the device contacts. Although counterintuitive, this transport feature can be beneficial for both energy-conversion and infrared detector technology. In particular, the interband cascade approach should be useful for improving the performance of narrow-bandgap optoelectronic devices operating at high temperature by ensuring a more efficient usage of the incident photons. The aim of this dissertation is to identify and demonstrate the advantages that interband cascade photovoltaic devices offer, both theoretically and experimentally.

A theoretical framework for studying signal and noise in multiple-stage interband photovoltaic devices is presented. The theory flows from a general picture of electrons transitioning between thermalized reservoirs. Making the assumption of bulk-like absorbers, we show how the standard semiconductor transport and recombination equations can be extended to the case of multiple-stage devices. The electronic noise arising from fluctuations in the transition rates between reservoirs is derived using the Shockley-Ramo and Weiner-Khintchine theorems. This provides a unified noise treatment accounting for both the Johnson and shot noise. In this framework, we derive

consistent analytic expressions for the quantum efficiency and thermal noise in terms of the design parameters and macroscopic material properties of the absorber.

The theory is then applied in order to quantify the potential performance improvement that can be gained from the use of multiple stages. We show that multiple-stage detectors can achieve higher sensitivities for applications requiring a very fast temporal response. This is shown by deriving an expression for the optimal number of stages in terms of the absorption coefficient and absorber thicknesses for a multiple-stage detector with short absorbers. The multiple-stage architecture may also be useful for improving the sensitivity of high operating temperature detectors, if a short diffusion length limits the quantum efficiency. The potential sensitivity improvement offered by a multiple-stage architecture can be judged from the product of the absorption coefficient, α, and diffusion length, L_n, of the absorber material. For detector designs where the absorber lengths in each of the stages is equal, the multiple-stage architecture offers the potential for significant detectivity improvement when $\alpha L_n \leq 0.2$. We also explore the potential of multiple-stage detectors with photocurrent-matched absorbers. In this architecture, the absorbers are designed to absorb and collect an equal number of carriers in each stage. It is shown that for zero-bias operation, this design has a higher ultimate detectivity than a single-absorber device. Such improvements in detectivity are significant for material with $\alpha L_n \leq 0.5$. Additionally, for photocurrent-matched detectors, it is shown that when the noise is limited by the inherent fluctuations in a strong signal, the detectivity improvement possible scales with the square of the improvement in particle conversion efficiency. Using the results derived for general

values of αL_n, we offer an outlook for multiple-stage detectors that utilize InAs/GaSb superlattice absorbers.

The experimental characterization of a series of IC PV devices designed for radiative energy conversion is presented. Devices utilizing InAs/GaSb superlattice (SL) absorbers and others using InAs/$Al_{0.8}In_{0.2}Sb$/GaSb/$Al_{0.8}In_{0.2}Sb$ SL absorbers are characterized. In the latter devices, the thin layer of $Al_{0.8}In_{0.2}Sb$ enabled a wider absorber bandgap to be realized. This led to an improved efficiency at high temperature. For both sets of the devices, the power conversion efficiency is found to be limited by a low fill factor. A variable-area analysis of a series of the wider-bandgap devices revealed the devices suffered from significant surface shunting effects. This shunting is also shown to limit the open-circuit voltage.

An experimental comparison of single- and multiple-stage infrared detectors is also detailed. These detectors utilized absorbers composed of InAs/GaSb superlattices. The cutoff wavelengths of these detectors was in the mid-wave infrared. Similar to the energy-conversion devices, these detectors had dark currents limited by surface leakage effects. For the set of devices studied, it is shown that multiple-stage detectors using short absorbers are able to achieve higher values of R_oA and have a photoresponse that is less sensitive to temperature. The sensitivity of the multiple-stage devices, as characterized by the specific detectivity, exceeds that of the single-stage devices at ambient temperatures and above. This provides direct evidence of the utility of these devices for high-temperature detector operation.

Chapter 1 : Photovoltaic Conversion and Detection of Radiation

1.1 Infrared Radiation and Photovoltaic Devices

According to the laws of thermodynamics, an object with a temperature higher than that of its ambient surroundings will give off heat. This heat is often given off as radiation. When this is the case, the spectral distribution of the emitted photons is quite similar to that of an blackbody source at a temperature equivalent to that of the hot object. The net photon flux, J_γ, between a hot source at temperature T_s, and a detector at ambient temperature T_{amb} can be expressed as:

$$J_\gamma = \frac{2\pi}{h^3 c^2}\left[\int_0^\infty dE\ \varepsilon(E)\frac{E^2}{e^{E/k_b T_s}-1} - \int_0^\infty dE\ \varepsilon(E)\frac{E^2}{e^{E/k_b T_{amb}}-1}\right], \tag{1.1}$$

where ε(E) is the spectral emissivity of the object, h is Planck's constant, c is the speed of light, and k_b is Boltzmann's constant. For a given photon energy, the emissivity is a number between zero and unity. An emissivity of unity represents the pure blackbody limit. An example of an object that gives off heat with a blackbody-like emission spectrum is the Sun. The temperature of the Sun is about ~6000 K. For this blackbody temperature, most of the emitted photons fall in the visible and near-infrared regions of the spectrum. For terrestrial sources, the source temperatures are typically much lower (500 K – 2000 K). For sources with these temperatures, most of the emitted photons will be in the mid-infrared region of the spectrum (3-30 μm). This is shown in Fig. 1.1, which compares the blackbody emission spectrum for sources of different temperatures.

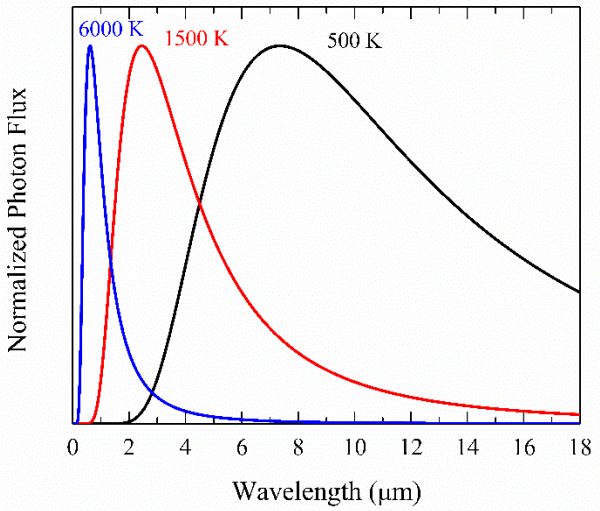

Figure 1.1: Blackbody emission spectra for sources of different temperatures

Due to the prevalence of mid-infrared radiation in the emission spectrum of terrestrial sources, the conversion of these photons to electrical current is an important technological issue [1-4]. In particular, there is significant interest in converting light with wavelengths that fall within the mid-infrared atmospheric transmission windows. One of these is in the mid-wave infrared region (MWIR) of 3-5 μm, another is the long-wave infrared (LWIR) region of 8-12 μm, and another is the very-long-wave infrared (VLWIR) region of ≥ 14 μm. Photons with energies in these spectral windows are subject to less loss from absorption and scattering. For the MWIR and LWIR regions, this can be seen in Fig. 1.2, which shows the atmospheric transmittance for light at different wavelengths. In addition, the frequencies for the fundamental rotational and vibrational modes of many molecules fall in the mid-infrared. As such, spectroscopic instruments designed to measure the concentration of certain gases can be much more sensitive with the use of infrared sources and detectors.

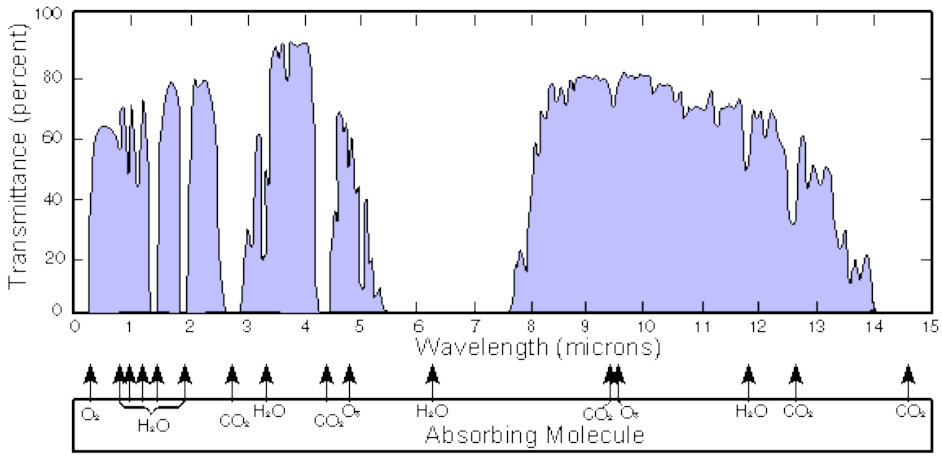

Figure 1.2: Infrared atmospheric transmittance spectrum. Figure is available in public domain and was taken from Wikipedia Commons

Photons can be efficiently converted to electrical signal using photovoltaic devices. Photovoltaic devices utilize a semiconductor structure that converts absorbed light to an electrical current and/or voltage that is measured with an external circuit connected to the semiconductor at two contacts. The structure of the semiconductor device is designed so that when operated under zero-bias, a photocurrent flows in the external circuit. When operated at zero current, a photovoltage will be observed in the external circuit. When there is a voltage across a PV device, distinct chemical potentials are established for carriers in the conduction band and carriers in the valence band for at least some portion of the absorber region. A good PV device is able to maintain a strong chemical potential splitting throughout most of the absorber region of the device.

PV devices can be used as cells for converting incident light to usable electrical power. Solar cells are the most common example of this sort of device. The conventional method for obtaining a device with a photovoltaic architecture is to introduce a doping gradient in the material. The variation of the density of the fixed dopants gives rise to a built-in electric field, in accordance with the electrostatic Poisson's equation. The most common example of this is the p-

n junction. The band diagram of a p-n homojunction structure is shown in Fig. 1.3(a). In this structure, the PV effect is enabled by the built-in electric field in the depletion region, which is void of freely moving carriers (electrons and holes). As there are no free carriers in the depletion region, there is gradient in the spatial distribution of charge due to the abrupt shift in positively charge donors on the n-side to negatively charge acceptors on the p-side. This gives rise to a localized electric field. A photocurrent at zero-bias arises when this device is illuminated due to the diffusion of generated minority carriers to the junction and their subsequent collection. The spatial dependence of the chemical potentials for conduction band carriers, F_n, and valence band carriers, F_p are shown. Note that the more rapid decrease of the chemical potential on the n-side of the junction is due to the lower diffusion length of minority holes on that side compared with that of the minority electrons on the p-side. As seen in in Chapter 3, signal is produced in the external circuit whenever an electron changes its chemical potential.

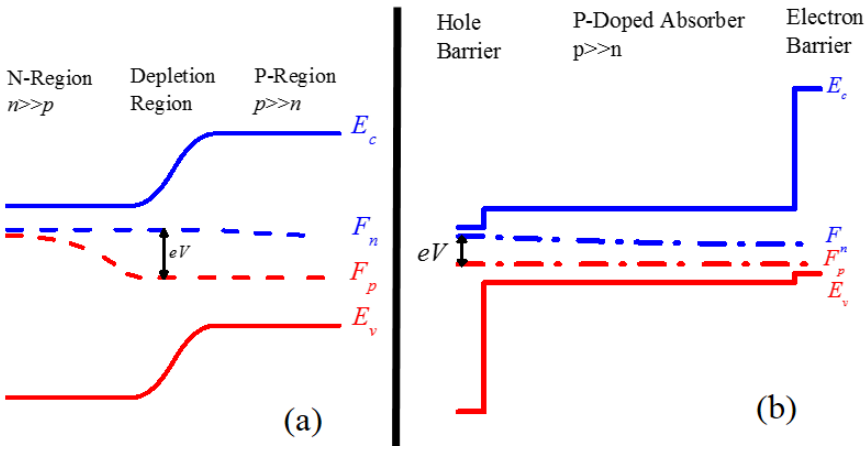

Figure 1.3: Band diagrams of two different photovoltaic structures under a forward bias. The solid lines indicate the conduction and valence band edges of the material. (a) Band diagram of p-n junction. In (b) a diagram of a "heterostructure diode" is shown. In this case, rectification is achieved by bringing together materials with different band alignments, rather than with doping gradients.

The use of p-n junctions to achieve a photovoltaic device is so common that it is sometimes believed to be necessary requirement. A more general definition for a photovoltaic is

that it is a two-terminal device, with a structure designed to sweep carriers in the conduction band to one contact and to sweep carriers in the valence band to the other contact. In p-n junctions, this is accomplished with the built-in electric field in the transition region near the interface of the p and n regions. PV devices without doping gradients can be realized by using semiconductor heterostructures. This is possible when there are certain band alignments between the constituent materials of the heterostructure. The band diagram of such a "heterostructure diode" structure for a hypothetical set of materials is shown in Fig. 1.3(b). In this device, the light-absorbing region of the device (the absorber) is sandwiched between an electron barrier region and a hole barrier region. The barrier regions are designed to block their namesake carrier and freely allow the flow of the other carrier type. These barriers are sometimes referred to as membranes in the solar photovoltaic literature [5].

The heterostructure PV design is advantageous for several regions. Since the bandgaps of the barrier regions are larger than that of the absorber material, the light absorption and thermal generation and recombination processes are primarily confined to the absorber. In addition, the barrier regions can suppress parasitic tunneling currents. These can be particularly problematic in LWIR and VLWIR infrared detectors due to the very narrow semiconductor bandgap [6,7]. However, as alluded to above, there is a very specific requirement for the band alignment between the absorber and the electron and hole barriers. It is difficult to find suitable combinations of lattice-matched bulk materials with the band alignments necessary for a heterostructure diode. Using modern epitaxial growth technology, it is possible to create a suitable set of materials using superlattices and bandstructure engineering [8-11]. This is the approach used for realizing the interband cascade PV structure [8, 12-14], which is the topic of this dissertation.

1.2 Overview of Infrared Detector Technology

1.2.1 Semiconductor Infrared Detector Materials

In order to be sensitive to long-wavelength light, the absorber material in infrared detectors must have a fairly narrow bandgap. Among the most popular absorber materials for infrared detectors are the II-VI material HgCdTe (MCT) and the III-V semiconductors InAs, InSb, along with the alloy InAsSb. The IV-VI material PbSnTe was fairly heavily researched in the period of 1960-1980. Some level of interest in this material continues to this day. Detectors based on the aforementioned materials are all based on interband transitions, which means the absorbed photons induce electrons to transition from the valence band of the material to the conduction band. Table 1.1 summarizes the important narrow-bandgap III-V semiconductors. Also shown are the bandgaps and corresponding cutoff wavelengths at 77 K and 300 K calculated by the band parameters in Ref. 15. For the alloy InAsSb, the choice of $InAs_{0.91}Sb_{0.09}$ corresponds to an alloy that is lattice matched to GaSb, while the choice of $InAs_{0.37}Sb_{0.63}$ corresponds to the longest wavelength achievable by this material. Note that detectors based on MCT and PbSnTe can achieve cutoff wavelengths throughout the mid-infrared through variation of the relative fractions of the constituent materials in the alloy.

Of these aforementioned choices, MCT is generally considered the best material for achieving detectors with the highest possible sensitivities. This is due to the material's favorable absorption and non-radiative properties. In addition, there have been large investments of time and money aimed at bringing detectors based on this material to technological maturity. However, detectors based on III-V semiconductors materials are able to remain competitive because of lower growth and fabrication costs, as well as the fact that they possess a higher level

of material uniformity across epitaxial structures. The latter property is necessary for the fabrication of good focal plane arrays (FPAs) with good uniformity across the pixels.

Material	E_g (77 K)	E_g (300 K)	λ_c (77 K)	λ_c (300 K)
InAs	407 meV	354 meV	3.1 μm	3.5 μm
InSb	227 meV	174 meV	5.5 μm	7.1 μm
$InAs_{0.91}Sb_{0.09}$	336 meV	283 meV	3.7 μm	4.4 μm
$InAs_{0.37}Sb_{0.63}$	137 meV	84 meV	9.1 μm	15 μm

Table 1.1: Bandgaps and corresponding cutoff wavelengths of narrow-gap III-V bulk semiconductors at temperatures of 77 K and 300 K. Calculated from parameters of Ref. 15.

There has not been extensive research into LWIR InAsSb-based detectors. One reason for this is that there is no good lattice-matched substrate for the alloy at the mole fractions needed to reach longer wavelengths. Thus, detectors based on bulk III-V materials have been primarily confined to MWIR applications. In order to extend the cutoff wavelengths of III-V infrared detectors, there has been significant research into superlattices (SLs) consisting of III-V semiconductors [16]. SLs are man-made materials that consist of alternating thin layers of semiconductor materials. The ability to choose the period of the constituent thin layers provides more flexibility for designing absorbers with certain properties such as the bandgap, effective mass, and absorption coefficient.

Most of the research into narrow-bandgap III-V SLs has been on those composed of alternating layers of InAs and GaInSb. Like MCT, these SLs have the potential to achieve cutoff wavelengths throughout the mid-infrared. This is due to the semi-metallic alignment between InAs and GaSb. In addition to using III-V materials, detectors based on InAs/GaSb SLs have also been predicted to be able to achieve sensitivities beyond those achievable by MCT. This possibility is enabled by flexibility to engineer the bandstructure of SLs by manipulating the layer widths of the constituent materials. More specifically, it was predicted that the dark current

that arises from electron-electron interband transitions could be made lower than that in MCT [17,18].

However, despite many years of development, there are still a number of obstacles that hinder InAs/GaSb SL from becoming the prominent material for mid-infrared detectors. The most alarming of these is the short lifetime for defect-assisted transitions. This was established by a number of time-resolved experiments [19-22]. The typical measured lifetimes for the material are on the order of 10-100 ns. For MCT, interband lifetimes are typically > 1 μs [20]. The postulated reason for this is the presence of a native defect in the GaSb layers. Since the short lifetime is caused by the presence of material defects, it is not believed to be an instrinsic limitation. With improved material growth or treatment, the full potential of this material may still be realized. Nevertheless, at the writing of this dissertation, this remains an open issue.

Due to the short lifetime of InAs/GaSb SL, there has been renewed interest in detectors based on "Ga-free" SLs composed of alternating layers InAs and InAsSb. This material has been shown to have a longer lifetime than InAs/GaSb SLs with similar wavelengths [23,24]. There have been some preliminary attempts to fabricate devices from this material, although exceptional performance has not yet been observed [25,26].

Another popular type of mid-infrared detector is the quantum well infrared detector (QWIP) [27]. In contrast to the narrow-bandgap materials listed above, QWIPs use intersubband optical transitions. There are several fundamental disadvantages associated with detectors based on intersubband transitions. First, special light-coupling schemes must be used, since transitions between quantum well energy levels cannot be induced by normal-incidence light. In addition, these transitions have higher thermal generation rates associated with them. This means they require more cooling to reach background-limited operation than interband detectors sensitive to

the same wavelengths. Also, for classical photoconductive QWIPs, the higher thermal generation rates result in higher values of dark current, which can saturate the read-out integrated circuit (ROIC) when the integration time is too long. Photovoltaic devices based on intersubband transitions in GaAs QWs, referred to as quantum cascade detectors (QCDs), have also been demonstrated [28]. These devices are able to operate with lower bias voltages, so there is less saturation of the ROIC, however, they still have the fundamental disadvantages of forbidden normal-incidence transitions and high thermal generation rate.

Despite the fundamental disadvantages, QWIPs are able to capture some market share because they utilize GaAs/AlGaAs QWs and are grown on GaAs substrates. Because of the technological maturity of this material system, the growth and device fabrication is much more mature than for narrow-bandgap III-V devices and in particular devices that use the II-VI and IV-VI materials. In addition to lower cost, the higher material quality ensures better uniformity across an epitaxial structure, making it a good candidate for large-area FPAs. In addition, QWIPs have been demonstrated to have very fast response times (~1 ps) making them the optimal choice for applications such as heterodyne detection that require high-speed detectors [29].

1.2.2 Advanced Semiconductor Infrared Detector Device Structures

For detectors that utilize p-n junction structures, the fundamental dark (i.e. non-radiative) current flow is typically separated into two sources. The first source is the generation of minority carriers in either of the quasi-neutral regions and their subsequent diffusion across the junction to the side where they are majority carriers. This generation can occur through either impact ionization, or can be assisted by defects [30]. Impact ionization occurs due to the electron-electron interaction. For defect-assisted generation, electrons are first excited from the

valence band to mid-gap defects, and then excited again to the conduction band. Thus, defects enable interband generation to occur through lower-energy processes such as phonon scattering [31]. Regardless of the specific microscopic excitation process, this sort of current is referred to as diffusion current. To first approximation, the temperature dependence of this current scales as $\sim n_i^2$, where n_i is the intrinsic carrier concentration. The other source of current is the generation of carriers in the depletion region, and their subsequent collection. This is often referred to as the generation-recombination (g-r) current. Current in the depletion region only arises from defect-assisted generation, since the depletion region is void of the free carriers needed for impact ionization. The temperature-dependence of this current scales as $\sim n_i$ to first-order approximation [32]. Note that the current flow in the heterostructure diode of Fig 1.3(b) is diffusion current only, since there is no depletion region in the structure.

As stated earlier, semiconductor heterostructures can be used to establish a photovoltaic architecture without introducing doping gradients. This requires finding appropriate materials that can act as selective barriers for establishing a preferred direction of current flow. This is often not possible in detectors that only utilize bulk materials. However, heterostructures with a single barrier layer can also be used to control the current flow mechanisms in a detector. The potential for this sort of control is particularly present in the Sb-based III-V materials. Examples of this sort of detector include the nBn [33], which uses an InAs absorber and substrate, and the XBn, which uses $InAs_{0.91}Sb_{0.09}$ absorber and is grown on a GaSb substrate [34]. It is shown in Ref. 35 that the basic physics of these single-barrier detectors is the same. As in a p-n junction, a doping gradient between the contact and absorber layers is used to achieve a photovoltaic effect. However, in the region near the junction a wider-bandgap barrier material is inserted. In order to achieve a working detector, the barrier material must not inhibit the flow of the photocarriers

from the absorber to the contact. For InAs and GaSb-based detectors, the bulk material AlAsSb can be used as a barrier, since it has a valence band edge higher than that of the absorber. Thus, minority holes can freely pass through the barrier layer. The mole fraction for the AlAsSb alloy is chosen so that the barrier material is lattice-matched to the substrate. The thickness of the wide-bandgap layer is typically hundreds of nanometers [33].

One advantage of this single-barrier diode design is that the electric fields are confined to wide-bandgap material. This suppresses generation-recombination current, which is fundamental in p-n homojunctions, by suppressing any generation and recombination events in that part of the structure. This is useful as a means of ensuring diffusion-limited transport at lower temperatures. Since the temperature scaling of the diffusion dark current is as n_i^2, this current will typically be orders of magnitude lower than the generation-recombination current at low temperature. This is a favorable choice for many infrared detector applications where cryogenic cooling is used. However, this design will not always be more favorable at higher temperatures (i.e. > 200 K). Due to the different temperature-scaling of diffusion and g-r currents, it is expected that for a given material there is some threshold temperature, above which g-r dark current is lower than diffusion current.

A fruitful outcome of research into the single-barrier heterostructure detectors is that it has impelled a rethinking in the approach to mid-infrared FPA fabrication. The constituent detectors in FPAs must be very small, with typical dimensions of < 50 μm. Due to the small size, a major issue in mid-infrared FPA fabrication is dealing with the non-idealities related to the device surface. To fabricate the FPA, the individual pixels are formed by etching through the epi-layers to the buffer layer of the epitaxial structure. The exposed surface then must be passivated to prevent oxidation of the sidewalls and eliminate mid-gap surface states. Typically,

this is done by depositing of a layer of a dielectric material such as SiO_2 or Si_3N_4. However, even with several years of refinement of the passivation techniques there are still noticeable surface effects [36]. This is especially true for LWIR detectors. In addition, the etching process becomes more difficult when the epitaxial material is very thick.

In the original nBn paper, it was shown that the barrier layer can provide self-passivation of the surface [33]. In this sort of FPA, only a shallow-etch through the top contact is performed to isolate the pixels. With this arrangement, a special passivation treatment is not needed, since the wide-bandgap barrier region isolates the electrons in the narrow-gap region from the device surface. This prevents the formation of leakage channels along the surface. Notably, it has been shown to limit $1/f$ noise above 1 Hz in InAs-based detectors under a strong reverse bias [37]. In recent years, the shallow-etch FPA design has also been applied to double-barrier heterostructure diodes [38,39]. However, the adoption of this FPA design requires a material with a fairly low lateral diffusion length, so as to prevent cross-talk. This is not a problem in deep-etched devices, since the dielectric layers deposited for passivation prevent the lateral flow of carriers between individual devices on an array.

For high-temperature detector operation, the major obstacle for detectors based on MCT (and many other materials) is the high rate of interband transitions based on electron-electron interactions (interband generation is referred to as impact ionization and recombination is referred to as Auger recombination). One design introduced by Elliott and White is the so-called "non-equilibrium" design [40-42]. The structure is essentially a standard p-i-n structure. The p and n regions are referred to as extraction and exclusion junctions. The absorber doping is kept as low as possible so that in equilibrium the material is intrinsic. The product of free electron and free hole concentrations is given by

$$np = n_i^2 e^{eV/k_b T}, \tag{1.2}$$

where V is the applied bias and T is the temperature. Under application of reverse bias, the noise due to recombination is quenched and the absorber is depleted of free carriers. In the limit of zero background doping, this also eliminates impact ionization (and hence all the effects of interband electron-electron effects). Thus, non-radiative generation is solely due to defect-assisted effects, and thus is only determined by the density of recombination-assisting defects of the absorber material.

Research into this sort of device has been ongoing since its initial proposal in 1985. Both negative luminescence [43] and negative differential resistance [44-45] in these devices has been observed. The former validates the suppression of recombination under reverse bias (light emission is due to radiative recombination). The latter phenomenon confirms the transition of dominant current from electron-electron effects near equilibrium to defect-assisted effects under strong negative bias. Both of these observations provide confirmation that the absorber is depleted of free carriers. However, the expected improvement in detector sensitivity has not yet been established. The primary reason that has been identified for this is a large $1/f$ noise that is present in these detectors under the strong reverse bias needed to suppress the Auger effects. However, interest in this design has contributed to be strong due to its potential for realizing good high-temperature performance.

1.3 Overview of Infrared Photovoltaic Energy Conversion

Photovoltaic devices provide a means for directly converting radiation into electrical power. The devices are essentially heat engines that take advantage of the natural flow of radiation from hot sources to the lower-temperature cells. For blackbody-like radiation, the

transfer of radiation is described by Eq. 1.1. For a general heat engine, the fundamental limiting efficiency is the Carnot efficiency:

$$EFF = 1 - \frac{T_s}{T_{cell}}, \tag{1.3}$$

which is about 95% for solar energy conversion. However, the PV concept is not limited to solar energy conversion. It can be used to convert energy from virtually any source that emits radiation. There is interest in using these cells to convert the energy emitted by nuclear sources. Another application for PV cells is as a supplement to conventional fossil-fuel-burning power systems. The cells can augment the efficiency of these systems by reclaiming some of the lost energy given off as "waste heat" during the combustion process. However, the development of commercial PV cells for non-solar applications has been inhibited by the high material cost. In addition, the efficiency of these systems will be inherently lower. The temperatures for terrestrial sources are typically in the range of 500-1500 K. For a 1500 K source, the Carnot efficiency is 80%, while for a 500 K source the efficiency is as low as 50%.

Systems designed to convert primarily infrared light are typically referred to as thermophotovoltaic (TPV) systems. TPV systems often utilize spectral shaping technology to alter the spectral distribution of the radiative energy to one that can be converted by the cell with a higher efficiency [4]. The spectral shaping component could be a filter that reflects and passes light with certain wavelengths, or a selective emitter that, when heated, emits light over a very narrow range of photon energies. Selective emitters with emission near the cell bandgap would be the "ultimate" spectral shaping component, since it would mitigate losses due to both thermalization and below-bandgap light transmission. These are the most significant intrinsic losses in PV conversion.

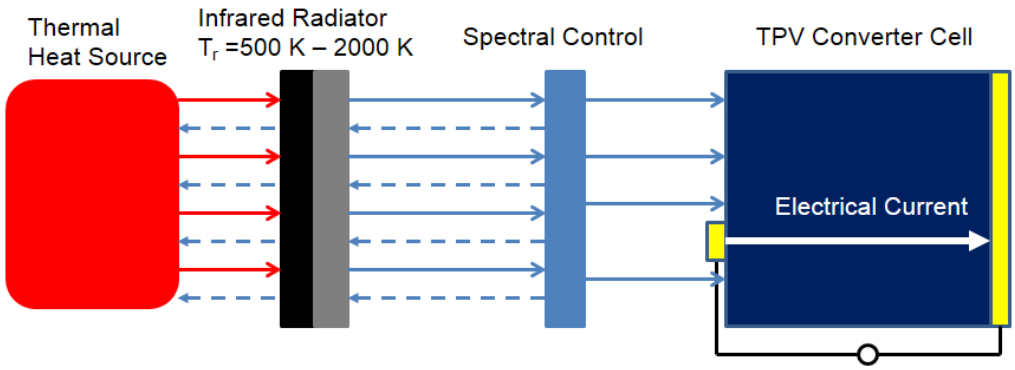

Figure 1.4: Schematic of a TPV conversion system that incorporates spectral shaping components.

A schematic of typical a TPV system is shown in Fig. 1.4. The radiation from the thermal source (can be any source of heat) is used to heat an intermediate radiator. The light from this radiator is then converted to electrical power by the converter cell. In an ideal system, the filter between the radiator and the converter cell would transmit photons above the bandgap of the converter cell and reflect photons with energies below the bandgap.

For solar cells, the common absorber materials include Si (E_g ~1.1 eV) and GaAs (E_g~1.4 eV). These are appropriate bandgaps for solar energy conversion, as much of the available energy is in the optical and near-infrared regions of the spectrum. For lower energy sources, where more energy is concentrated in the mid-infrared, research has been focused on cells that employ InGaAs, GaSb, or some other variant of the GaInAsSbP alloy as the absorber material [46-48]. The bandgaps of these materials have generally been in the range of ~0.50 eV. However, for blackbody-like sources with temperatures ≤ 1500 K, cells that use these absorber materials still have inherently low efficiencies due to large losses from the transmission of below-bandgap photons. Low source temperatures are preferable for many applications, as they are easier to integrate into systems [4]. Thus, there is interest in exploring cells with narrower bandgap absorbers. In addition, there has been some promising research into metamaterials that

may be useful as selective emitters in the mid-infrared [49,50]. Another potential application is optical power beaming systems. Transporting energy over mid-infrared wavelengths may reduce the significant atmospheric absorption and scattering losses that can occur at shorter wavelengths.

If the PV cell is being utilized for converting radiation with a blackbody-like distribution, one way to estimate the optimal bandgap for a given source temperature is to utilize the theory of detailed balance [51, 52]. The detailed balance limit imposes a more stringent upper limit on the efficiency than the Carnot limit, since it also accounts for the power losses from below-bandgap photon transmission and the thermalization of carriers excited by above-bandgap photons. In the detailed-balance theory the cell is treated as a thermal "greybody" radiator. This represents the limit where all the generation and recombination in the absorber is radiative. In the greybody limit, the cell is able to absorb and emit photons with energies above the bandgap, E_g, as a blackbody at the cell temperature would, but does not absorb or emit photons with energies less than the bandgap. When the cell is placed under a bias of V, the cell will emit light as a greybody with a chemical potential of eV [53]. In the detailed balance limit, the current flowing under a certain bias voltage in the cell is given as:

$$J_{cell}(V) = -e\frac{2\pi}{h^3c^2}\int_{E_g}^{\infty} dE\left[\frac{E^2}{e^{\frac{E}{k_bT_s}}-1} - \frac{E^2}{e^{\frac{(E-eV)}{k_bT_{cell}}}-1}\right], \tag{1.4}$$

where T_s is the source temperature and T_{cell} is the cell temperature. The first term in the integrand represents the reverse cell current that arises due to electron absorption of photons. The second term represents the forward cell current that arises due to the recombination of electrons. Note that an ideal photovoltaic device is a perfect absorber under strong reverse bias ($|eV| \gg k_bT$). This is the negative luminescence effect described earlier.

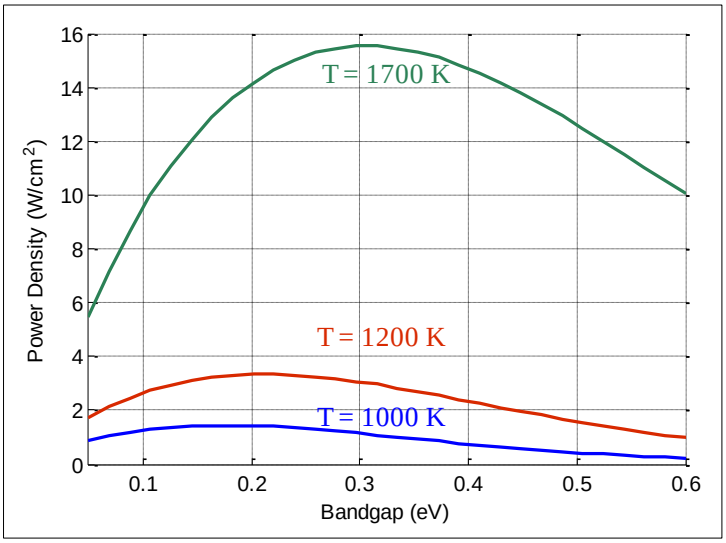

Figure 1.5: Detailed balance calculation showing the upper conversion limit for different blackbody source temperatures for a cell with a certain bandgap.

From Eq. 1.3, the cell power in the detailed balance limit can be calculated for a given T_s and E_g. This was done by calculating the *J-V* characteristics, and finding the maximum cell power, given by: $P_{out} = -JV$. The results are shown in Fig. 1.5 for source temperatures of 1700 K, 1200 K, and 1000 K. It is seen that for this range of source temperatures, the bandgap at which the cell power density is maximized ranges from 200-300 meV. This is well less than the ~500 meV cell bandgaps currently used. Note that the detailed balance limit is a very idealized limit. In realistic narrow-bandgap devices, Auger and defect-assisted recombination tend to dominate over radiative recombination. Inclusion of the non-radiative recombination in the analysis will widen the optimal bandgap for a given temperature. However, the point remains that there is great potential in further development of PV cells with bandgaps less than 400 meV.

1.4 Dissertation Introduction

This chapter has given an introduction to the PV conversion of infrared radiation and relevant technological applications. Aside from the intersubband QWIPs, all the device designs utilize a structure with a single, thick (> 2 μm), absorber region. Such a thick absorber is

necessary in order to absorb most of the incident light. Typically, the absorption coefficient at energies near the bandgap becomes smaller for materials with narrower bandgaps. Thus, for applications such as the photodetection of radiation in the LWIR region of the spectrum, very thick absorbers are required. For MCT detectors, a general rule of thumb is that the absorber thickness should be roughly equal to the cutoff wavelength [54]. However, making the absorber thicker does not guarantee that all the photons will be used efficiently, even if they are absorbed. This is because when the absorbers are very thick, only those carriers that are able to diffuse to the collection point before recombining produce photocurrent. This limitation to the photocurrent in single-absorber devices can be particularly apparent at higher temperatures, where the minority carrier diffusion length is often shorter. In addition, narrow-bandgap optoelectronic devices tend to be more susceptible to series resistance effects [55]. This is an especially detrimental effect for energy-conversion applications, because the currents tend to be quite high.

The issues of inefficient photon usage and large series resistance power loss can be partially mitigated by using an alternative type of photovoltaic architecture based on interband cascade structures. In these structures, the absorption and collection process is distributed across multiple discrete stages. The stages are electrically connected together by designing the structure so that electrons in the conduction band of one stage can tunnel to the valence band of the next stage in the series via fast, low-energy scattering processes. If the inter-stage connection can be made efficiently, with minimal extraneous absorption or additional resistance, this enables a multiple-stage device where the absorbers can be kept fairly short to ensure good carrier collection. This arrangement reduces the operating current in the device, which is limited to the value of the current generated in one of the short stages. However, the overall power in the

device is not necessarily reduced because the voltage across each stage adds to create the total voltage in the device. This tradeoff is useful for reducing the series resistance losses that can be problematic when the device operating current is high.

The opportunity to create multiple-stage devices based on interband transitions is possible when utilizing heterostructures composed of the group of III-V semiconductors with lattice constants near 6.1 Å. This group includes InAs, GaSb, AlSb, and their related alloys. The three binary semiconductors are nearly lattice-matched. High quality heterostructures composed of these materials can be grown on InAs or GaSb substrates using molecular beam epitaxy (MBE).

The subsequent chapters of this dissertation will detail research carried out to explore and demonstrate the advantages of the interband cascade approach for certain applications. Chapter 2 will provide a historical perspective on the development of interband cascade optoelectronic devices. It will also present a qualitative overview of the attractive features this design presents for sensing and energy conversion applications. In Chapter 3, a general analytic model describing the physics of multiple-stage devices is presented. This model is then applied to compare the ultimate limits of single-absorber and multiple-stage devices. Chapters 4 and 5 describe the design and experimental characterization of interband cascade PV devices. Chapter 4 focuses on devices targeted for energy conversion. The devices investigated include a series that utilized InAs/GaSb SL absorbers and others that utilized InAs SL absorbers. As shown, these devices are able to achieve high open-circuit voltages. However, the efficiency is limited by a low fill factor, which is shown to be partially due to surface shunting effects. Chapter 5 focuses on devices targeted for use as infrared detectors. This chapter gives an experimental comparison between single- and multiple-stage infrared detectors with cutoff wavelengths in the

MWIR. The sensitivity of the different designs is compared as a function of temperature. It is shown that at high temperature, the decrease in photoresponse caused by the reduction in diffusion length is mitigated. Thus, these detectors are able to achieve a better sensitivity at high temperatures. The main findings from this work and a discussion of the future prospects of interband cascade photovoltaic devices are included in Chapter 6.

Chapter 2 : Overview of Interband Cascade Structures

2.1 Historical Perspective – Interband Cascade Lasers

The concept of what would eventually become the interband cascade design for optoelectronic devices was first presented in 1994 [56]. This design was originally proposed as an alternative to the intersubband laser, which a hot research topic at the time in the photonics community. Shortly before this proposal, a laser based on intersubband transitions was demonstrated at Bell Labs [57]. The Bell Labs intersubband laser was dubbed the quantum cascade laser (QCL). The term "cascade" in the name referred to the fact that the laser was composed of multiple stages cascaded together in series. Each individual stage was designed to enable electrons to relax to lower energy states by emitting photons. The relaxed electrons were then transported to the next stage. With the cascade design, a single electron was used to generate multiple photons.

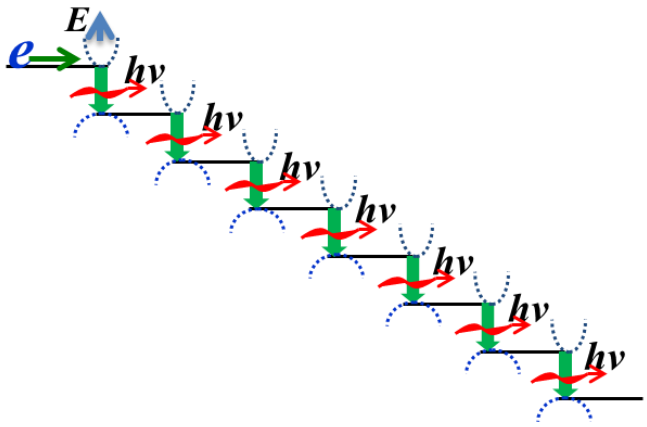

Figure 2.1: Schematic of electron transport and photon emission in interband cascade laser. From Ref. 58.

When a cascade laser is forward biased, lasing can occur when the individual stages are separated by an energy larger than eV/N_s, where V is the bias voltage and N_s is the number of stages. Current flow in the device arises due to the relaxation of electrons through the cascade,

as seen in Fig. 2.1. Ideally, the electron relaxation occurs by photon emission rather than non-radiative processes. A cascade laser requires a higher voltage than a standard laser diode. This is because each stage must consume enough voltage to obtain population inversion. However, the current required to generate a certain output power is reduced, as multiple photons are produced for each injected electron. At the high operating currents needed for a high-power semiconductor laser, the Ohmic power loss, equal to I^2R_s, where R_s is the series resistance, can be particularly detrimental. Thus, the cascade design can be beneficial for improving the total power conversion efficiency by lowering the operating current.

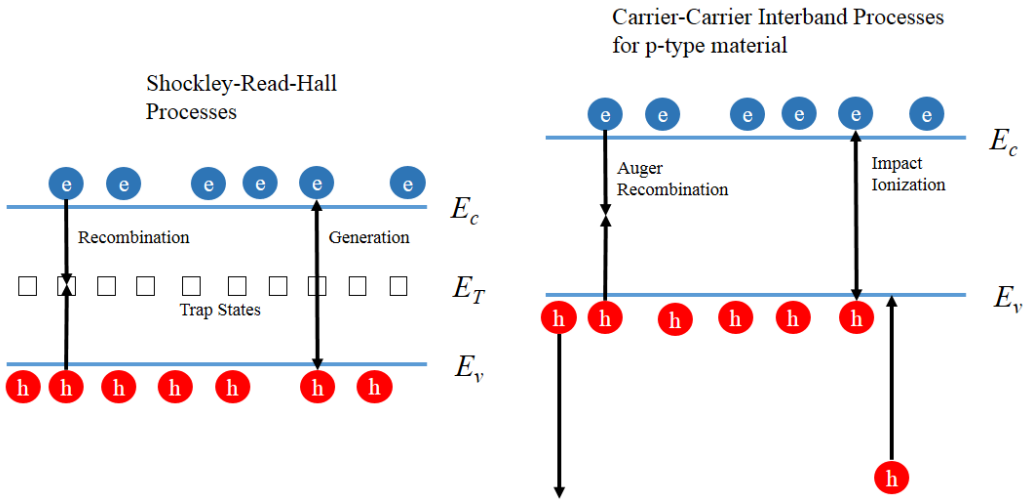

Figure 2.2: Non-radiative generation and recombination processes in semiconductors.

The first multiple-stage interband laser following the design of Ref. 56 was demonstrated in Ref. 59. It was shown that this sort of interband laser was able to achieve differential quantum efficiencies greater than 100%, meaning that a single injected electron was in fact generating more than one emitted photon. This was an important validation of the multiple-stage nature of the device. Due to its similar nature to the QCL, this multiple-stage interband laser was christened the interband cascade laser (ICLs). Like QCLs, ICLs utilize a cascade design. Another similarity between the designs is that ICLs use bandstructure engineering for tailoring

the energy that photons are emitted and absorbed and for achieving the diode configuration needed for many optoelectronic devices. However, unlike the intersubband devices, photon emission in ICLs occurs via interband transitions. This is an important distinction because non-radiative interband transitions occur on a much longer timescale than intersubband non-radiative transitions. The non-radiative lifetime of interband devices is determined by Auger recombination (the inverse of impact ionization) or by defect-assisted Shockley-Read-Hall recombination (the inverse of the defect-assisted generation process described in Chapter 1). These processes that mediate non-radiative interband generation and recombination are illustrated in Fig. 2.2. Intersubband devices are limited by phonon scattering, which occurs on a much faster (> 2 orders of magnitude) timescale. For lasers (and other optoelectronic devices) the device performance will be better if the non-radiative lifetime for the optical transition is longer. Note that this fast intersubband scattering time is the also the source of the high thermal generation rates in QWIPs discussed in Chapter 1.

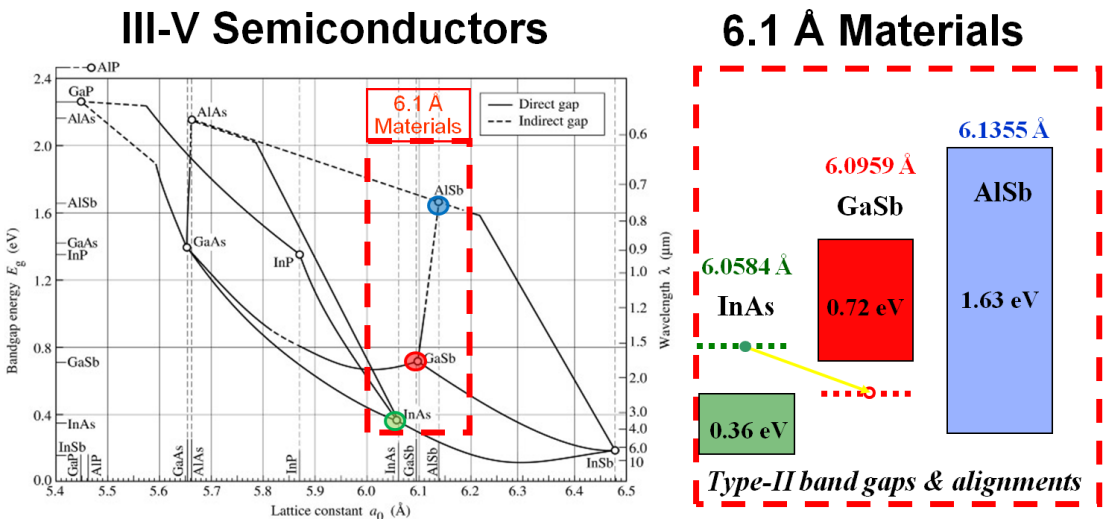

Figure 2.3: Lattice constants and band alignments of binary III-V 6.1 Å semiconductors. Figure is from Ref. 60.

In ICLs, a type-II heterostructure is employed to efficiently transport electrons between the conduction band of one stage and the valence band of an adjacent stage. This sort of

heterostructure is made possible by the unique band alignments of the 6.1 Å group of semiconductors. The relative band alignments of these binary semiconductors at room temperature is shown in Fig 2.3. Note that the bandgap for AlSb refers to the energy gap between the indirect X-Γ transition. The key feature that makes this set of materials ideal for multiple-stage devices is the unique type-II broken-gap alignment that exists between InAs and GaSb. The conduction band edge of InAs actually falls about 150 meV below the valence band edge of GaSb. For heterostructures that include both InAs and GaSb layers, this means that electrons can easily pass between conduction band states localized in the InAs layers and valence band states localized in the GaSb layers via fast scattering processes in which little energy is gained or lost.

The way this type-II broken-gap alignment is exploited in an ICL can be seen in Fig. 2.4. This figure shows the layer sequence of a single stage under forward bias and the resulting band diagram. An individual stage in an ICL is composed of an active region, consisting of an InAs-GaInSb-InAs "W" QW [61], an electron injector, consisting of digitally graded InAs/AlSb QWs, and a hole injector, consisting of GaSb/AlSb QWs. When the ICL is placed under forward bias, electrons are injected from the conduction band of the electron injector into the conduction band of the active region. The injected electrons then relax to the valence band of the active region. The relaxed electrons are swept into the valence band of the hole injector. Because of the type-II alignment between the GaSb layers in the hole injector and the InAs layers in the electron injector, the electrons are then able to pass through the valance band of the hole injector into the conduction band of the electron injector of the next stage. As stated above, these interband processes that enable electrons to pass between stages are very fast processes, such as phonon scattering. Because of the strong coupling enabled by the type-II interface, the electrons in the

valence band of the hole injector come into equilibrium with the electrons of the conduction band, faster than they equilibrate with the conduction electrons in their own stage.

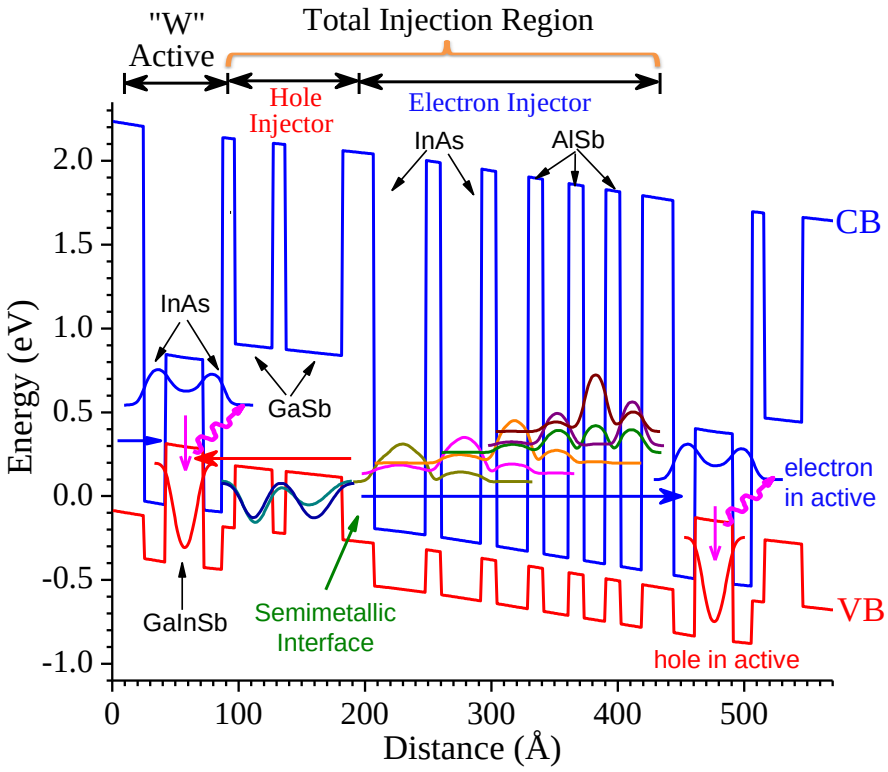

Figure 2.4: Band diagram of an interband cascade laser stage under forward bias. Figure is available in public domain and was taken from Wikipedia Commons. It is originally from Ref. 62.

ICLs combine the advantage of reduced Ohmic losses from cascade lasers with the advantage of the long lifetime of interband transitions. At present, cw operation of ICLs at room temperature has been demonstrated from 2.9 to 5.7 μm [63].

2.2 Interband Cascade Devices for Light-to-Electricity Conversion

2.2.1 Structure and Device Overview

The majority of research into interband cascade structures has focused on their usefulness for realizing good light-emitting devices. However, the advantages offered by the multiple-stage architecture may actually be more signficant for optoelectronic devies designed for light-to-electricity conversion. In this disseration, we will generally refer to these structures as interband

cascade photovoltaic (IC PV) structures. These device structures can be used to fabricate interband cascade infrared photodetectors (ICIPs) or energy-conversion cells.

The concept and demonstration of an IC PV device was first presented in 2005 [8]. These initial devices were actually fabricated from ICL structures. Thus, the active part of the device resembled the band diagram of the ICL in Fig. 2.4. The light absorber region consisted of only a single pair of coupled quantum wells. In subsequent devices, the design did not have to be significantly altered. This is because the basic device structure for a good light emitter and good PV device are similar. It can be seen that a single stage in the ICL in Fig. 2.4 resembles the heterostructure diode in Fig. 1.3(b). The electron injector in an ICL can serve as the hole barrier in an IC PV structure. Analogously, the ICL hole injector can serve as the electron barrier. Thus, a single stage in the IC PV is a double heterostructure, with the absorber between wider bandgap electron and hole barriers. The rectification effect within a stage is established by using type-II staggered band-edge alignment between the absorber and barrier regions.

The main modification to the basic interband cascade structure in the optimization for PV applications has been the replacement of the coupled quantum wells with longer InAs/GaSb type-II SL absorbers [10-11]. This choice enabled the devices to absorb a much larger percentage of the incident photons. Recent designs have also enhanced the thickness of the electron barrier region compared to that in a typical ICL. This was done to suppress any inter-stage tunneling currents [14,64].

Since current rectification in IC PV devices is achieved using heterostructures, rather than doping gradients, intentional doping is not required anywhere in the structure. However, the absorbers in IC PV devices are typically doped *p*-doped. This is done in order to make holes the majority carrier in the absorber. Studies of structures with different doping choices has found

that InAs/GaSb SL detectors with majority holes in the absorber have lower dark currents [65-66]. This is presumably because the interaction cross-section between the trap states and valence band states is lower than that between the trap states and conduction band states. This doping choice has also been adopted for IC PV energy conversion devices.

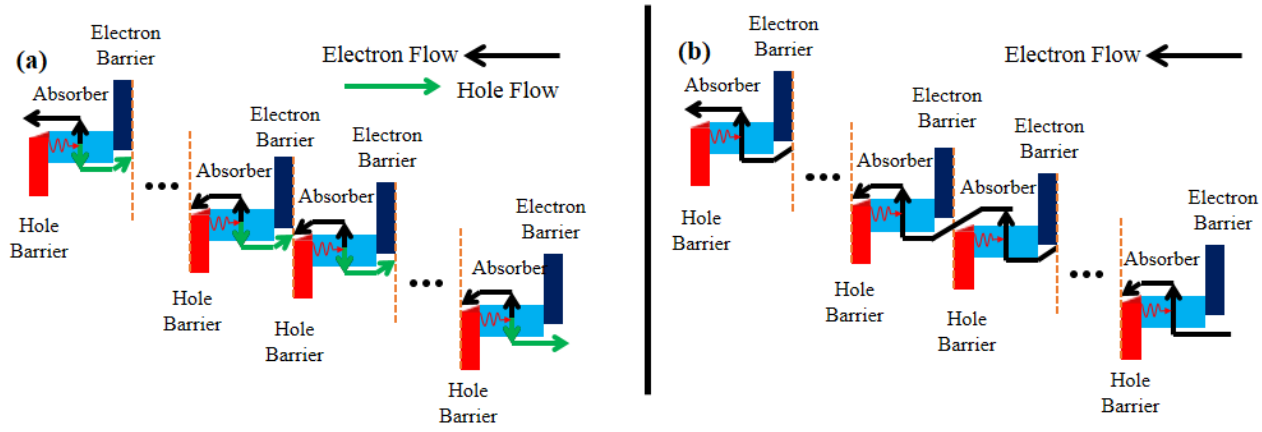

Figure 2.5: General schematic for interband cascade PV devices under forward bias for (a) electron-hole and (b) electron-only pictures. The black (green) lines and arrows show the transport path of electrons (holes) from generation in the absorber to recombination (collection) at the interface of the electron and hole barriers (denoted by the brown dashed lines).

Fig 2.5(a) shows a basic schematic of a multiple-stage IC PV device in forward bias. Note that the band alignment of a single stage in the figure differs in an important way from that of the stage shown in Fig. 1.3(b). In the structure of Fig. 1.3(b), the valence band edge of the electron barrier is below the conduction band edge of the hole barrier. For IC PV devices, the ground state of the electron barrier valence band is designed to be above or within k_bT of the ground state of the conduction band ground state of the adjacent hole barrier. This is a necessary condition for an efficient interband stage-to-stage transition. The black and green lines in the figure designate the ideal transport paths taken by electrons and holes, respectively. The direction of the net flow for a given carrier is away from its namesake barrier. The carriers generated within an internal stage of the structure recombine with another internally generated

carrier from an adjacent stage. This carrier recombination occurs at the interface of the electron barrier and hole barrier of the adjacent stages. Electrons generated in the top stage of the stack and holes generated in the bottom stage will be collected at the device contacts. It is also insightful to think of an alternative picture, where the concept of holes is disregarded. This representation is illustrated in Fig. 2.5(b). Here, electrons are excited from the valence band of a stage's absorber to the conduction band of the absorber. The electrons then pass through the unipolar barrier regions to the valence band of the next stage. They are then excited again by another photon.

The recycling of electrons permits interband cascade PV devices to achieve photovoltages higher than the individual absorber bandgap. This does come at the cost of a lower *upper limit* for the photocurrent. This is because the top contact only extracts electrons generated in the top stage of the stack. Nevertheless, this tradeoff between photocurrent and photovoltage will be beneficial in many cases. Similar to ICLs, the reduction in operating current will mitigate contact resistance power losses in energy-conversion cells based on the IC PV structure. These losses are particularly detrimental for narrow-bandgap, single-absorber converters. This is because in PV devices with narrow bandgaps a larger percentage of the power is carried as current, rather than voltage. In addition, most potential terrestrial PV applications, such as micron-gap TPV [67] and laser power-beaming applications, involve the conversion of large incident light intensities. The current for voltage trade also raises the resistance of the device. This should be a useful feature for ICIPs, because the higher device resistance makes it less likely the noise will be limited by the preamplifier and other parasitic sources [68]. This parasitic noise can be especially problematic at longer wavelengths where the detector bandgap is small and thus the resistance of a single-absorber devices is inherently low.

2.2.2 Carrier Collection Improvement

Another advantage of the multiple-stage design is that the thickness of the absorbers can be kept shorter than the diffusion length. This ensures that most of the carriers are collected before they recombine (either at the contacts or at the electron-barrier/hole-barrier interface). Particle conversion efficiencies, defined as the percentage of incident photons that generate an electron that is collected, close to 100% should be possible.

The improvement in carrier collection offered by the multiple-stage architecture is illustrated in Fig. 2.6 for detectors with p-type absorbers. This figure compares the absorption and collection process of a single-absorber detector with that of a four-stage detector for the case where $\alpha L_n = 0.5$. The four-stage PV device is chosen to have identical stages. The total absorber thickness, d, for both detectors was set equal to the absorption depth. Thus, the individual absorber thicknesses for the four stages in the detector are equal to $d/4$. Since light absorption only occurs in the absorber region, the total absorption efficiency for both detectors is equal. In this example, the light is taken to be incident on the absorber from the minority carrier collection point.

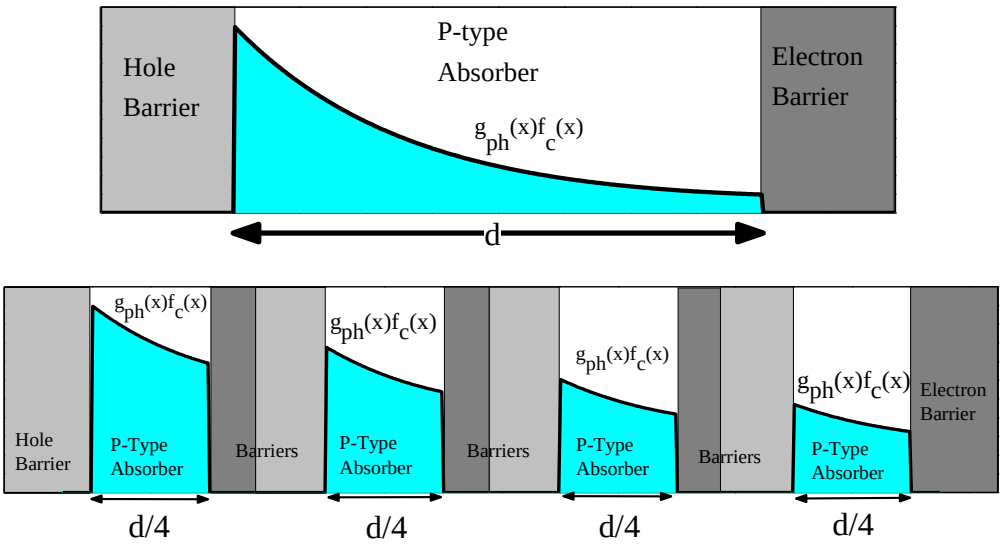

Figure 2.6: Comparison of collection efficiency in single- and multiple-stage absorbers for detectors using a p-type absorber material with a low αL product. In this example αL was 0.5, and the thickness of the single-stage device was set equal to the absorption depth α^{-1}. The absorber thicknesses of the four-stage device are $d/4$. Thus, the total absorption thickness in the two devices is the same. The shaded regions in each stage indicate the variation of the product of the photo-generation rate and minority carrier collection probability across the absorber.

The shaded region in the absorber show how the product of the photo-generation rate, $g_{ph}(x)$, and carrier collection probability, $f_c(x)$ varies across the absorber region. The carrier collection probability is higher throughout the absorber regions of the multiple-stage device because of the discrete collection architecture. The rate that carriers are collected in a given stage is the integral of the product of these two quantities across the stage absorber. The total collection efficiency is defined as the ratio of the incident photons that are successfully converted to collected current in any of the stages. This collection efficiency is found to be fairly low (54%) for the case of a single-absorber detector. This is due to the low carrier collection probability at points far from the minority carrier collection point. Notably, the carriers that are generated at the right edge of the absorber, and have to travel across the entire absorber to be collected, only have a collection probability of ~27%. In contrast, each stage in the multiple-

stage detector has a carrier collection point at the interface of the hole barrier and the absorber. Since the absorbers are kept short, the collection efficiency stays fairly high across the absorber. This enables the multiple-stage device to achieve a much higher total collection efficiency of 93%. For this case, the carriers generated farthest from the collection point at the right edge of one of the absorbers still have a high collection probability of ~89%.

It should be noted that since infrared detectors are typically operated near zero bias, there is an additional requirement that the device have an equal photocurrent in all stages. This will reduce the effective particle efficiency of the device. In ICIPs, the photocurrent will be equal to the photo-generation rate in the stage with the lowest photo-generation rate. For ICIPs with identical stages, this will be the optically deepest stage. In order to keep a constant current through the device, the other stages must have some compensating injection current. For ICIPs with identical stages, this negates some of the advantages of the multiple-stage architecture. An alternative design choice is to utilize a photocurrent-matched detector design, where the absorber thicknesses are varied across the structure in order to achieve an equal photo-collection current in each stage. It is notable that this loss of signal due to the current-matching effects is not present when an illuminated device is operated at zero net current. For an illuminated device with zero current, each photon that contributes to the photo-collection current in any of the stages, requires some additional forward bias to bring the detector to a zero-current condition. This is one reason why the open-circuit voltages in interband cascade structures can be quite high [13].

2.3 Noise Reduction in Multiple-Stage Infrared Photodetectors

The previous section presented the advantages of a cascade structure for improving energy-conversion cells designed to convert mid-infrared radiation. However, even with improved carrier collection, it may still seem counter-intuitive to engineer a photodetector that

requires multiple incident photons to generate a single electron in the external circuit. This sort of design probably seems even more ludicrous when it is taken into consideration that an ICIP with several identical stages will have the same saturation dark current as one with a single-stage that is equivalent to those in the multiple-stage device! To truly understand the benefits of a multiple-stage design, it is necessary to consider how the use of multiple stages influences the noise associated with the current flow.

The noise in a detector results from the inherent uncertainty in the arrival times of electrons to the collecting contacts. In interband detectors, the flow of current between the device contacts is primarily bottlenecked by the interband transition of electrons from the absorber valence band to the absorber conduction band. Each interband excitation is a random process that follows the Poisson distribution. As seen in Fig. 2.5, by introducing multiple-stages into the structure, electrons are forced to undergo additional interband transitions as they pass between the contacts. For the single-stage structures, such as those in Fig 1.3, the transport of an electron between the device contacts is bottlenecked by only a single interband transition. Thus, only a single random event is required to produce current. From Poisson statistics, the uncertainty in the arrival time rate for a single-stage device will scale will the square root of the average arrival time rate. This relationship was established by Schottky [69]. For a device with N_s stages, random events in each of the stages are required to create an electron flowing in the external circuit. Thus, the uncertainty in the current will be reduced by a factor of N_s. The addition of stages to a detector essentially has the same effect as the addition of extra trials in a measurement of the current. It is well-known that additional trials in an experiment lowers the measurement uncertainty.

There are actually several other electronic systems where noise reduction is achieved by increasing the number of transition events the electron must undergo in their transport path between the contacts. One example is the aforementioned QWIP detectors. In these intersubband detectors, as long as the emission and capture events in each of the wells are uncorrelated, the noise is reduced by a factor of $1/N_w$, where N_w is the total number of wells in the detector structure [70]. The experimental verification of this was established in Ref. 71. Another common example is the double-barrier resonant tunneling structure, where the electron must tunnel across two separate barriers as it traverses from the emitter to the collector [72]. This can result in noise reduction by as much as a factor of 1/2. Also notable is that in reverse-biased p-n junctions, when the interband transitions are primarily due to recombination and generation at deep traps in the depletion region, it is possible for the noise to be reduced if the emission and capture cross-sections for electrons in the conduction band and holes in the valence band are of comparable magnitude [73,74]. In this system, the noise reduction can also be as much as ½ since there are two independent processes, hole emission and electron emission, that are required for current flow under reverse bias.

The potential of using this sort of design to improve the sensitivity of infrared detectors has actually been explore previously. Earlier attempts to realize these sorts of devices using MCT were carried out by utilizing tunnel junctions to electrically connect the conduction band of one absorber to the valence band of an adjacent absorber in a way similar to multi-junction solar cells [68,75]. However, this proved difficult due to both extraneous absorption at the tunnel junction [76] and due to high series resistance between the tunnel junctions [77].

Chapter 3 : Theoretical Comparison of Multiple-Stage and Single-Stage Interband Photovoltaic Detectors

3.1 Theoretical Framework for Multiple-Stage Device Analysis

3.1.1 Signal and Noise in Infrared Detectors

The sensitivity of an infrared detector is determined by the signal-to-noise ratio. As such, the sensitivity depends on both the detector's external quantum efficiency (EQE), η_{ext}, and the noise current, i_n. In this work, η_{ext} is defined as the number of electrons produced in the external circuit per incident photon. If a photon flux of Φ_o, is incident on a detector with an EQE of η_{ext}, the resulting photocurrent, i_{ph}, is given by:

$$i_{ph} = e\Phi_o\eta_{ext}. \tag{3.1}$$

In the subsequent analysis, it is assumed that the detector has a good anti-reflection coating, so the optical losses at the air-semiconductor interface are negligible. In multiple-stage detectors, at least one absorbed photon per stage is required in each stage to maintain a continuous photocurrent through the structure, unless there are internal gain mechanisms. This means that for a multiple-stage detector with N_s stages, the value of η_{ext} is bounded by $\eta_{ext} \leq 1/N_s$, where N_s is the number of stages. The noise current in a semiconductor device is given by the autocorrelation function:

$$i_n^2 = \langle i(t)i(0)\rangle_t - \langle i\rangle_t^2, \tag{3.2}$$

where $<>_t$ represents a time-averaged quantity.

Typically, the quality of an infrared sensor is assessed using figures of merit that do not depend on the strength of the incoming signal or the integration time. Common alternative figures of merit for evaluating a focal plane arrays (FPAs) are the noise-equivalent power (NEP) and the noise-equivalent temperature difference (NETD). The noise equivalent power represents the signal power required to achieve a signal-to-noise ratio of unity. The NETD is defined as the

temperature difference at which the induced change of the background power equals the NEP. The NETD is particularly relevant for infrared imaging applications, because it directly gives the temperature resolution of a thermal imaging system. In this work, we will not be characterizing FPAs, but instead single-element detectors. The sensitivity a single-element detector is typically quantified by specific detectivity, D^*. The value of D^* is proportional to the inverse of the noise-equivalent power, and is normalized for a detector of a given area, A, and bandwidth, Δf. In terms of η_{ext} and i_n, the expression for D^* for a general detector is given as:

$$D^* = \frac{e\lambda}{hc}\eta_{ext}\sqrt{\frac{A\,\Delta f}{i_n^2}}. \tag{3.3}$$

3.1.2 Device Transport and Shockley-Ramo Theorem

In order to determine the ultimate sensitivity limit of a given detector structure, it is necessary to relate η_{ext} and i_n to the device design parameters and the structure material properties. This requires a model for the electron transport. For ideal (so-called diffusion-limited) detectors, these quantities are not independent [78,79], and should be calculated from the same transport model. This ensures that the design tradeoff between signal and thermal noise is established. We consider semiconductor devices where phase-coherent effects are not a critical part of the transport process. In this limit, the carrier transport can be described as arising from the exchange of electrons between the eigenstates of the structure's static Hamiltonian. We will assume that the transitions of electrons between the static eigenstates can all be considered as Markov processes. Consequently, the noise in the device arises from the statistical uncertainties in these transitions. To simplify the analysis, it is useful to sort the many eigenstates of the static Hamiltonian into groups of states, which we refer to as reservoirs. The dynamic interactions of the states within the same group is fast enough that they can be

considered to be in thermodynamic equilibrium, and thus share a common chemical potential. The dynamics between states with different chemical potentials is relatively slow. The detailed physics of this "discrete" transport picture has been developed by researchers in the mesoscopic physics [72,80], and quantum cascade detector communities [81-83]. Our model will closely follow these ideas, particularly those from Refs. 72 and 82.

A schematic representation of the discrete transport picture we are considering is shown in Fig. 3.1 for a device with four reservoirs. The semiconductor device is assumed to be held between two metallic contacts. The first contact is held at a constant potential of V_o, and the second is grounded. The 1^{st} and N^{th} reservoirs are assumed to be in equilibrium with the left and right contacts, respectively. We assume that the contacts provide large reserves of electrons,

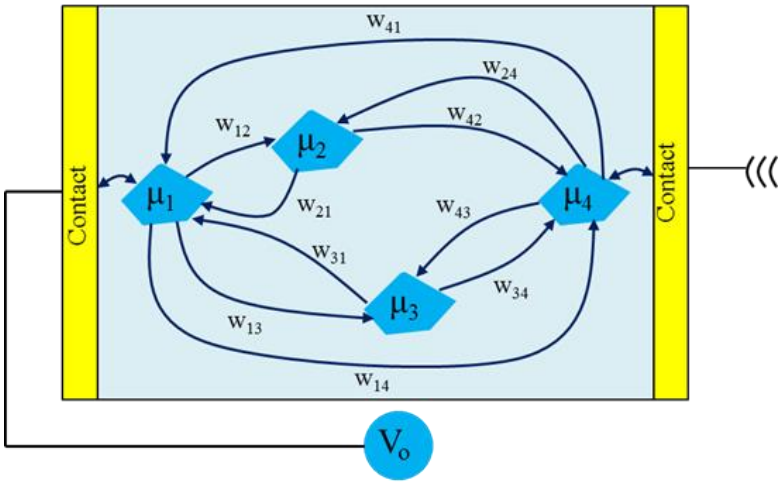

Figure 3.1: Schematic of an arbitrary semiconductor device where electron transport can be modeled as thermalized reservoirs exchanging electrons.

which act to replenish the steady-state occupation numbers in these reservoirs, so that the potential across the device remains constant. Transport of electrons through the device occurs as a result of the exchange of electrons between reservoirs. The transition rate of electrons from the i^{th} to j^{th} reservoir is denoted as w_{ij}. The transition rates between two reservoirs will depend on their relative disequilibrium, which is quantified by the difference in their chemical potentials.

To solve the transport problem, one must assume a form for this relationship between the chemical potential difference between two reservoirs and the transition rate. The problem is solved by finding the average rates, $\langle w_{ij} \rangle_t$, for a given value of V_o under the constraint that the current should be constant through the device.

The Shockley-Ramo theorem [80,84-86] provides a useful tool for analyzing transport in complex devices. This theorem connects the temporal change in the distribution of the device's internal electrons to the temporal signal delivered to the external circuit. This provides a more accurate description of current flow in devices than the conventional picture that charge flows in the external circuit only when carriers are collected at the contact. When applied to our discrete transport model, the theorem establishes that the transition of an electron between two of the reservoirs in the device yields an effective charge delivered to the external circuit that is proportional to the relative change in the electron's chemical potential before and after the transition. As seen in the subsequent analysis, this distinction in the interpretation of current flow is a critical consideration for proper treatment of the noise.

The essence of the Shockley-Ramo theorem is that the signal produced in a device's external circuit at a given time is caused by the exchange of energy between the device's internal electrons and the environment at the same instant. An essential assumption is that retardation effects are negligible. In the transport picture we are considering, signal is produced each time an electron transitions between reservoirs. As shown in Appendix A, the effective charge delivered to the circuit by an inter-reservoir transition can be deduced by considering the changes in the Gibb's free energy of the before and after the transition. Under the transport picture we are considering, the Shockley-Ramo theorem gives the instantaneous current in the device as:

$$i(t) = e\sum_{i,j}\alpha_{ij}f_{ij}\left(t - t_p^{ij}\right), \tag{3.4}$$

where α_{ij} is the percentage of the total voltage that is applied to the $i \rightarrow j$ transition. The times t_p^{ij} are sets of random variables indicating the times at which an electron is transferred between reservoirs i and j. The indices p of these random times range from 1 to N_{ij}, where N_{ij} is the total number of transitions from i to j in the observation time T_{obs}. The function $f_{ij}(t)$ gives the temporal pulse shape that characterizes the $i \rightarrow j$ transition. This can be more conveniently defined in terms of its Fourier transform:

$$f_{ij}(t) = \int_{-\infty}^{\infty}\frac{d\omega}{2\pi}F_{ij}(\omega)\exp(-i\omega t), \tag{3.5}$$

where $F_{ij}(\omega)$ is the Fourier amplitude of the pulse shape. We will assume a delta-like pulse for each transition, so that $F_{ij}(\omega) = 1$. Under this assumption, the time-averaged current, $\langle i \rangle_t$ can be written as:

$$\langle i\rangle_t = e\sum_{i,j}\alpha_{ij}\langle w_{ij}\rangle_t, \tag{3.6}$$

where $\langle w_{ij} \rangle_t$ indicates the average transition rate from i to j. From the Shockley-Ramo theorem, it can be seen that a given transition event between reservoirs i and j delivers an effective charge of $\alpha_{ij}e$ to the external circuit. Thus, α_{ij} is an indication of how much of a bottlenecking effect the $i \rightarrow j$ transition has in the overall path of an electron between the device contacts. This fact allows us to classify the various transitions as either macroscopically significant or insignificant, based on the effective charge that is delivered to the external circuit. Macroscopically significant transitions are the ones that play a role in determining the empirically measurable quantities such as the dc current and the noise frequency spectrum. Macroscopically insignificant transitions will not show any signatures in these measurements.

Now, we will consider the noise that arises from the fluctuations in the electron exchange between reservoirs. Often in the analysis of infrared detectors, the noise is split into various components. A common approach for finding the noise in the literature has been to simply write the total noise, *s*, as a sum of Johnson noise and shot noise components. This is expressed as:

$$s = \frac{4k_bT}{R} + 2e\langle i\rangle_t, \tag{3.7}$$

where *R* is the device resistance. This treatment assumes that Johnson and shot noise are independent phenomenon. The use of Eq. 3.7 in evaluating the detector noise is often attractive, because it allows the noise to be found from the measurement of the device's I-V characteristics, rather than having to be measured directly. Direct measurement of the detector noise can be difficult in practice because of the difficulty in isolating the device noise from the other sources of noise introduced by the experimental setup. However, this picture of Johnson and shot noises as independent phenomenon in infrared detectors has been criticized recently [83]. A more general criticism of this picture in analyzing solid state devices was given earlier by Landauer in 1993 [87]. In addition, experiments have shown deviations in the noise from the prediction of Eq. 3.7 when the detector is operated under a large reverse bias. In this operation regime, the noise is expected to approach the pure shot noise limit, which is given by the famous Schottky expression [69]:

$$s = 2e\langle i\rangle_t. \tag{3.8}$$

However, when measured directly, the noise in infrared detectors is often found to exceed this prediction. This problem has been known for some time in the MCT community [88], and recent experiments have shown excess noise in InAs/GaSb SL detectors as well [89,90]. The excess noise is usually classified as $1/f$ noise. This is because when the noise spectrum is measured, rather than having a uniform frequency-dependence, the noise at low frequencies tends to

increase as $1/f$. The source of the $1/f$ noise in infrared detectors is often speculated to be related to bulk or surface defects. There is some experimental evidence to support this conclusion. Notably, Tobin et. al. found a strong correlation between the noise in MCT photodiodes and the surface leakage current [91]. They were able to isolate the surface component of the current by measuring detectors fabricated from the same wafer, but with different areas for the mesa surface. Despite this evidence, the conventional theory has not been able to explain these effects, which has made it challenging to make the appropriate design modifications needed to lower the noise and improve the detector sensitivity.

A more reliable approach is to simply deduce the *total* noise directly from the instantaneous current equation provided by the Shockley-Ramo theorem, which is given in Eq. 3.4. In this treatment, the observed macroscopic noise is calculated directly from the temporal fluctuations in the transition rates between reservoirs, $w_{ij}(t)$. This provides a direct link between the microscopic phenomenon and the measurable quantities. In addition, although not done in this work, the theory should be useful for calculating the spectral distribution of the noise. This would provide a means for evaluating the excess noise observed in infrared detectors. Often, the models for $1/f$ noise attempt to find a relationship between the current fluctuations and the average current, $\langle i \rangle_t$, under dark conditions. However, this sort of treatment is inapplicable to devices such as Auger-suppressed detectors, where large noise is present under large reverse bias, even while the total dark current is reduced due to the reduced impact ionization generation [88].

In our application of the Shockley-Ramo theorem, we assume the voltage across the device is held fixed (i.e. not fluctuating) and that the α_{ij} values for a given transition are unaffected by the transition rate fluctuations from which the noise arises. The former

assumption is contingent on the external circuit having a negligible impedance. Dealing with the finite impedance of the circuit is a non-trivial problem [92], and we will assume that it's effects are minimal. The α_{ij} values will be fixed if the reservoir chemical potentials, μ_i, are fixed. The assumption of non-fluctuating chemical potentials for the reservoirs that are in equilibrium with the contacts, μ_1 and μ_N follows from the assumption of a fixed external voltage. The chemical potentials for the internal reservoirs will be fixed so long as the fluctuations of the transition rates between the reservoirs do not create large internal potentials. Although this assumption may not be valid in certain mesoscopic systems, as pointed out in Ref. 80, for devices such as cascade lasers or detectors this assertion should be valid.

The noise spectral density, $c(\omega)$, is related to the autocorrelation of the instantaneous current by the Wiener-Khinchin theorem, and is written as:

$$c(\omega) = \frac{1}{T_{obs}} |i(\omega)|^2 - 2\pi \langle i \rangle_t^2 \delta(\omega), \tag{3.9}$$

where $i(\omega)$ is the Fourier transform of $i(t)$ defined in Eq. 3.4. This quantity is evaluated as:

$$i(\omega) e \sum_{i,j} \sum_{p} \alpha_{ij} e^{i\omega t_p^{ij}}. \tag{3.10}$$

Squaring $i(\omega)$, we obtain:

$$|i(\omega)|^2 = e^2 \sum_{i,j} \sum_{k,l} \alpha_{ij} \alpha_{kl} \sum_{p} \sum_{s} e^{-i\omega\left(t_p^{ij} - t_s^{kl}\right)}. \tag{3.11}$$

We now split the sum over p and s into two different sums:

$$\begin{aligned} &\sum_{p} \sum_{s} e^{i\omega\left(t_p^{ij} - t_s^{kl}\right)} \\ &\qquad = \sum_{p} e^{i\omega(t_p^{ij} - t_p^{kl})} \delta_{ij,kl} + \sum_{p} \sum_{s} e^{i\omega\left(t_p^{ij} - t_s^{kl}\right)} (1 - \delta_{ij,kl}\delta_{p,s}). \end{aligned} \tag{3.12}$$

where the first sum is over the diagonal terms ($s=p$), and the second sum represents the non-diagonal terms. In the diagonal sum, the only non-zero terms are those where we are evaluating the difference between the same random time index from the same transition. Each of these terms is unity, and the overall sum over each of these terms evaluates to $N_{kl}\delta_{ij,kl}$. To evaluate the second sum, where the terms of the exponent are differences of unequal times, the sum over the t_p^{ij} times for a given time t_s^{kl} can be approximated as an integral [72,82]. The result of this approximation is: where $h_{ij,kl}(t)$ represents the $i\rightarrow j$ transition rate, given a $k\rightarrow l$ transition occurred at t=0. At times far from t=0 the transition rate $h_{ij,kl}(t)$ will lose all correlation with the $k\rightarrow l$ transition event at t=0 and will approach its mean value $h_{ij,kl}(t=\pm\infty)\rightarrow\langle w_{ij}\rangle$. Thus, we define the reduced correlator $g_{ij,kl}(t) = h_{ij,kl}(t) - \langle w_{ij}\rangle$, which indicates the transient time-dependence of the $i\rightarrow j$ transition rate in the vicinity of the $k\rightarrow l$ transition times. Far from these times $g_{ij,kl}(t) = 0$. We can now write:

$$|i(\omega)|^2 = e^2 \sum_{i,j}\sum_{k,l} \alpha_{ij}\alpha_{kl} N_{kl} \left[\delta_{ij,kl} + 2\pi\langle w_{ij}\rangle\delta(\omega) + \int_{-\infty}^{\infty} dt\, g_{ij,kl}(t) e^{-i\omega t}\right]. \tag{3.13}$$

By substituting this result for $|i(\omega)|^2$ into Eq. 3.9, we can get the general form of $c(\omega)$ for a given structure. In real devices, the relevant noise parameter is the one-sided noise spectral density, which is defined as: $s(\omega)=2c(\omega)$. This quantity can be split into two parts, $s(\omega)=s_o+s_{corr}(\omega)$. The first noise term, s_o, represents the noise without considering the transient behavior of $w_{ij}(t)$. This noise is Poissonian, and has no frequency dispersion. The second term represents a correction that arises when the correlations between events are considered. Because of our assumption of delta-like behavior of the transition pulses between reservoirs, the frequency dependence in the

total noise spectrum arises only from the correlations between transitions. The first portion of the noise, the uncorrelated noise term $s_{o,}$ is given by:

$$s_o = 2e^2 \sum_{i,j} \alpha_{ij}^2 \langle w_{ij} \rangle. \tag{3.14}$$

This s_o term resembles the Schottky noise expression given in Eq. 3.7. However, whereas the original Schottky formula only gives the current noise associated with the transport between two reservoirs, the expression in Eq. 3.14 provides a more general equation that includes the contribution from all the possible transport channel in a more complex device. The correlation noise term, $s_{corr}(\omega)$, is given by:

$$s_{corr}(\omega) = 2e^2 \sum_{i,j} \alpha_{ij}\alpha_{kl} \int_{-\infty}^{\infty} dt\, g_{ij,kl}(t) e^{-i\omega t}, \tag{3.15}$$

which we refer to as the "correlation correction" to the noise spectrum. The correlation correction can be obtained by using a master equation for the time-dependence of the conditional occupation probability of the reservoirs in the device [72,82]. The magnitude of this correction is given by a sum over the terms:

$$\alpha_{ij}\alpha_{kl}\langle \big(w_{ij}(t) - \langle w_{ij} \rangle_t\big) w_{kl}(0) \rangle_t.$$

If the transition rates $w_{ij}(t)$ deviate strongly from their mean values in the time immediately after a $k \rightarrow l$ transition, we will expect a strong correlation correction. When these terms are small, the noise can be approximated as the Poissonian s_o term. In the subsequent analysis of multiple-stage interband detectors, we will assume that the correlation correction to the noise is negligible, which should be valid as a first-order approximation.

3.1.3 Relationship of Signal-to-Noise in Multiple-Stage Detectors

Now, we apply this theory to the specific case of a multiple-stage interband infrared detector. The main goal in the subsequent analysis is to calculate the magnitude of performance improvement that may be possible for a given infrared detector material when a multiple-stage, rather than single-absorber architecture is utilized. We focus on the "ultimate" performance limit of a given material and device architecture. This represents the limit where the detector performance is determined bulk properties of the absorber material. In this spirit, we neglect a number of non-idealities that may be present in real devices. We assume that the barrier regions block all tunneling of their namesake carriers and act as ideal contacts for the opposite carrier. As a result of this assumption, the chemical potentials are spatially constant across these regions. In a real device, there may be some resistive or tunneling effects that must be accounted for when analyzing experimental data. We also assume that the structure has been designed so that the potential drop across the absorber is zero, and hence all electric fields are confined to the barriers. This can typically be achieved with a proper choice of barrier doping. A flat-band absorber design is often preferred for narrow-bandgap detectors in order to avoid detrimental tunneling currents. In addition, factors such as shunting effects and contact series resistance are neglected. These factors are expected to be minimal after sufficient maturation of the material growth and device fabrication techniques.

For many infrared detector materials, such as InAs/GaSb SLs, the cross-sections for microscopic processes such as phonon scattering and defect-assisted generation recombination are not well known. In addition, for SL materials these parameters will vary with the composition of an individual period. This precludes a more complete microscopic analysis such as those carried out for quantum cascade detectors in Ref. 93-94. Instead, we will connect our

theory with macroscopic parameters that average over the influence of all the microscopic events. These parameters are: the minority carrier diffusion coefficient, D_n, the nonradiative recombination time τ_{nr}, and the optical absorption coefficient, α. These parameters are more easily obtained experimentally than the microscopic cross-sections. Note that we are assuming that radiative recombination is a negligible process in the narrow-bandgap systems we are considering due to the prevalence of strong Shockley-Read-Hall and Auger processes. We will assume that the absorber material can be considered "bulk-like."

In the ultimate limit, the total current consists of separate forward and reverse currents. The forward current arises due to the injection of minority carriers from the contact (or opposite polarity barrier) into the absorber and their subsequent recombination. This current is referred to as the injection current. The reverse current consists of the generation of minority carriers in the absorber and their subsequent collection. This current is referred to as the collection current. The collection current arises both due to carrier generation induced by the incident photons and thermal generation.

Let us now consider how we can divide the individual states in a multiple-stage detector structure into reservoirs. First, let us consider the special case of $D_n \rightarrow \infty$. In this limit, all the minority carriers within a given stage are perfectly thermalized. This implies that all the generated minority carriers are collected. This is sometimes referred to as the infinite mobility limit in the solar photovoltaic literature. In this limit, the only transport bottlenecks come from the interband transitions across the absorber bandgaps. In this limit, the electrons can be clearly grouped into N_s+1 distinct reservoirs. In this case, an individual reservoir would consist of the electrons occupying conduction band states in the absorber and the hole barrier of one stage, and the electrons occupying valence band states of the absorber and electron barrier of the adjacent

stage to which it is connected via the type-II broken-gap window. This means that within a given stage, all of the absorber states in the conduction band have a single chemical potential that is different than the chemical potential of the valence band states in the same stage. For an internal stage, this chemical potential will be shared with the opposite band absorber states of one of the adjacent stages. In the first and last stages, either the conduction or valence band states will be in chemical equilibrium with the adjacent contact, depending on whether the contacts are hole- or electron-injecting. This gives a total of N_s+1 distinct chemical potentials in the device. The formation of these chemical potentials under reverse bias situation is shown in the Fig. 3.2, indicated as the $D_n \rightarrow \infty$ case (dotted line).

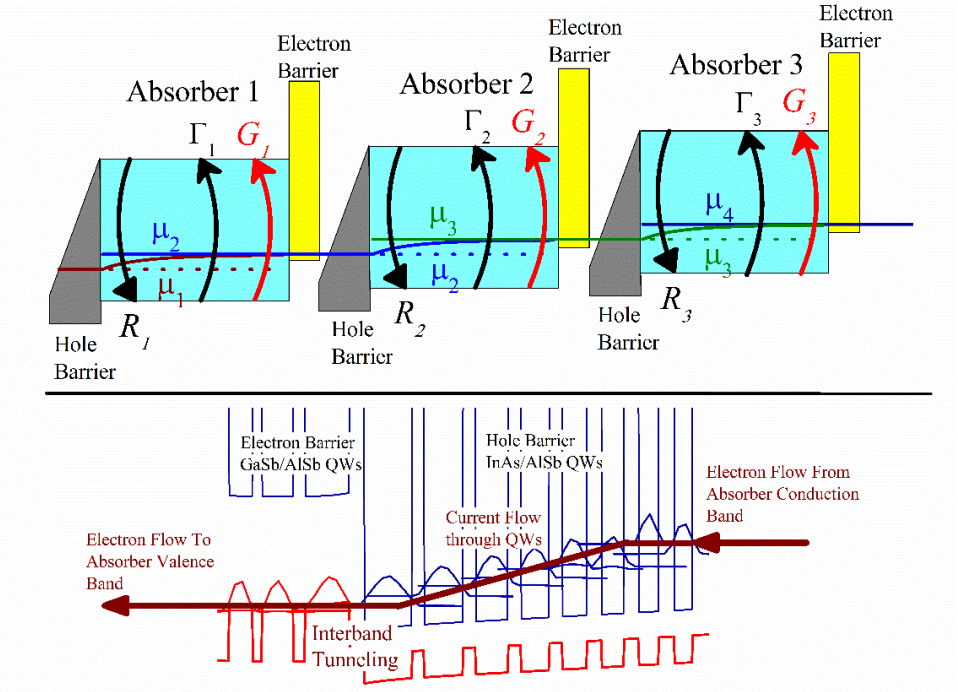

Figure 3.2: Schematic of an ICIP with equal-absorber thicknesses d under reverse bias. The direction of injection, R_i, thermal collection, Γ_i, and photo-collection currents, G_i, are indicated in each stage are indicated for the i^{th} stage. The four distinct chemical potentials that exist in the three stages are indicated for the case where $d=L$ (solid line) and $D_n \rightarrow \infty$ (dotted line). Also shown is the material composition of an ICIP near the interface of the electron and hole barriers, and the path than an electron takes as it travels between stages.

The overall picture becomes more complicated in the case where the collection process is no longer perfect. Carrier diffusion from the point of generation to the collection point provides an additional bottlenecking effect. Nevertheless, with some modifications to the theory, we can still retain the same overall picture. In this case, there are still N_s+1 distinct chemical potentials. However, electrons generated farther from the collection point have a greater probability of thermalizing with the valence electrons (i.e. recombining) before they are collected. Thus, the splitting of the two chemical potentials in a given stage will become smaller at points farther from the collection point.

Since the absorber material is treated as bulk-like, the chemical potential of all the electrons at a given point in the absorber varies continuously. For SL absorbers, we assume that the transport through the absorber is due to sequential well-to-well transport of the electrons through the material. Thus, although we describe the collections of eigenstates with similar energies in the SL absorber as "minibands", the "miniband transport" is a drift-diffusion process, rather than phase-coherent transport of delocalized electron waves. In a SL absorber, assuming that an electron in a given well only move sequentially to one of the adjacent wells, the diffusion coefficient can be expressed as:

$$D_n = \frac{(\delta x_w)^2}{\tau_w}, \tag{3.16}$$

where is the well-to-well transition time and Δx_w is the length of a single SL period. Note that an electron in a given SL well has an equal probability of transitioning to either of the two adjacent wells.

The spatial variation of the chemical potential across the three stages for the case where the minority carrier diffusion length, $L_n = \sqrt{D_n \tau_{nr}}$ was set equal to 1/3 of the absorber thickness, d is shown in Fig 3.2. As seen, the main difference between the $D_n \to \infty$ and the finite

D_n cases are that in the latter case the chemical potential of the minority carriers in the absorber has a spatial dependence. When D_n is finite the separation in the chemical potential between conduction band and valence band reservoirs of a given stage becomes smaller near the electron barrier. This is a consequence of the decreased collection probability for carriers farther from the collection point. A stronger separation in the chemical potentials across the stage is maintained when the absorber is made shorter than the diffusion length. Thus, it can be seen that when light is absorbed and collected in discrete intervals, it is easier to maintain good collection across the whole structure. This is why the multiple-stage architecture is able to maintain a good photovoltaic response even in situations where the material properties are not optimal.

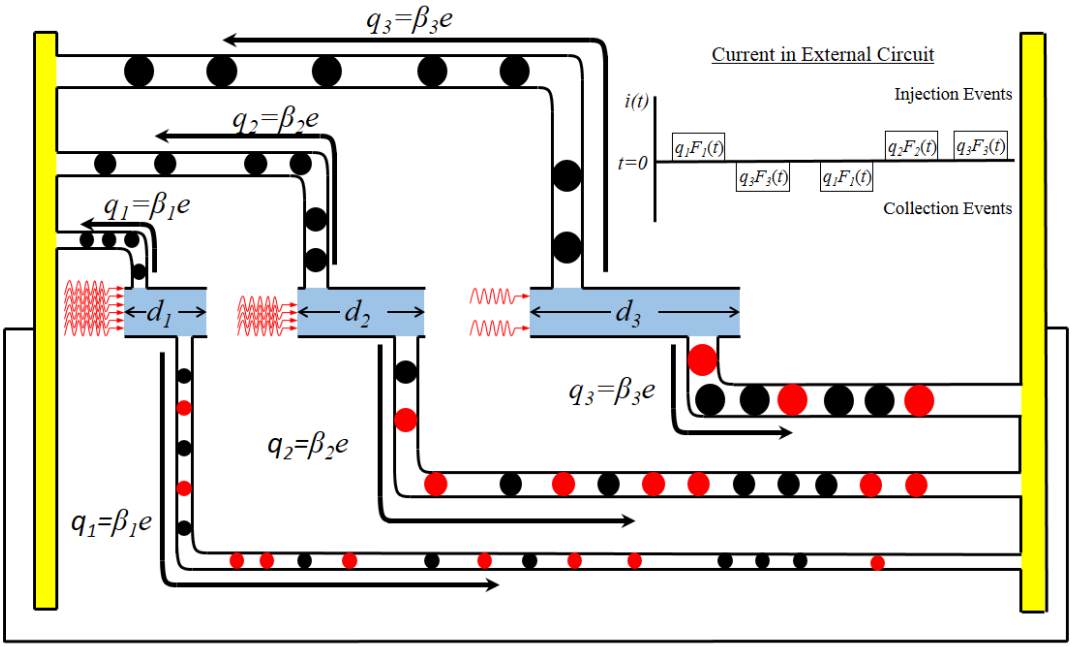

Figure 3.3: Circuit model for an ICIP found using Shockley-Ramo theorem. The black dots represent thermally generated or injected carriers. The red carriers represent photo-generated carriers. The inset shows the time-dependent signal. The squares represent the pulses of current produced when there is a transition between two reservoirs.

The signal and noise properties of multiple-stage detectors are determined by the statistics of the particle exchanges between these reservoirs. Using the Shockley-Ramo theorem,

it can be stated that in the time an electron moves across the m^{th} stage, an effective charge of $q_m=\beta_m e$ is delivered to the external circuit, where $\beta_m e$ is the percentage of the overall voltage that is applied to the m^{th} stage. This suggests that a multiple-stage detector can be thought of as stages acting in parallel rather than in series. A representation of this alternative picture of a three-stage detector is shown in Fig. 3.3. Each of the m stages with absorber thicknesses denoted as d_m can be thought of as a separate charge generator. In general, the $\beta_m e$ to either of the two contacts. The forward and reverse currents in a given stage are represented by the circles traveling from the stage to one of the contacts. The black circles represent thermal carriers, while the red circles represent photo-carriers. In the figure, the carrier injection process is represented by the carriers traveling to the left contact, and the carrier generation process is represented by carriers traveling to the right contact. The average rate of charge delivery from one of the stages to the contacts is fixed, and is determined by the injection and collection currents in the stage. However, there is an inherent uncertainty in the times at which charge is transferred from one of the stages to the contacts, due to the random nature of the physical processes that give rise to the current. This inherent statistical uncertainty is the source of noise in the device. Since the average total current must be equal in each stage this validates our assertion from Chapter 2 that introducing multiple stages into the device amounts to performing additional measurements of the current.

For a bulk-like absorber, the equation that governs the minority carrier density $n(x)$ and the chemical potential $\mu(x)$ is:

$$\frac{d}{dx}\left[\frac{D_n}{k_b T} n(x) \frac{d\mu(x)}{dx}\right] - \frac{n(x)}{\tau_{nr}} = -g(x), \tag{3.17}$$

where $g(x)$ is the interband carrier generation rate per unit volume. When the electric field is zero in the absorber, the relationship between $n(x)$ and $\mu(x)$ is given by:

$$k_b T \frac{d\mu(x)}{dx} = \frac{1}{n(x)} \frac{dn(x)}{dx}, \tag{3.18}$$

so the equation for $n(x)$ is now an diffusion equation:

$$\left[\frac{d^2}{dx^2} - \frac{1}{L_n^2}\right] n(x) = -\frac{g(x)}{D_n}. \tag{3.19}$$

Let us define the bottom edge of the m^{th} absorber as $x=x_m$. This point corresponds to the left edge of the absorber, as indicated in Fig. 3.2(b). The thickness of the m^{th} absorber is d_m, so the absorber extends from x_m to x_m+d_m. Note that we designate the d_m with higher index m as those that are optically deeper in the structure. Thus, for detectors designed for a single radiation pass, the higher the m index of d_m, the weaker the incident light is on that particular stage, due to the light absorption in the first m-1 stages. At $x=x_m$, all the generated carriers will be collected and the steady-state concentration will not be influenced by the limits of the diffusion collection. Let us define β_m as the percentage of the total applied voltage that falls across the m^{th} stage. At $x=x_m$, the electron concentration will be equal to the value that would be present if the conduction and valence band chemical potentials were flat across the absorber and separated by $\beta_m eV$. In other words, the concentration at this point should be the same as in the $D_n \rightarrow \infty$ limit considered earlier. This gives a boundary condition of:

$$n_m(x)|_{x=x_m} = n_o \exp(\beta_m eV/k_b T). \tag{3.20}$$

At the opposite end of the absorber, $x=x_m+d_m$, the minority diffusion current terminates at the interface between the absorber and the electron barrier. Ideally, the barrier should be perfectly reflecting, so that $J_n|_{x=xm+dm} = 0$. However, there may be some recombination of minority carriers due to impurity states in the barrier. If a surface recombination velocity of S_{eb} is used to characterize the recombination at the absorber-electron barrier interface, the boundary condition is:

$$\left.\frac{dn_m(x)}{dx}\right|_{x=x_m+d_m} = -\frac{S_{eb}}{D_n}[n_m(d) - n_o]. \tag{3.21}$$

For maintaining completeness of the theory, we will consider a nonzero S_{eb} in the theory development, though we will assume S_{eb}=0 in the analysis in Section III.

Eq. 3.19 has the form of the inhomogeneous Helmholtz equation. For this equation, we are interested in the solution of $n(x)$ under both the spatially uniform thermal generation rate (dark) and a generation rate with a negative exponential spatial variation (light). An elegant approach to this problem is to find a Green's function $G_m(x,x')$ from which we can calculate the distribution, and hence the current, under an arbitrary generation rate. The development of this reciprocity method is attributed to Donolato [95,96]. It has also been extended and utilized extensively by members of the solar PV community, since it provides an important link between the short-circuit current and open-circuit voltage of a solar cell [97-99]. To our knowledge, this is the first time this method has been applied to analyze photodetectors. Thus, we present a self-contained derivation in the hope of increasing awareness of this technique in the community.

The Green's function is found by solving the differential equation:

$$\left[\frac{d^2}{dx^2} - \frac{1}{L_n^2}\right] G_m(x, x') = \delta(x - x'), \tag{3.22}$$

with homogenous boundary conditions . The solution methods for obtaining a particular Helmholtz Green's function are well-known [100]. The complete derivation of the closed-form expression of the Green's function is given in Appendix B. Here we will summarize the main results that we use to analyze photodetectors. For a given spatial generation profile in the absorber, $g(x)$, the spatial electron concentration in the m^{th} stage, $n_m(x)$, can be expressed as:

$$n_m(x) = -n(x' = x_m)\left[\frac{d}{dx'}G_m(x,x')\right]_{x'=0} - \frac{n_o S_{eb}}{D_n}G_m(x,x')\Big|_{x'=x_m+d_m} - \int_{x_m}^{x_m+d_m} dx' G_m(x,x')\frac{g(x')}{D_n}. \tag{3.23}$$

We see that physically, the function $G_m(x,x')$ correlates the stationary carrier distribution at x to the carrier generation rate at x'. Thus, we expect $G_m(x,x')$ to have a maximum at $x=x'$ and to decay away from this point with a characteristic length given by diffusion length. The appropriate Green's function is given as:

$$G_m(x,x') = -L_n \sinh\left(\frac{x_<}{L_n}\right)\frac{\cosh\left[\frac{x_> - d_m}{L_n}\right] - \left(\frac{S_{eb}L_n}{D_n}\right)\sinh\left[\frac{x_> - d_m}{L_n}\right]}{\cosh\left(\frac{d_m}{L_n}\right) - \left(\frac{S_{eb}L_n}{D_n}\right)\sinh\left(\frac{d_m}{L_n}\right)}, \tag{3.24}$$

where $x_<$ represents the lesser value of x and x' and $x_>$ represents the greater value. A simpler function that is more useful for calculating experimentally observable quantities such as the current and voltage is the carrier collection probability, $f_{c,m}(x)$. This probability can be derived from $G_m(x,x')$. This function gives the probability that an electron at position x will diffuse to the collection point $x=x_m$ before recombining. The function $f_{c,m}(x)$ can be found by considering the condition of zero illumination. In this case, there is only thermal generation, which is uniform across the absorber (as shown in Appendix B). The result is:

$$f_{c,m}(x) = \frac{\cosh[(x_> - d_m)/L_n] + \left(\frac{S_{eb}L_n}{D_n}\right)\sinh[(x_> - d_m)/L_n]}{\cosh\left(\frac{d_m}{L_n}\right) + \left(\frac{S_{eb}L_n}{D_n}\right)\sinh\left(\frac{d_m}{L_n}\right)}. \tag{3.25}$$

Note that the spatial collection probability is related to the dark carrier distribution by:

$$n_m(x) = n_o\left[1 + f_{c,m}(x)\left(e^{e\beta_m V/k_b T} - 1\right)\right], \tag{3.26}$$

and the relationship between the chemical potential for conduction band states across the m^{th} stage, $\mu_m(x)$, and the carrier distribution is given by:

$$\frac{\mu_m(x)}{k_b T} = \frac{\mu_{o,m}}{k_b T} + \ln\left(\frac{n_m(x)p_o}{n_i^2}\right), \tag{3.27}$$

where $\mu_{o,m}$ is the chemical potential for valence band states in the m^{th} stage. The relationship between $\mu_{o,m}$, $\mu_{o,m+1}$, and the total applied bias is given by:

$$\mu_{o,m+1} - \mu_{o,m} = e\beta_m V, \tag{3.28}$$

Now, we can use the functions $f_{c,m}(x)$ and $G_m(x,x')$ to evaluate the expressions for η_{ext} and s_o. The total current in a given stage is given by the difference of the forward injection current and the reverse collection current. The injection current flowing in the m^{th} stage, R_m, is bias-dependent, and thus is determined by the amount of bias that is applied to a given stage. As stated above, the collection current consists of a thermal collection current, Γ_m, and a photo-collection current, W_m. Note that R_m, Γ_m, and W_m are particle current densities. The corresponding electric current densities are related by a factor of electric charge. From Eq. 3.14, we can write s_o for a multiple-stage detector as a weighted sum of the current components of each stage, given as:

$$s_o = 2e^2 A \sum_{m=1}^{N_s} \beta_m^2 (\Gamma_m + R_m + W_m). \tag{3.29}$$

We have used the assertion that the voltage applied to a given stage is equal to the change in the chemical potential as an electron moves across the stage.

Before discussing noise in more detail, let us address the signal portion. There are two types of illumination geometries that should be considered. The first is the geometry where the light is incident on the absorber from the collection point, and thus travels through the structure in a direction opposite to the flow of minority carriers. When the absorber is p-doped, the minority carrier collection point is located at $x=x_m$, as indicated in Fig. 3.2. Consequently, for the figure schematic, light coming toward the absorber from the right-hand side would be considered

incident from the collection point. In the other illumination geometry, the light is incident opposite to the collection point, so that the incident photons travel through the structure in the same direction as the minority carrier flow. For obtaining a larger signal, the former geometry, where the light is incident from the collection point is preferable, since with this choice the average collection probability of the photo-excited electrons will be larger.

For the p-doped absorber we are considering, the spatial variation of the photogeneration across the m^{th} absorber is given by: $Q_m(x) = \Phi_m \alpha e^{-\alpha(x-x_m)}$, where Φ_m is the photon flux incident on the m^{th} stage. When light is incident opposite to the collection point, the photogeneration across the absorber is given by $Q_m(x) = \Phi_m \alpha e^{-\alpha[d-(x-x_m)]}$. The individual quantum efficiency of the m^{th} stage in a detector is given by:

$$\eta_{d_m} = \Phi_m^{-1} \int_{x_m}^{x_m+d_m} dx\, Q_m(x) f_c(x). \tag{3.30}$$

When light is incident on an absorber with length d from the collection point, the individual quantum efficiency is given by:

$$\begin{aligned} &\eta_d \\ &= \left[\frac{\alpha L_n}{1-(\alpha L_n)^2}\right] \\ &\times \left[\frac{\left(1-\frac{\alpha L_n S_{eb} L_n}{D_n}\right)\sinh\left(\frac{d}{L_n}\right)+\left(\alpha L_n-\frac{S_{eb}L_n}{D_n}\right)e^{-\alpha d}+\left(\frac{S_{eb}L_n}{D_n}-\alpha L_n\right)\cosh(\frac{d}{L_n})]}{\cosh(d/L_n)+\left(\frac{S_{eb}L_n}{D_n}\right)\sinh(d/L_n)}\right], \end{aligned} \tag{3.31}$$

and when the light is incident opposite to the collection point, the individual quantum efficiency is given by:

$$\eta_d = \left[\frac{\alpha L_n}{1-(\alpha L_n)^2}\right] \times \left[\frac{\left(1+\frac{\alpha L_n S_{eb} L_n}{D_n}\right)\sinh\left(\frac{d}{L_n}\right)e^{-\alpha d} + \left(\alpha L_n + \frac{S_{eb}L_n}{D_n}\right)\cosh\left(\frac{d}{L_n}\right)e^{-\alpha d} - \alpha L_n - \frac{S_{eb}L_n}{D_n}]}{\cosh(d/L_n) + \left(\frac{S_{eb}L_n}{D_n}\right)\sinh(d/L_n)}\right]. \quad (3.32)$$

These expressions reduce to the expressions of Ref. 101 in the limit where $S_{eb}\rightarrow 0$. For the sake of clarity, let us also briefly consider the case of a detector using absorbers with n-type doping. For the setup in Fig. 3.2, if the absorber is n-doped, the collection point for the minority holes will be at $x=x_m+d_m$, which is the interface of the absorber and the electron barrier. Thus, for an n-type absorber, light incident from the collection point corresponds to light coming to the absorber from the right side of the schematic in Fig. 3.2. The expression in Eq. 3.31 is valid for describing the quantum efficiency of such a detector, so long as we replaced L_n, D_n, and S_{eb} with the corresponding parameters for minority holes. Similarly, for the alternative case, where light is incident on an n-type absorber from $x=x_m$, Eq. 3.32 holds, provided the parameters for minority holes are utilized. Thus, in modeling the quantum efficiency of a stage, the choice of Eq. 3.31 or Eq. 3.32 depends on the direction of the light traveling through the structure relative to the direction of the minority carrier flow.

If the incident photon intensity is denoted as Φ_o, the photo-collection current, W_m, that flows in the m^{th} stage is given as:

$$W_m = \Phi_o \eta_{ext} = \Phi_o \left[\prod_{j=1}^{m-1} \exp(-\alpha d_j)\right] \eta_{d\,m}, \quad (3.33)$$

where the bracketed term accounts for the effects of light attenuation.

Now let us apply $f_{c,m}(x)$ to find the thermal injection and collection currents. These two currents can be related by the principle of detailed balance. This relationship is given by:

$$R_m = \Gamma_m \exp(e\beta_m V/k_b T). \tag{3.34}$$

Thermal collection current is produced by the collection of thermally generated carriers in the bulk part of the absorber, as well as those generated at the absorber-electron barrier interface. For Γ_m, we have:

$$\begin{aligned}\Gamma_m &= f_c(d) n_o S_{eb} \\ &\quad + g_{th} \int_{x_m}^{x_m+d_m} dx\, f_c(x) \\ &= n_o \tau_{nr}^{-1} L_n \left[\frac{\left(\frac{S_{eb}L_n}{D_n}\right)\cosh\left(\frac{d}{L_n}\right) + \sinh(\frac{d}{L_n})}{\left(\frac{S_{eb}L_n}{D_n}\right)\sinh\left(\frac{d}{L_n}\right) + \cosh(\frac{d}{L_n})} \right].\end{aligned} \tag{3.35}$$

In the thermal noise limit, we can now write the value for s_o in terms of the material parameters as:

$$\begin{aligned}s_o &= 2e^2 A g_{th} L_n \\ &\quad \times \sum_{m=1}^{N_s} \left\{ \beta_m^2 \left[e^{\beta eV/k_b T} + 1 \right] \left[\frac{\left(\frac{S_{eb}L_n}{D_n}\right)\cosh\left(\frac{d_m}{L_n}\right) + \sinh\left(\frac{d_m}{L_n}\right)}{\left(\frac{S_{eb}L_n}{D_n}\right)\sinh\left(\frac{d_m}{L_n}\right) + \cosh\left(\frac{d_m}{L_n}\right)} \right] \right\}.\end{aligned} \tag{3.36}$$

From this expression, we see that each individual stage can be thought of as separate Poissonian charge generator. Under this picture, an injection/collection event in the m^{th} stage results in the delivery of an effective charge of positive/negative $e\beta_m$ to the external circuit. The average dark electrical current that flows through the device is given by:

$$J_d(V) = en_o\tau_{nr}^{-1}L_n$$

$$\times \sum_{m=1}^{N_s} \left\{ \beta_m \left[e^{\beta eV/k_bT} - 1 \right] \left[\frac{\left(\frac{S_{eb}L_n}{D_n}\right)\cosh\left(\frac{d_m}{L_n}\right) + \sinh\left(\frac{d_m}{L_n}\right)}{\left(\frac{S_{eb}L_n}{D_n}\right)\sinh\left(\frac{d_m}{L_n}\right) + \cosh\left(\frac{d_m}{L_n}\right)} \right] \right\}, \quad (3.37)$$

where it should be noted that the individual current flowing through each stage will be equal.

3.2 Finite Collection Limits of Single-Absorber Detectors

As stated in Chapter 1, the requirement for creating a device that operates as a photovoltaic is an architecture that steers conduction band carriers in the absorber to one contact and valence band carriers in the absorber to the other contact. A basic schematic an arbitrary single-absorber photovoltaic detector with a p-doped absorber region of thickness *d* is shown in Fig. 3.4. The "electron barrier" and "hole barrier" in the schematic can be realized with the use of doping gradients or heterostructures.

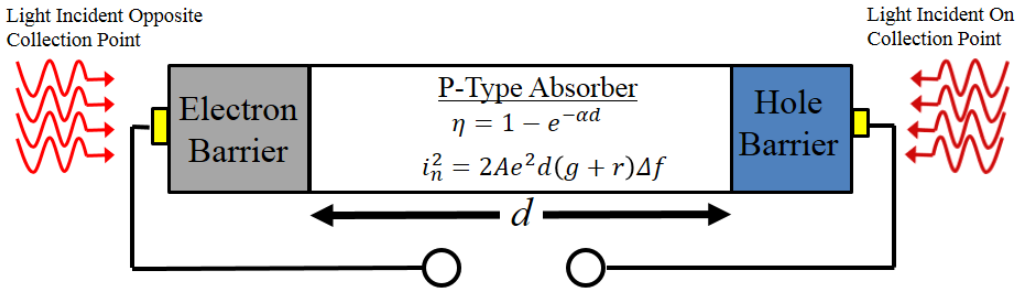

Figure 3.4: Photovoltaic detector with single absorber of thickness *d*. The absorber is p-doped, so the generated electrons are collected at the interface of the absorber and the hole barrier.

A model for treating an arbitrary single-absorber PV detectors in the $D_n \to \infty$ limit was presented by Piotrowski and coworkers [78,79]. In their treatment, they defined the ultimate performance limit as the case where the performance was limited by the bulk material properties of the material. Thus, non-idealities introduced by series resistance, surface generation-recombination effects, and non-ideal contacts are not included in the ultimate limit. In addition, since they assumed that $D_n \to \infty$, all the carriers generated in the absorber (both photo-generated

and thermally generated carriers) are collected and produce charge flowing in the external circuit. When all absorbed carriers contribute to the photocurrent, the detector quantum efficiency, is given by:

$$\eta = 1 - e^{-\alpha d}, \tag{3.38}$$

and the noise current is given by:

$$i_n^2 = 2Ae^2 d(g + r)\Delta f, \tag{3.39}$$

where g and *r* are the generation and recombination rates in the absorber and Δf is the detector bandwidth. The bandwidth is related to the integration time by:

$$\tau_{int} = {}^{1}/_{2\Delta f}. \tag{3.40}$$

In this limit, the value of *D** is given by [79]:

$$D^* = 0.31\ x\ k \frac{\lambda}{hc} \frac{1 - e^{-\alpha d}}{\sqrt{2(g + r)d}}, \tag{3.41}$$

where for a single-pass of radiation k is a number that varies between 1 and $2^{1/2}$ depending on the magnitude of the reverse bias. It can be seen from Eq. 3.41 that detectors operating in the thermal noise limit will have a tradeoff between signal and noise as the absorber is made thicker. When the detector is made longer, the value of η becomes larger. However, the thermal noise is also enhanced. The tradeoff comes from the fact that the generation rate for photocarriers exponentially decays at points deeper in the absorber, while the thermal generation rate is constant across the absorber. The *D** value in Eq. 3.41 is maximized by the optimal absorber thickness, d_{opt}, which is given by:

$$d_{opt} = \frac{1.26}{\alpha}. \tag{3.42}$$

This thickness gives the optimal quantum efficiency for a thermal-noise limited detector in the $D_n \rightarrow \infty$ limit as: η_{opt}=71%.

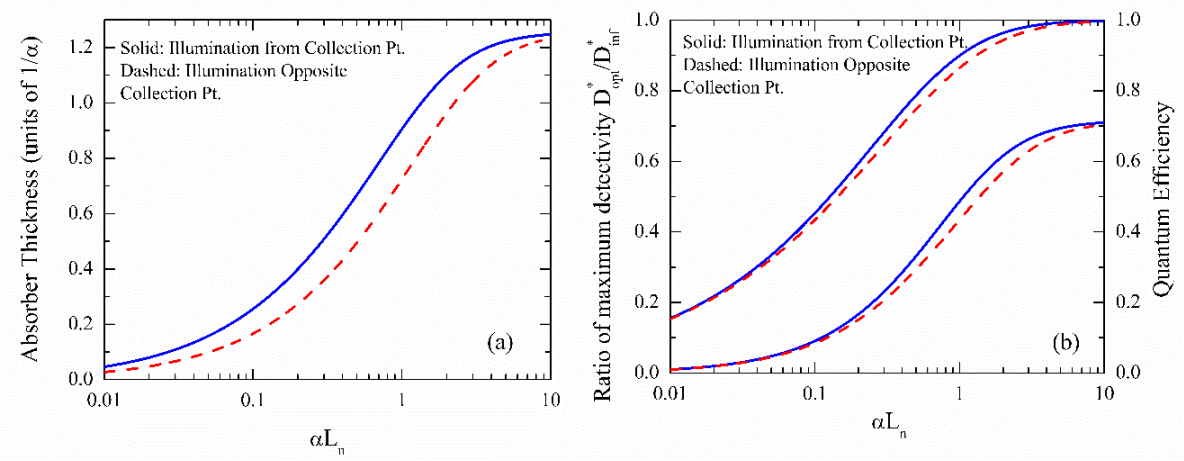

Figure 3.5: Variation of the performance of optimized single-absorber photovoltaic infrared detector as a function of absorber material parameter αL_n. The results corresponding to an optical signal incident from the minority carrier collection point are indicated by the solid line and the results corresponding to an optical signal from opposite the collection point are indicated by the dashed line. (a) The variation of the optimal absorber thickness in units of the absorption depth. (b) The variation of the quantum efficiency and optimal detectivity D^*_{opt}, for a detector that utlizes the optimal absorber thickness. The optimal detectivity values are normalized to the corresponding value evaluated in the infinite mobility limit.

Multiple-stage detectors have the potential to achieve better sensitivity than single-absorber detectors in the limit where the carrier collection of the generated carriers in the absorber is limited by a slow diffusion process. Thus, it is useful to quantify how the performance of an infrared detector is limited by the finite diffusion coefficient. Using the theory developed above, the ultimate limit can be extended to include the effect of finite carrier collection.

The limiting effects of imperfect carrier collection on the potential performance of a single-absorber detector can be judged by the product of the absorption coefficient and the diffusion length of the material. A low value of implies that a single-absorber detector will be unable to convert a large percentage of the incident photon flux to photocurrent, because the total number of electrons excited within a diffusion length of the collection point will be low. The influence of the finite collection properties of the absorber on the maximum D^* of a single-

absorber detector is shown in Fig 3.5. As seen, the analysis was done over a range of αL_n values from 0.01 to 10, and considered both light incident on the absorber from the collection point and light incident opposite the collection point. The configuration of an optimized detector was deduced by identifying the αd values that maximized the value of D^*. Fig 3.5(a) shows the optimal choice of αd corresponding to a given value of αL_n. It is seen optimal choice for αd is reduced for lower αL_n. This is because for smaller αL_n, the chance of collecting the carriers generated farther from the collection point is reduced. Fig 3.5(b) shows the variation of the optimized single-absorber detectivity, D^*_{opt}, and corresponding quantum efficiency. The detectivity is normalized to the value evaluated in the $D_n \rightarrow \infty$ limit, D^*_{inf}. As expected, the choice of αd for an optimized detector approaches 1.26 for high αL_n with a corresponding quantum efficiency of ~71% [79]. From Fig. 3.5, one can see that the attainable D^* and the corresponding quantum efficiency for a single-absorber PV detector decrease when the diffusion length is reduced. The influence of the limited collection on the detector performance can be seen when αL_n is smaller than 1.

3.3 Multiple-Stage, Equal-Absorber Detectors

3.3.1 Detectors Optimized for High-Speed Operation

The theory developed above will now be applied to compare the ultimate limits of single-absorber and multiple-stage detectors. First, we will consider a multiple-stage detector composed of N_s stages, where the absorber lengths in each stage are equal to the same value. This length is denoted as d. As stated above, for a detector designed for only a single pass of radiation, the external quantum efficiency of an identical-stage detector will be limited by the photo-collection current in the optically deepest stage. This is the last stage through which the incident light passes. The expression for η_{ext} is given as:

$$\eta_{ext} = \eta_d \exp[-\alpha d(N_s - 1)], \tag{3.43}$$

where η_d is given by Eq. 3.31 when the signal is incident on the absorber from the collection point and Eq. 3.32 when the signal is incident opposite to the collection point. In the case of $J_d >> J_{rad}$, the voltage is distributed equally across each stage, so $\beta_j = 1/N_s$. This gives the value of D^* as:

$$D^* = \frac{\lambda}{hc}\sqrt{N_s}\,\frac{\eta_d \exp[-\alpha d(N_s - 1)]}{\sqrt{(r+1)2\, g_{th} L_n \tanh(d/L_n)}}, \tag{3.44}$$

where r is a number ranging between 0 and 1 that indicates how much of the noise is due to recombination. Explicitly, r is equal to: $\exp(eV/N_s k_b T)$. At zero bias, there is full recombination noise, and r=1. Under saturation bias, there is no recombination noise and r=0. It can be seen that when the stages of a multiple-stage detector are made identical, there is a tradeoff between higher signal and lower noise as the number of stages increases. Adding further stages to an equal-absorber ICIP reduces the thermal noise, but also reduces the overall signal current, because of light attenuation in the optically deeper stages. From Eq. 3.44 we can deduce that the optimal number of stages to maximize the D^* of an equal-absorber ICIP operating in the thermal noise limit is given as:

$$(N_s)_{opt} = (2\alpha d)^{-1}. \tag{3.45}$$

Let us first address how the multiple-stage architecture can be advantageous for realizing intrinsically fast interband infrared detectors without overly compromising the sensitivity. The detector's intrinsic response time is determined by the time it would take the signal current to decay to zero if the optical signal were switched off. This signal-quenching time is itself determined by the time it takes a photo-excited electron to move across the conduction band of the absorber and through the barrier regions to the valence band of the next stage. Two ways to reduce the response time of a standard photodiode are to shorten the absorber length or to

introduce a built-in electric field in the absorber. Using a short absorber ensures that all the generated electrons in a given stage are collected relatively quickly. Introducing a built-in field increases the speed with which photogenerated electrons traverse through the absorber conduction band. However, taking either of these steps to improve the temporal response can result in a lower sensitivity. As mentioned above, the introduction of a built-in electric field will likely be accompanied by parasitic tunneling currents, which can result in additional noise. Shortening the absorber thickness will reduce the quantum efficiency. Here, we show that the tradeoff between response time and sensitivity that results from shortening the absorber can be made less severe by using a multiple-stage architecture. This is perhaps the most obvious advantage of multiple-stage detectors. In particular, we look at the limit where $d << L_n$ and $d << 1/\alpha$. We reiterate that we are neglecting the correlation effects in our treatment, and hence the frequency-dependence of the noise spectral density. The validity of this assumption is less certain for detectors operating in the high-speed regime. Thus, the following analysis should be considered as a first-order approximation, and more investigations may be needed to confirm the conclusions.

The value of η_{ext} for the short-absorber case is given by:

$$\eta_{ext} = e^{-\alpha d(N_s-1)}(1 - e^{-\alpha d}) \cong \alpha d e^{-\alpha d(N_s-1)}, \tag{3.46}$$

where we have set $\eta_d = \alpha d$, which is valid to first order in αd. Also, we can make the approximation: $\tanh(d/L_n) \cong d/L_n$, which gives $i_n^2 = 2e^2 A(r+1) g_{th} d\Delta f$. In this limit, the thermal-noise-limited detectivity can be written as:

$$D^* = \left[\frac{\lambda}{hc}\frac{\alpha d}{\sqrt{2(r+1)g_{th}d}}\right]\sqrt{N_s}\exp[-\alpha d(N_s-1)], \tag{3.47}$$

for both light incident from and opposite to the collection point. The bracketed term in Eq. 3.47 represents the detectivity of a single-absorber PV detector with absorber thickness d. The effect

of adding additional stages can be seen more clearly by expanding the last exponential term as a series:

$$D^* = D^*_{sing}\sqrt{N_s}\left[1 - \alpha d(N_s - 1) + \frac{(\alpha d)^2}{2!}(N_s - 1)^2 - \cdots\right]. \quad (3.48)$$

It is seen that in the short-absorber limit, when the chosen N_s is less than order $1/\alpha d$, the first term in the sum dominates. This gives the $N_s^{1/2}$ scaling predicted previously for this limit [12]. However, as the number of stages is made larger, the limit imposed by light attenuation in the latter stages becomes significant, and the higher order terms in the sum are no longer negligible. So we see that the ICIP should offer benefits in achieving higher *D** and faster response if the product of αd is fairly low.

To put this result into context, let us compare the potential performance of a single- and multiple-stage detector for the case where we have an absorber with α=2000 cm^{-1} and wish to achieve a high response speed by setting d=100 nm. For the multiple-stage detector, d represents the thickness of the absorber in each of the stages. Although the multiple-stage detector has a longer overall structure, the response time of this device is expected to be similar to the single-absorber detector, since speed is determined by the collection time in a given stage. To optimize the detector sensitivity of the multiple-stage detector, we should chose $(N_s)_{opt}$ = 25, if it is operating in the thermal noise limit. From Eq. 3.48, we see that this results in a detector with a ~3 times higher value of *D** than would be achieved using a single-absorber detector with the same value of d. This illustrates how the multiple-stage architecture can be utilized to increase the detector response speed with less compromising of the sensitivity.

3.3.2 Detectors Optimized for Highest Sensitivity

Now let us consider a circumstance where the application priority is achievement of high sensitivity, rather than a fast response. From Eq. 3.44, it can be seen that the magnitude of the

improvement possible with the use of a multiple-stage architecture is a function of the product αL_n of the absorber material. When this product is less than unity, it implies that a significant amount of light is absorbed at points far from the collection point, and that the collection-improving properties of multiple-stage detectors may be beneficial in improving the sensitivity. Since we expect the benefit of a multiple-stage architecture to be best in the limit where $\alpha L_n << 1$, let us first estimate the sensitivity for this limiting case. In this limit, short absorbers ($d/L_n << 1$) are preferable. Thus, as in the analysis above, we can make the approximations $\eta_{ind} \cong \alpha d$ and $\tanh(d/L_n) \cong d/L_n$. This gives the detectivity as:

$$D^* = \frac{\lambda}{hc}\sqrt{N_s}\frac{\alpha d}{\sqrt{2(r+1)g_{th}d}}\exp(-\alpha d N_s). \tag{3.49}$$

The detector can be optimized for the highest detectivity by choosing the number of stages in accordance with Eq. 3.45. With this choice for N_s, the optimized detectivity, D^*_{opt}, in this limit is:

$$D^*_{opt} = \frac{\lambda}{hc}\frac{\exp(-1/2)}{2\sqrt{r+1}}\sqrt{\frac{\alpha}{g_{th}}}. \tag{3.50}$$

This derived expression for the $\alpha L_n << 1$ limit is actually a good approximation for the optimized detectivity when $\alpha L_n < 0.2$. Also in this limit, the optimized ICIP absorption quantum efficiency, which we define as the total percentage of incident photons that are absorbed by the structure, is given by:

$$\eta_{abs} = 1 - \exp(-\alpha d N_s) = 1 - \exp(-1/2), \tag{3.51}$$

which numerically evaluates to 39%. The particle conversion efficiency, which we define as the percentage of incident photons that are converted to useful electrons, is given by $\eta_{part} = N_s\eta_{ext}$, and for an optimized multiple-stage detector is equal to:

$$\eta_{part} = \frac{1}{2\alpha d}\exp(-\alpha d[N_s - 1])\alpha d \cong \frac{\exp(-1/2)}{2}, \tag{3.52}$$

which numerically evaluates to ~30% for the case where $N_s = (2\alpha d)^{-1}$. Now, let us compare the optimized multiple-stage device result with a single-absorber detector in the same limit. A detector with a single, long absorber in the αL_n<<1 limit has a quantum efficiency given by:

$$\eta_{ext} = 1 - \exp(-\alpha L_n) \cong \alpha L_n. \tag{3.53}$$

We also make the approximation $\tanh(d/L_n) \cong 1$ for a long absorber. This gives a single-absorber detectivity of:

$$D^*_{sing} = \frac{\lambda}{hc}\frac{\alpha L_n}{\sqrt{2(r+1)g_{th}L_n}}. \tag{3.54}$$

We can now deduce the "detectivity enhancement" that is possible from a multiple-stage architecture in the αL_n<<1 limit. We define this as the ratio of the detectivity of an optimized multiple-stage detector, D^*_{mult}, to that of an optimized single-absorber detector. Using Eq. 3.50 and Eq. 3.54, we estimate this as:

$$\frac{D^*_{mult}}{D^*_{sing}} \cong \frac{\exp(-1/2)}{\sqrt{2\alpha L_n}}. \tag{3.55}$$

Thus, we estimate that the benefit provided by the use of identical-stage ICIPs scales as $(\alpha L_n)^{-1/2}$ when the absorber parameter αL_n is small. We can now compare this analytic estimate with a numerical optimization. For this analysis, we utilized the full D^* expression given in Eq. 3.44. The optimal single-absorber detector was found by optimizing the absorber thickness for maximum D^*. The optimal ICIP was found by optimizing both the absorber thickness and the number of stages. This was done for a range of αL_n values from 0.01 to 1, and for both illumination geometries. The results showing the calculated detectivity enhancement are given in Fig. 3.6. These values are compared with the analytic approximation given in Eq. 3.55. Also

shown is the optimal number of stages for the multiple-stage detector as a function of αL_n found from the numerical optimization.

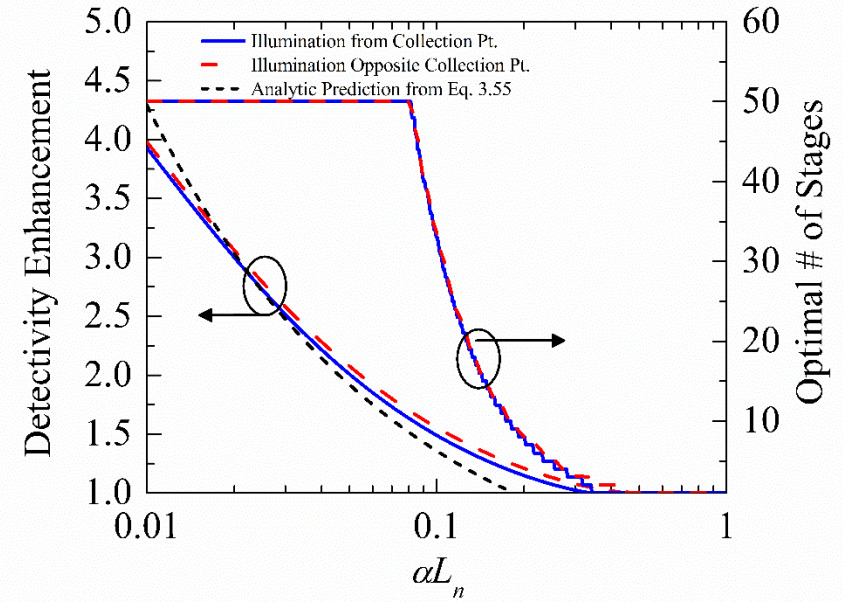

Figure 3.6: Theoretical detectivity enhancement for multiple-stage ICIPs with identical stages operating in thermal noise limit as a function of the αL_n product of the absorber material. The values were obtained by finding the optimal single-absorber and ICIP detector designs design using numerical optimization. The values are shown both for when light is incident on the absorber from the absorber's collection point and when it is incident opposite to the collection point. The enhancement factors obtained from numerical optimization were compared with the analytic approximation for this factor given in Eq. 3.55 from the text. For the numerical results the maximum number of stages was set to be 50.

From the numerical optimization, it was found that the multiple-stage detector can have superior performance for αL_n less than ~0.4. However, above this value of αL_n, the detectivity enhancement was equal to 1, which means that an optimized multiple-stage detector had N_s=1. Note that for the numerical optimization, the maximum number of stages was set as 50. This was the number of stages used for the multiple-stage device for $\alpha L_n < 0.08$. This is the reason that the analytic prediction for D^* enhancement is higher than the numerical values in the range of $\alpha L_n < 0.02$. For very low values of αL_n, the optimal number of stages becomes quite large (e.g. greater than 1000 for $\alpha L_n < 0.02$). In this range, the analytic approximation in Eq. 3.55

actually represents the theoretical limit for detectivity improvement if the number of stages were allowed to be very large. For higher values of αL_n, it is seen that the analytic prediction still provides a fairly good estimate of the possible detectivity enhancement, but does underestimate the numerical value. As earlier stated, Eq. 3.50 provides a good approximation for the detectivity of an optimized multiple-stage device for $\alpha L_n < 0.2$. However, Eq. 3.54 overestimates the detectivity of a single-absorber detector in this limit, due to an overestimate of the quantum efficiency. This is why the analytic expression underestimates the possible detectivity enhancement in the range of $\alpha L_n > 0.2$.

3.4 Multiple-Stage, Photocurrent-Matched Detectors

3.4.1 Thermal Noise Limit

From the results shown in Fig. 3.6, we see that if we set each absorber to have equal lengths, there will only be appreciable improvements in the sensitivity when the absorber parameter αL_n is less than 0.2. This is because the incident photons are still not used very efficiently, even with the improved collection of absorbed carriers provided by the multiple-stage design. This can be seen from Eq. 3.52 and Eq. 3.53, which show that for an optimized multiple-stage detector in the $\alpha L_n << 1$ limit, the overall absorption and particle conversion efficiency are below 50%. A way to improve the overall particle conversion efficiency is to utilize a "photocurrent-matched" multiple-stage design. In this type of design, the absorber thicknesses are varied throughout the structure so that an equal photo-collection is achieved in each stage when the device is illuminated. Consequently, this approach enables the most efficient usage of the incident photons. One downside is that this design limits the amount of thermal noise reduction that can be achieved by reverse biasing the detector. For stages with equal-length absorbers (both single- and multiple-stage), the noise from the injection current can be

completely quenched under reverse bias, which is the case when r=0 in Eq. 3.44. For ideal detectors, this enables the possibility of a $2^{1/2}$ detectivity improvement compared to the value zero-bias. However, in multiple-stage detectors designed for photocurrent-matching, the injection current noise can only be eliminated in the stage with the shortest absorber. This is because stages with longer absorbers must have some injection current to balance the larger generation rates in order to achieve an equal total current in each stage. Any reverse bias increase beyond that required for current saturation is applied to the stage limiting the current (i.e. the one with the smallest absorber). This continues until this stage reaches it's reverse-bias breakdown voltage. In addition to the limited ability to reduce the noise, detectors with a large number of stages may require extra iterations of structure growth in order to empirically achieve photocurrent-matching, especially if the spectral absorption coefficient is not accurately known.

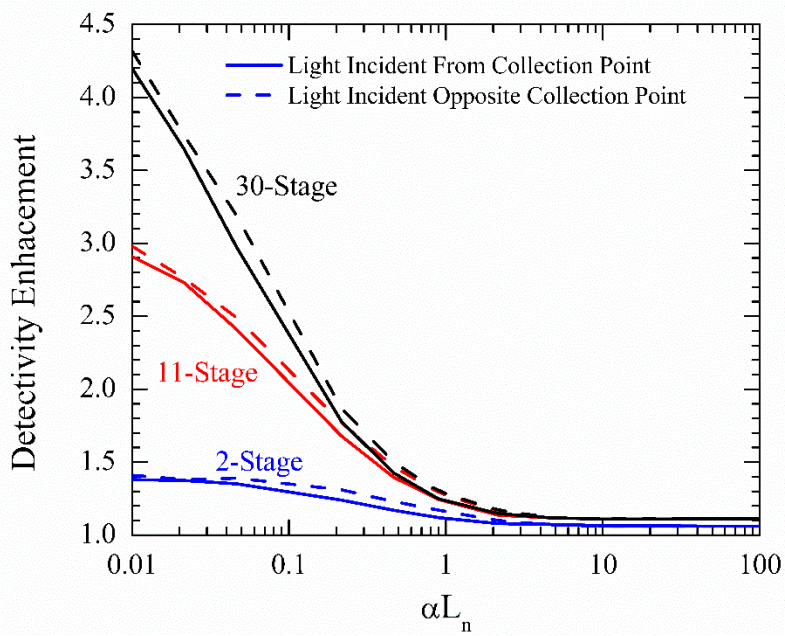

Figure 3.7: Theoretical zero-bias detectivity enhancement for 2-stage, 11-stage, and 30-stage photocurrent-matched multiple-stage interband detectors operating the thermal noise limit. For a given number of stages, the optimal photocurrent-matched detector was found by optimizing the sequence of absorber lengths for maximum *D.**

For the analysis in the thermal-noise limit, we will restrict our analysis to the case where the device is held at zero-bias. At zero-bias, the detectivity enhancement possible from using multiple stages again depends simply on the value of αL_n for the absorber material. This result should suffice as a guide for identifying the operating regimes where this approach is beneficial.

The thermal-noise-limited detectivity for photocurrent-matched detectors is given as:

$$D^* = \frac{\lambda}{hc}\frac{\eta_{ext}}{\sqrt{4g_{th}L_n}}\sqrt{\sum_m \frac{1}{\tanh(d_m/L_n)}}, \tag{3.56}$$

where d_m represents the thickness of the m^{th} absorber. Note that the individual resistance of a given stage scales as $1/\tanh(d_m/L_n)$. Thus, the sum inside the radical in Eq. 3.56 represents a summing of the resistances of each of the stages. This shows that the noise at zero bias reduces to the Johnson noise, given as:

$$i_n^2 = \frac{4k_bT}{R_o}\Delta f, \tag{3.57}$$

where R_o is the total resistance of the detector . To achieve photocurrent-matching, the d_m are chosen so that the number of collected photocarriers is equal in each stage. The optimized photocurrent-matched detectors were found by identifying the optimal sequence of absorber thicknesses for a detector with a given number of stages. The results are shown in Fig. 5 for 2-stage, 11-stage, and 30-stage detectors with αL_n values ranging from 0.01 to 10. Like the equal-absorber case, it is seen that the advantages of using multiple-stages only become significant when $\alpha L_n < 1$. However, it is interesting to note that there is always a sensitivity advantage to be gained from using multiple stages when operating at zero bias. This result is independent of the material parameters. We can simply illustrate this by comparing a single-stage and two-stage detector in the limit where $L_n \rightarrow \infty$, so that: $\eta_{d_m} = 1 - e^{-\alpha d_m}$. For a single-stage device, the optimal absorber thickness that maximizes D^* is $d=1.26/\alpha$ [79]. An optimized two-stage device

will have d_1=0.55/α and d_2=1.32/α. The ultimate zero-bias detectivity for this case is then given by:

$$D^* = (0.339)\frac{\lambda}{hc}\sqrt{\frac{\alpha}{g_{th}}}, \tag{3.58}$$

which is higher than the single-stage value by a factor of 1.06. This zero-bias detectivity enhancement will continue to increase as the number of stages is increased. For a large number of stages, the equation for the detectivity will be similar to Eq. 3.58, but with the numerical prefactor approaching the value of $8^{-1/2}$ as the number of stages is increased. This corresponds to an upper limit improvement of 1.1 times higher D^* than the single-absorber case.

3.4.2 Strong Signal Limit

In this section, we will apply the developed theory to investigate the case of signal-limited detection. This is relevant for certain applications such as optical communication and heterodyne detection, which utilize laser sources. In this limit, it is expected that the best detectors will be those that make the most efficient usage of the incident photons. In the strong-signal limit, the photo-collection current is strong enough that $G_m >> \Gamma_m$ in each stage. Thus, the noise comes directly from the fluctuations associated with signal current flow itself. Since we dealing with a photocurrent-matched design, no compensating injection current across any of the stages is required for realizing current-matching, so the condition of $G_m >> R_m$ holds as well. Here, we shall evaluate the detector sensitivity directly from the signal-to-noise ratios of the different designs. The signal current is given by:

$$i_s = e\eta_{ext}\Phi_o A, \tag{3.59}$$

where η_{ext} is the external quantum efficiency and Φ_o is the incident photon flux For the situation where G_m is much greater than Γ_m and R_m, Eq. 3.14 reduces to:

$$s_o = 2e^2 A \sum_{m-1}^{N_s} \beta_m^2 G_m. \tag{3.60}$$

In the high signal regime, the overall voltage will be applied equally to each stage, so β_m=1/N_s. The overall squared noise current can then be written:

$$i_n^2 = \frac{2e^2 A \eta_{ext} \Phi_o}{N_s} \Delta f, \tag{3.61}$$

where we have utilized the condition: $G_1 = G_2 = \cdots = \eta_{ext}\Phi_o$ for photocurrent-matched detectors. The overall signal to noise ratio (SNR) for an arbitrary number of stages is then given by:

$$SNR = \sqrt{\frac{\eta_{part}\Phi_o A}{2\Delta f}}, \tag{3.62}$$

where we have defined the quantity $\eta_{part} = N_s \eta_{ext}$ as the *particle conversion efficiency*. This metric indicates how efficient the device utilizes the incident photons. We see that Eq. 3.62 reduces to the standard expression for a single-absorber photovoltaic detector in the case of N_s = 1:

$$SNR = \sqrt{\frac{\eta_{ext}\Phi_o A}{2\Delta f}}. \tag{3.63}$$

It can be seen that when the incoming optical signal strong enough that the signal current is much greater than the dark current, there is no longer a design tradeoff between signal and noise. Thus, the design goal is simply to achieve as large a particle conversion efficiency as possible. If the absorber material has good extraction properties, such that η_{ext} can be very high for a single-absorber detector, there is limited room for improving the particle conversion efficiency by utilizing additional stages. However, when the photocarrier extraction properties of the absorber are poor, as indicated by the absorber product αL_n, adding additional stages can greatly enhance

η_{part}. Thus, as with the earlier cases discussed above, the multiple-stage approach will be useful when the product αL_n of the absorber material is relatively low.

3.5 Outlook for Multiple-Stage Detectors Using 6.1 Å Semiconductor Materials

From the above analysis, it can be seen that detectivity improvement is possible using both equal-absorber and photocurrent-matched detectors when $\alpha L_n < 0.5$. Of the two designs, the photocurrent-matched detectors are able to achieve better sensitivities in the αL_n range from 0.1 to 1. Here, we will attempt to put additional perspective on these results for detectors utilizing InAs/GaSb T2SL absorbers. We do this using the empirical data for absorption coefficient and diffusion length. Since much of the existing data was acquired at low temperatures it is difficult to conjecture on the high-temperature performance. We hope this discussion will spur additional interest from community to address some of the open questions.

For InAs/GaSb SL with bandgaps in the MWIR, there is both theoretical and experimental evidence placing the absorption coefficient in the range of 2000-5000 cm^{-1} [102-104]. For LWIR detection, the reported values are smaller, ranging from 1000-2000 cm^{-1} [103,105]. All of these values were acquired in the 77-80 K range, and may be larger at high temperature. There is more scatter in the reported diffusion length values. Several groups have found empirical diffusion lengths by fitting quantum efficiency data. Some results suggest fairly short 80 K diffusion lengths ranging from 0.6 μm [106] to 3.5 μm [105]. However, other sources suggest much larger values (e.g. as high as 20 μm) at this temperature [104,107]. Thus, at 80 K, the value of αL_n for the absorber material will be most likely greater than unity. This would preclude the need for a multiple-stage design for MWIR detection where high-sensitivity is prioritized over response speed. For LWIR detectors it is more difficult to make a concrete judgment. In both spectral ranges, there is a better chance the multiple-stage approach will find

applications for high-temperature detection. As stated earlier, the diffusion lengths are expected to drop at high temperature because of a reduction in the interband carrier lifetime [19-22,108]. However, to our knowledge, there are no systematic studies of the diffusion length dependence on temperature for InAs/GaSb SL material. Such a study must account for both the temperature-dependence of the diffusion coefficient (or equivalently the mobility), as well as the absorber's interband transition time.

The absorber diffusion length will also depend on the doping and the primary generation-recombination mechanism. As discussed in the interoduction, the performance of InAs/GaSb SL detectors is limited by the fairly fast Shockley-Read transition time between the conduction band and valence band states of the absorber material. These defect-assisted generation-recombination effects are strong enough to make it the dominant mechanism, even at higher temperatures where impact ionization and Auger recombination would be dominant in other materials such as MCT. The preferred absorber doping in T2SL detectors depends on the absorber bandgap, but is typically above 10^{16} cm^{-3}. If the source of the defect causing the short lifetime in current InAs/GaSb SL detectors can be identified and eliminated, these detectors may have Auger-limited performance at these doping levels. In this case, a lower absorber doping would be preferred, similar to that used in MCT detectors. In MCT detectors designed for high-temperature operation, the absorber materials are typically doped on the order of 10^{15} cm^{-3} in order to achieve lower rates of impact ionization and Auger recombination (these two processes are the inverse of each other). In these low-doped detectors is also possible to achieve "Auger-suppression" by reverse biasing the detectors and reducing the number of free carriers to very low-levels. However, the low absorber doping means that the carrier collection process will no longer be limited by the minority carriers, but will be ambipolar in nature. Thus, the minority

carrier formalism presented in this paper does not apply to such devices. However, we do conjecture that the multiple-stage architecture should be very useful for improving the collection efficiency of detectors with low-doped absorbers. This is because in the ambipolar regime, the photocarrier extraction process can be much less efficient, since it is limited by the low hole mobility. We are not aware of any studies of the ambipolar diffusion coefficient in 6.1 Å materials, but for MCT it has been established that the difference between the minority electron diffusion length in fairly highly-doped samples and the ambipolar diffusion length in low-doped samples can be fairly large [109]. An optical measurement of diffusion lengths in T2SL, carried out at 77 K, suggested that the hole diffusion length may be two orders of magnitude lower [110] at that temperature. This result suggests the difference between the minority electron and ambipolar diffusion lengths may even be larger in T2SL than in comparable materials.

3.6 Comparison of Single- and Multiple-Stage Photovoltaic Energy-Conversion Devices

When an illuminated photovoltaic device is held at zero current (i.e. open-circuit), a positive voltage is observed. This voltage is the open-circuit voltage, denoted as V_{oc}. When the circuit is connected, and held at a voltage between zero and the V_{oc}, the current flow in the device will be in the opposite direction of the electrostatic potential gradient. In this situation, power is delivered to the external circuit. This is the basis of photovoltaic energy conversion.

The total power for a photovoltaic device is given by:

$$P_{out} = J_{op}V_{op} = J_{sc}V_{oc}FF, \tag{3.64}$$

where J_{op} is the operating current, V_{op} is the operating voltage, J_{sc} is the short-circuit current density, and FF is the fill factor. The operating voltage is the voltage that maximizes P_{out}, and is set by the condition:

$$\left(\frac{\partial P_{out}}{\partial V}\right)_{V=V_{op}} = 0, \tag{3.65}$$

where $P = -JV$. Note that J_{op} is related to V_{op} by the semiconductor device theory developed above. The fill factor is defined as:

$$FF = \frac{J_{op}V_{op}}{J_{sc}V_{oc}}. \tag{3.66}$$

In real devices, the fill factor is typically limited by series resistance effects and shunting currents.

As with multiple-stage detectors, multiple-stage energy-conversion devices will have lower operating currents than single-absorber devices. However, the operating voltages will be higher, so the total power under a given source illumination can be larger. This is because voltage must be applied to each stage in order to provide an injection current that compensates the photo-collection current induced by the light illumination. The open-circuit condition is achieved when the magnitude of the injection and collection currents in each stage are equal. The total voltage will be a sum of the voltage applied to each stage. Using the theory developed in the previous sections of this Chapter, the total V_{oc} for a multiple-stage PV device is given as:

$$\frac{eV_{oc}}{k_bT} = \sum_{m=1}^{N_s} \ln\left(\frac{\Phi_m\eta_m}{\Gamma_m} + 1\right), \tag{3.67}$$

where under strong illumination ($\Phi_m >> g_{th}L_n$) the second term in the ln( ) is negligible. If we assume that the intrinsic carrier concentration of the absorber follows the relationship

$$n_i^2 = N_cN_ve^{-E_g/k_bT}, \tag{3.68}$$

where N_c and N_v are the effective density of states for the conduction band and valence band of the absorber material, then in the strong illumination limit, Eq. 3.67 can be expressed as:

$$\frac{eV_{oc}}{k_bT} = \sum_{m=1}^{N_s} \ln\left(\Phi_m \eta_m \tau_{nr} \frac{p_o}{\sqrt{N_c N_v}} e^{E_g/k_bT}\right), \tag{3.69}$$

where we have also used the well-known relationship $n_o p_o = n_i^2$, which is commonly referred to as the law of mass action. From Eq. 3.69, the relationship between E_g and the V_{oc} (under the assumptions considered in this work) can be expressed as:

$$\frac{eV_{oc}}{k_bT} = N_s \frac{E_g}{k_bT} - \sum_{m=1}^{N_s} \ln\left(\frac{N_c N_v}{\Phi_m \eta_m \tau_{nr} p_o}\right). \tag{3.70}$$

Within the assumptions of this work, the condition $N_c N_v \gg p_o \Phi_m \eta_m \tau_{nr}$ will exist. This implies that each of the terms inside the ( ) in the m ln( ) terms in the sum is greater than unity. Thus, Eq. 3.68 illustrates that while the V_{oc} of a single-absorber (N_s = 1) PV device is bound by $V_{oc} < E_g$, the V_{oc} of an N_s-stage device is bound by $V_{oc} < N_s E_g$. Note that at very high light intensities, many of the assumptions necessary for deriving Eq. 3.70 would not exist (such as the assumption of purely non-radiative thermal generation and recombination). However, the bounding of $V_{oc} < N_s E_g$ would still hold.

The total power delivered to the external circuit is a sum of the power delivered by each individual stage. This is given as:

$$P_{out} = \sum_{m=1}^{N_s} P_m = J_{op} \sum_{m=1}^{N_s} [V_{op,m}], \tag{3.71}$$

where $V_{op,m}$ denotes the operating voltage of the m^{th} stage. The operating current is constant across the device. This means that the difference of the injection and collection currents must be equal in each stage. This requirement also implies that the $V_{op,m}$ values are not independent.

Let us consider how the ultimate efficiency of a PV energy-conversion device can be improved with the use of a multiple-stage design. We will utilize the high illumination

approximation described above, $\Phi_m >> g_{th}L_n$, for each of the m stages. This is the expected condition for most TPV applications. Under this assumption, the photo-collection current is much higher than the thermal collection current. For achieving the best efficiency, a multiple-stage PV energy-conversion device should be designed for photocurrent-matching. With this design choice, the collection currents, given by Eq. 3.33, are equal in each stage. Since the total operating current in each stage must be equal, the injection currents, given by Eqs. 3.34 and 3.35 must also be equal in each stage.

As in the analysis for detectors, we will assume there is no dispersion in the absorption coefficient. This approximation will not hold for most TPV applications, where broadband light is converted. However, in this limit, as with the detector analysis above, it is possible to quantify the performance improvement that is possible from a multiple-stage design simply in terms of the αL_n product of the absorber material. Thus, the analysis below should serve as a useful first approximation.

In terms of the thickness, d_1, and corresponding individual quantum efficiency, $\eta_1(d_1)$, of the absorber in the first stage through which light passes, the operating current is given as:

$$J_{op} = e\left[\eta_1(d_1)\Phi_o - g_{th}L_n \tanh(d_1/L_n)e^{eV_{op,1,}/k_bT}\right], \tag{3.72}$$

where $V_{op,1}$ represents the operating voltage across the first stage. Note we have assumed that S_{eb}=0. The voltages V_m across the $m > 1$ stages can be related to V_1 by using the fact that the injection current components are equal in each stage. This relationship is given as:

$$\tanh(d_1/L)e^{eV_1/k_bT} = \tanh(d_m/L)e^{eV_m/k_bT}, \tag{3.73}$$

for $m > 1$. Solving for V_m gives:

$$\frac{eV_m}{k_bT} = \frac{eV_1}{k_bT} - \ln\left(\frac{\tanh(d_m/L)}{\tanh(d_1/L)}\right). \tag{3.74}$$

For devices designed for photocurrent-matching, the d_m values will increase with increasing m. Thus the voltages across the longer and optically deeper stages will be smaller. Substituting into Eq. 3.71, the power for a multiple-stage PV energy-conversion device is given in terms of $V_{op,1}$ as:

$$P_{out} = e\left[\eta_1(d_1)\Phi_o - g_{th}L_n \tanh(d_1/L_n)e^{\frac{eV_{op,1}}{k_bT}}\right] \times \left[N_s \frac{eV_{op,1}}{k_bT} - \sum_{m=2}^{N_s} \ln\left(\frac{\tanh(d_m/L)}{\tanh(d_1/L)}\right)\right]. \tag{3.75}$$

The operating voltage for the first stage, $V_{op,1}$, is set by Eq. 3.65 with V_1 replacing V as the varied quantity. The value of $V_{op,1}$ is determined by the transcendental equation:

$$\frac{eV_{op,1}}{k_bT} = \frac{eV_{oc,1}}{k_bT} - \ln\left[1 + \frac{eV_{op,1}}{k_bT} - \frac{1}{N_s}\sum_{m=2}^{N_s} \ln\left(\frac{\tanh(d_m/L)}{\tanh(d_1/L)}\right)\right], \tag{3.76}$$

where the voltage contribution from the first stage under open-circuit conditions, $V_{oc,1}$, is given by:

$$\frac{eV_{oc,1}}{k_bT} = \ln\left(\frac{\eta_1\Phi_o}{g_{th}L_n \tanh(d_1/L_n)}\right), \tag{3.77}$$

and the total open-circuit voltage for the multiple-stage photocurrent-matched device is:

$$\frac{eV_{oc}}{k_bT} = N_s\frac{eV_{oc,1}}{k_bT} - \sum_{m=2}^{N_s} \ln\left(\frac{\tanh(d_m/L)}{\tanh(d_1/L)}\right). \tag{3.78}$$

An approximate solution for $V_{op,1}$ can be found through a recursive substitution for $V_{op,1}$ in the ln( ) [111]. This gives:

$$\frac{eV_{op,1}}{k_bT} = \frac{eV_{oc,1}}{k_bT} - \ln\left\{-\frac{1}{N_s}\sum_{m=2}^{N_s}\ln\left(\frac{\tanh(d_m/L)}{\tanh(d_1/L)}\right) + 1 + \frac{eV_{oc,1}}{k_bT} - \ln\left[1 - \frac{qV_{op,1}}{k_bT} - \frac{1}{N_s}\sum_{m=2}^{N_s}\ln\left(\frac{\tanh(d_m/L)}{\tanh(d_1/L)}\right)\right]\right\}, \tag{3.79}$$

where the last ln[ ] term in the braces is negligible. Using Eq. 3.77 and Eq. 3.78, $V_{op,1}$ can be written in terms of the total V_{oc}. This is given by:

$$\frac{eV_{op,1}}{k_bT} = \frac{eV_{oc,1}}{k_bT} - \ln\left(1 + \frac{1}{N_s}\frac{eV_{oc}}{k_bT}\right), \tag{3.80}$$

Note that for the case of N_s=1, the total operating voltage is given by:

$$\frac{eV_{op,1}}{k_bT} = \frac{eV_{oc,1}}{k_bT} - \ln\left(1 + \frac{eV_{oc}}{k_bT}\right). \tag{3.81}$$

Substituting Eq. 3.79 into Eq. 3.75, we can now cast the total output power in terms of the design, material, and illumination parameters:

$$P_{out} = e\left[\eta_1(d_1)\Phi_o - g_{th}L_n\tanh(d_1/L_n)\frac{e^{\frac{eV_{oc,1}}{k_bT}}}{1 + \frac{1}{N_s}\frac{eV_{oc}}{k_bT}}\right] \times \left[N_s\frac{eV_{oc,1}}{k_bT} - \ln\left(1 + \frac{1}{N_s}\frac{eV_{oc}}{k_bT}\right) - \sum_{m=2}^{N_s}\ln\left(\frac{\tanh(d_m/L)}{\tanh(d_1/L)}\right)\right]. \tag{3.82}$$

The multiple-stage design will be most useful when a low value of αL_n limits the possible quantum efficiency absorber material. When this is the case, the portion of the photon flux that cannot be efficiently converted to current in a single-stage can instead be used to drive a voltage in the later stages. However, as seen, with the photocurrent-matched design, gains in efficiency are still possible, even when the absorber material is fairly good (αL_n > 10). This is because in

PV energy-conversion devices, as in photodetectors operating in the thermal noise limit, there is a tradeoff in choosing the thickness of the absorber. As the absorber is made thicker, more light is absorbed, increasing the short-circuit current. However, the open-circuit voltage will be higher as the absorber thickness, d, is made thicker, since the injection current will increase as $L_n \tanh(d/L_n)$.

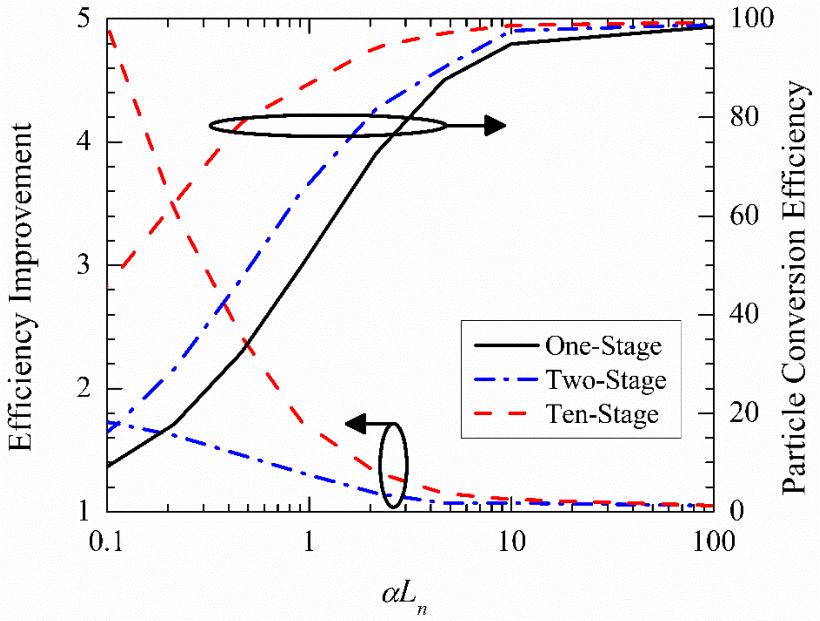

Figure 3.8: Theoretical efficiency improvement for 2-stage and 10-stage photocurrent-matched multiple-stage photovoltaic energy-conversion devices as a function of the product of the absorption coefficient and diffusion length of the absorber material. The ratio of the photon flux to the thermal flux ($\Phi_o/g_{th}L_n$) was set equal to $1x10^6$. Also shown are the particle conversion efficiencies for optimized 1-stage, 2-stage, and 10-stage devices.

The possible efficiency improvement that can be achieved with the use of 2-stage and 10-stage photocurrent-matched devices is shown in Fig. 3.8 for a range of αL_n values from 0.1 to 100. In this analysis, the optimal absorber thicknesses for each design were found by finding the values that maximized P_{out}, as given in Eq. 3.82. In the analysis, the ratio of the photon flux to the thermal flux, defined as:

$$\xi = \frac{\Phi_o}{g_{th}L_n}, \tag{3.83}$$

was taken to be equal to 1.0×10^6. Also shown in Fig. 3.8 are the particle conversion efficiencies for optimized 1-stage, 2-stage, and 10-stage devices.

As predicted, the multiple-stage devices are most effective when αL_n is fairly low, and better efficiency improvement is possible when more photocurrent-matched stages are used. For instance, when, $\alpha L_n = 0.1$, an efficiency improvement of 73% is possible by using a 2-stage device and an improvement of 395% is possible by using a 10-stage device. Even for high values of αL_n, efficiency improvement is possible due to the fact that optimized multiple-stage detectors use incident photons more efficiently than optimized single-stage devices. This can be seen from the particle conversion efficiency curves. For $\alpha L_n = 10$, the particle conversion efficiencies for optimized 1-stage, 2-stage, and 10-stage devices are 94.9%, 97.6%, and 98.7%. As a result, an optimized 2-stage device is 7% more efficient than an optimized 1-stage device, while an optimized 10-stage device is 10% more efficient.

Chapter 4 : Interband Cascade Structures for Infrared Radiation Energy Conversion

4.1 Overview

This chapter presents the design and experimental characterization of interband cascade PV devices that were designed for the conversion of infrared radiation. The chapter is split into two parts. The first part reviews the characterization of devices from wafer EB3337. These devices had cutoff wavelengths of ~5 μm at room temperature and were designed with identical cascade stages. The absorbers in these stages were composed of conventional InAs/GaSb SLs. The second part of the chapter details work done on devices with wider-bandgap absorbers. The devices presented in this section were fabricated from wafer EB3911, which had three cascade stages, and EB3917, which had two cascade stages.

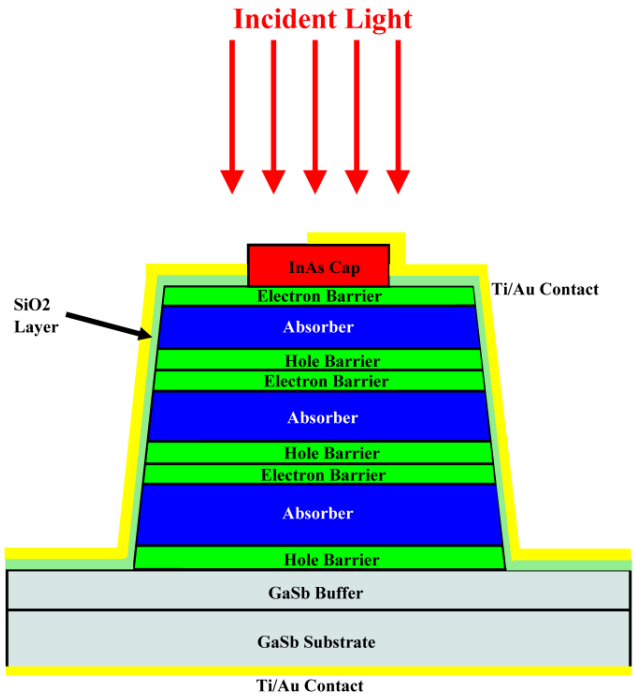

Figure 4.1: Schematic representation of device processed from wafer EB3911.

Each of the three EB3--- series of samples were grown using molecular beam epitaxy at Sandia National Laboratories. Each was grown on a (100) p-type GaSb substrate. The

processing of these wafers into devices was done at the University of Oklahoma. The processing steps for all the devices presented below were similar. A schematic of a processed device from wafer EB3911 can be seen in Fig. 4.1. For all the devices presented, the processing was carried out using standard contact UV lithography followed by wet-chemical etching. After the etching was completed, a dielectric layer was deposited for passivation using an AJA sputtering system. Most of the devices were passivated with SiO_2. Other devices were passivated with silicon oxynitride (combination of SiO_2 and Si_3N_4). The metal contacts, consisting of 30 nm Ti / 180 nm Au, were deposited with thermal evaporation. Further details specific to each set of devices are given below.

4.2 Narrow-Bandgap Photovoltaic Devices

4.2.1 EB3337 Structure Details

The absorber in the wafer EB3337 composed of a 33-period InAs/GaSb (7/9 monolayers) type-II SL. The GaSb layers in the SL absorber were *p*-doped with a targeted dopant concentration of $3.0x10^{17}$ cm^{-3}. The total thickness of each absorber was ~0.16 μm. The absorbers for each stage were made identical. The electron barrier in this structure was composed of alternating layers of GaSb and AlSb with layer thicknesses (in Angstroms) of **16**/53/**16**/75, where the normal and bold numbers refer to the GaSb and AlSb layers, respectively. The hole barrier was composed of InAs, AlSb, and $Al_{0.8}In_{0.2}Sb$, with a digitally graded layer thickness (in Angstroms) sequence given by **20**/81/**20**/66/***21***/55/**22**/47.5/***23***/42/**24**/37.5/***25***/34/**26**/31/**32**, where normal, bold, and bold italic represent InAs, AlSb, and $Al_{0.8}In_{0.2}Sb$ layers respectively. The GaSb layers in the electron barrier were *p*-doped with the same concentration as those in the absorber, while the AlSb layers were left undoped. All the layers in the hole barrier were left undoped. The band diagram of

this structure under a forward bias is shown in Fig. 4.2. The figure shows the layer structure near the interface of the electron and hole barriers. The bottom conduction miniband and highest valence miniband of the SL absorber are indicated. The ground state energy levels and wavefunctions for the QWs that compose the barrier regions are shown. The electron and hole levels were calculated using the *k*•*p* envelope function theory [112]. The potential of the free carriers was included using the Hartree approximation [113]. This yielded self-consistent Schrödinger-Poisson solutions of the charge and potential distribution. As seen, the voltage is primarily applied to the electron and hole barriers, and a flat-band condition is maintained in the SL absorber, even for a device under bias.

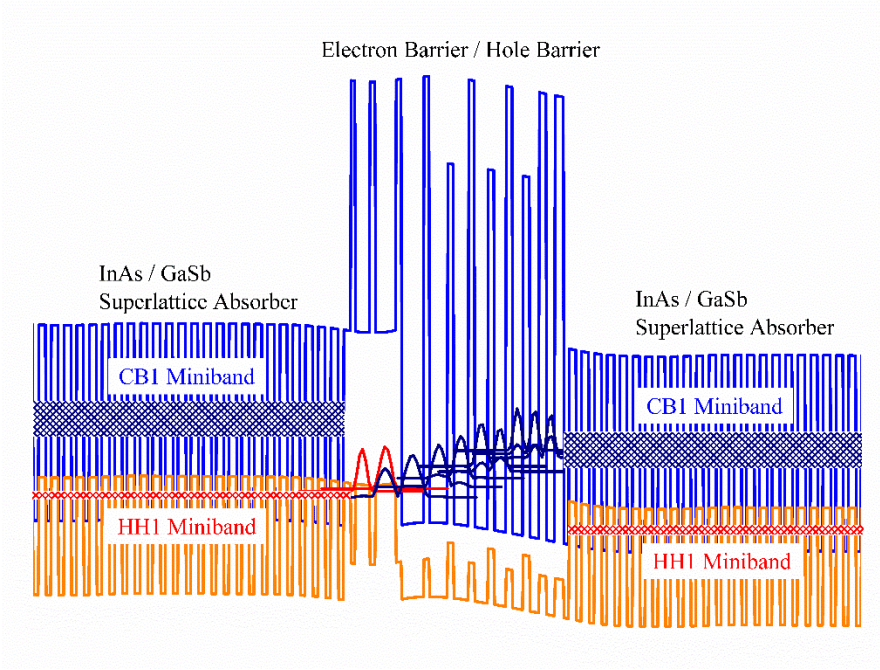

Figure 4.2: Calculated band diagram of EB3337 under forward bias at 300 K in the region near the interface of electron and hole barrier regions.

The devices were processed into circular mesa devices with mesa diameters ranging from 100-400 μm. For characterization, the devices were mounted onto ceramic chip carriers and wire-bonded. In order to study the temperature-dependence of the performance metrics, the

devices were mounted in a LN_2-cooled cryostat. A Lakeshore 331 control unit was used to vary the temperature of the device. A calibrated blackbody emitter was used as a thermal radiation source. The external quantum efficiency (EQE) and current-voltage characteristic curves were measured over a range of device temperatures from 80 to 340 K. A Nicolet 8700 Fourier Transform Infrared Spectrometer (FTIR) was used to measure the relative spectral response. The calibrated EQE spectrum was found by measuring the device's photocurrent, while it was illuminated by the blackbody source. For the EQE measurements, the blackbody source was heated to 1,200 K, and placed 30 cm away from the device. For the low-temperature dark current measurements, the device was encased in a cold shield in order to isolate it from the ~300 K background radiation.

4.2.2 Photocurrent and Open-Circuit Voltage

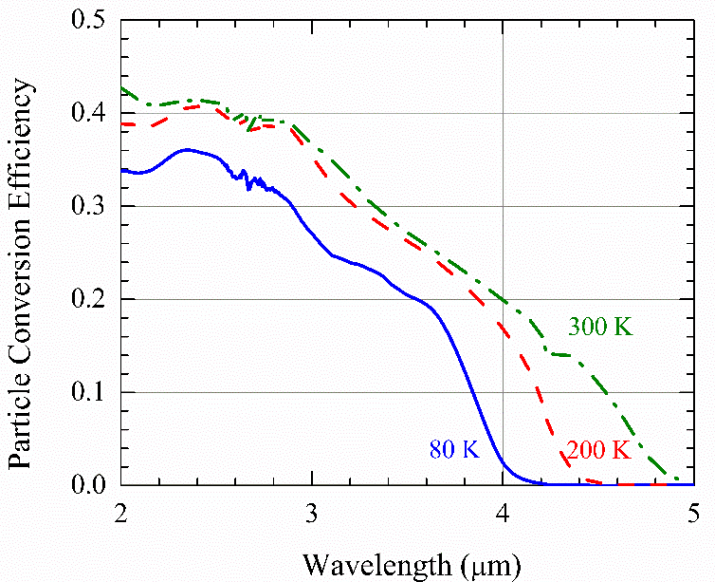

Figure 4.3: Particle conversion efficiency of device from wafer EB3337 at different temperatures.

In this section, we present detailed results from the device that achieved the highest open-circuit voltage (V_{oc}) at 80 K. The diameter of this device was 400 μm and it was passivated with silicon oxynitride. Other devices fabricated from this wafer (both passivated with SiO_2 and

silicon oxynitride) showed comparable performance. The particle conversion efficiency spectra at temperatures of 80, 200, and 300 K for a device processed from this sample are shown in Fig. 4.3. Recall that the particle conversion efficiency for a device is defined as the external quantum efficiency times the number of stages. This data was acquired at zero-bias. The device had a 10% cutoff wavelengths of 4.0 μm at 80 K and 4.8 μm at 300 K. From these values, the SL absorber bandgap (E_g) is estimated to be 0.31 eV at 80 K and 0.26 eV at 300 K. As seen, the signal becomes stronger as the temperature is increased, even up to room temperature. This observation suggests efficient photocarrier collection because the EQE is not sensitive to the decrease in minority carrier diffusion length at higher temperatures.

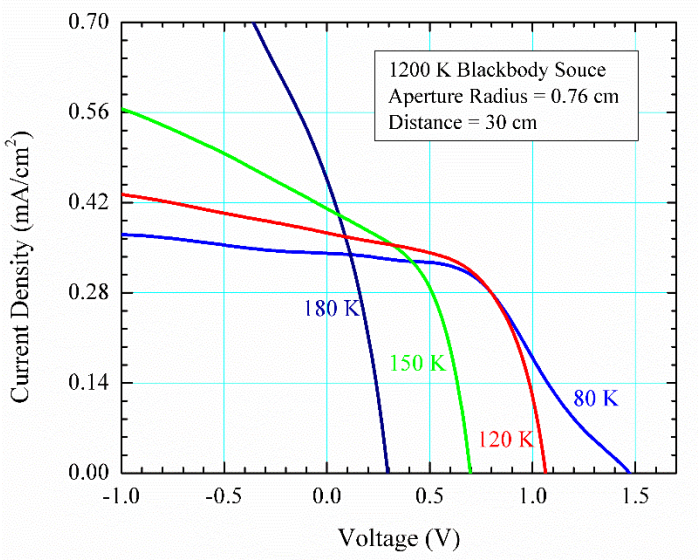

Figure 4.4: Current density-voltage characteristics at different device temperatures for a device illuminated by a 1200 K blackbody source. The aperture radius of the source was 0.76 cm and it was held at a distance of 30 cm from the device.

The current measured under illumination at different device temperatures is displayed in Fig. 4.4. This data was taken for both forward- and reverse-bias voltages. For this particular measurement, the blackbody source temperature was 1,200 K, the aperture radius of the blackbody emitter was 0.76 cm, and the distance between the emitter and the device was 30 cm.

The observed increase in short-circuit current density (J_{sc}) with device temperature is caused by the bandgap narrowing of the absorber. At all temperatures, an increase in current is observed when the device is reverse-biased. For the data taken at 150 and 180 K this trend is primarily due to the high dark current at these temperatures. However, for this light intensity, the dark current (measured with radiation shielding) for the device at 80 K was over two orders of magnitude lower than the illumination current ($<10^{-4}$ mA/cm^2 at -2.0 V). For a device temperature of 120 K, this difference between the dark and light current was over one order of magnitude. Thus, for these temperatures, we are observing a voltage-dependent photocurrent. In ideal PV devices, the photocurrent should be insensitive to an increase in reverse bias. It is possible that carriers generated in the absorber do not recombine at the interface of the electron barrier and hole barrier. Instead, they may undergo intraband tunneling across their namesake barrier. This is similar to the "photoconductive gain" effect observed in quantum well infrared photodetectors [27]. This "leaky barrier" effect is detrimental in forward bias. Electrons tunneling across the barrier relax via non-radiative processes to an adjacent absorber that is lower in the energy cascade. Theoretical calculations indicate that the electron barrier should be sufficiently thick to suppress direct intraband tunneling [14]. However, the tunneling process may be assisted by defect states within the bandgaps of GaSb or AlSb.

Figure 4.5(a) shows the V_{oc} as a function of device temperature. This data was acquired under the same illumination settings as the data presented in Fig. 4.4. The cascade design enabled the device to maintain a V_{oc} above the individual absorber bandgap up to 180 K even under a weak light illumination. However, this value falls off to just a few meV at higher temperature as the dark current becomes more dominant. Under a more powerful laser source, it

was actually found that devices from this wafer were able to achieve open-circuit voltages above the individual bandgap at room temperature [114].

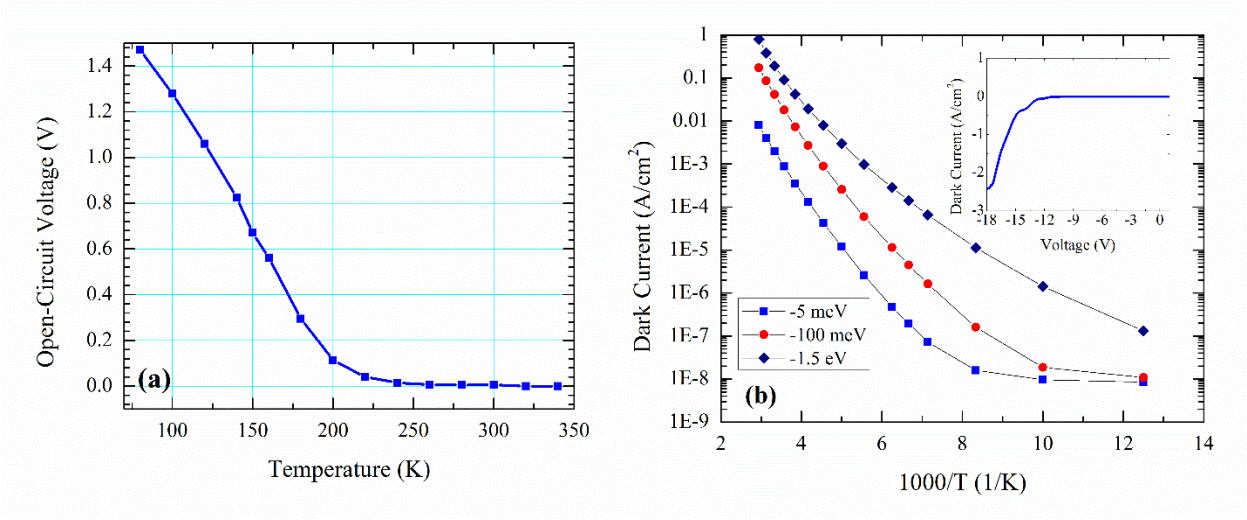

Figure 4.5: Device temperature dependence of (a) open-circuit voltage and (b) dark current density of an IC PV device. The dark current was measured at reverse-bias voltages of -5 mV, -100 mV, and -1.5 V under radiation shielding.

An Arrhenius plot illustrating the temperature-dependence of the dark current density for bias voltages of -5.0 mV, -50 mV, and -1.5 V is shown in Fig. 4.5(b). The inset of Fig. 4.5(b) shows the long-range dark current characteristics at a device temperature of 80 K. This data shows that diode-like rectification can be achieved in IC PV devices over a large voltage range. However, the dark current characteristics indicate that there is some amount of non-ideal leakage current.

In ideally operating equal-absorber-length IC PV devices, the application of reverse bias should lead to a depletion of minority carriers in the absorber. At high reverse bias, the current should saturate to a value determined by the thermal generation due to Shockley-Read-Hall processes or impact ionization. In our data, there is no clear saturation of the current in reverse bias. This can also be seen by comparing the magnitude and the slope of the Arrhenius plots of the dark currents. For most temperatures, an order of magnitude increase in the dark current is

observed as the bias voltage is increased from -50 mV to -1.5 V. The slope of the Arrehenius curves for the data at large reverse bias is also less steep. This means that the current that flows at a given voltage is less temperature sensitive. This suggests that at higher reverse bias voltages, a larger percentage of the transport is occurring through non-ideal channels, since the non-ideal current tends to be less temperature-sensitive than the fundamental generation current.

One possibility for the additional leakage current is that the mesa edge is not sufficiently passivated and there are current-carrying surface states present. Another possibility is the defect-assisted carrier tunneling across the electron barrier. This is the same mechanism earlier identified as a possible cause of the bias-dependent photocurrent. This process is analogous to the trap-assisted tunneling current often observed in *p-i-n* junctions under reverse bias [7].

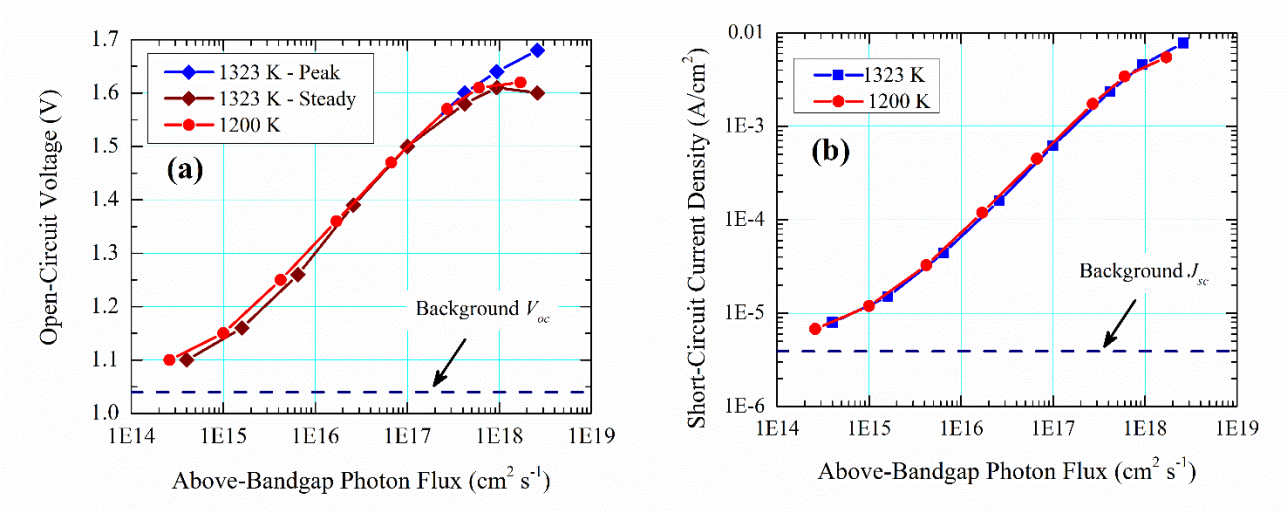

Figure 4.6: (a) Open-Circuit voltage and (b) short-circuit current density for an IC PV device at 80 K for various above-bandgap photon fluxes. The incident photons were generated from a blackbody source at temperatures of 1200 K and 1323 K. The photon flux was varied by changing the aperture radius of the blackbody source. The above-bandgap fluxes were computed using Planck's radiation law.

The relationship between the V_{oc} and short-circuit current density (J_{sc}) of the device and the incident above-bandgap photon flux is shown in Figs. 4.6(a) and 4.6(b). This data was acquired for a device temperature of 80 K. For a given blackbody temperature, the photon flux

was changed by altering the aperture size of the emitter. For each of these measurements, the distance between the blackbody source and the device was 10 cm. The incident photon flux was calculated by considering the radiation transferred from the blackbody source, which emits light out of a circular aperture, to the device at a given distance away from the source. The photon flux from the source to the device is given by:

$$J_\gamma = \left(\frac{r_a}{d}\right)^2 \frac{2\pi}{h^3 c^2}\left[\int_0^\infty dE\ \frac{E^2}{e^{E/k_b T_s} - 1} - \int_0^\infty dE\ \frac{E^2}{e^{E/k_b T_{amb}} - 1}\right]. \tag{4.1}$$

As seen, this is a modified version of Eq. 1.1, where a prefactor of $(r_a/d)^2$ is put in front of the integral to account for the fact that the setup can be treated as a point source emitting radiation to an object in the far-field [115]. The dashed lines in Figs. 4.6(a) and 4.6(b) show the "background" values for V_{oc} and J_{sc}. These are the values measured when the radiation from the blackbody source was blocked. These values are nonzero because the unshielded device (at 78 K) was still exposed to the radiation from the ~300 K ambient surroundings. It was noticed that there was an increase in device temperature when larger apertures were used, due to heating from the blackbody source. Thus, there are two values of V_{oc} quoted for the higher blackbody temperature of 1,323 K. The "Peak" values were measured immediately after the device was illuminated. The device temperature in this case was the lowest that could be achieved with LN_2. The "Steady" values were measured when the device reached a stable temperature, after the heating from the blackbody source. The large deviation between the measurements before and after heating for an aperture radius of 1.2 cm indicates that there was a significant rise in the device temperature. The scaling of J_{sc} with incident photon flux was approximately linear, and was not strongly affected by the device heating. The highest V_{oc} value we observed was 1.68 V. This value was found for the largest aperture size, and was measured before device heating was

observed. The highest stable-temperature V_{oc} was 1.63 V. With the bandgap estimated from the spectral EQE, we find these V_{oc} values are 77% and 75% of the effective bandgap of $N_{stage}E_g$, respectively, where N_{stage} is the number of cascade stages.

4.2.3 Power Conversion Efficiency and Relevant Physical Processes

There are a diverse number of TPV approaches and applications. Consequently, there has not been a standardization of how to characterize the efficiency of a TPV device. In this work, the total efficiency we give, η_{tot}, is a measure of how well the device was able to convert the radiation from the blackbody emitter used to characterize the device. In the following analysis, we put this value into context by breaking it into a product of individual efficiencies. Each of the individual efficiencies characterizes the power loss from a certain physical mechanism in the energy-conversion process. This analysis enables us to gain insight on how these relevant processes affect the device performance. This approach is similar to that used in Ref. 4. The product of the individual efficiencies is given by:

$$\eta_{tot} = \eta_{spec}\eta_{win}\eta_{strans}\eta_{therm}\eta_{abs}\eta_{coll}\eta_{oc}FF, \tag{4.2}$$

where η_{spec} is the spectral efficiency, η_{win} is the window transmission efficiency, η_{strans} is the surface transmission efficiency, η_{therm} is the thermalization efficiency, η_{abs} is the absorption efficiency of TPV cell, η_{coll} is the collection efficiency, η_{oc} is the voltage efficiency, and FF is the fill factor. The spectral efficiency is the fraction of transmitted power above the absorber bandgap. The window transmission efficiency is the percentage of incident above-bandgap power that is transmitted by the cryostat window. The surface transmission efficiency is the percentage of above-bandgap power that passes through the window and is subsequently transmitted by the air-semiconductor interface. It indicates the amount of power that is lost to reflection and contact absorption. The thermalization efficiency describes the amount of

transmitted above-bandgap power that can be recovered after carrier thermalization. The absorption efficiency, and collection efficiency, characterize the percentage of transmitted above-bandgap light that is absorbed by the cell and successfully collected. The voltage efficiency is given by: $\eta_{oc}=V_{oc}/(N_{stage}E_g)$.

In this analysis, the power loss from below bandgap photons was considered first. This was done in order to make it easier to estimate the efficiency if the losses from the window or surface transmission were improved or eliminated. The transmission at the window is a loss introduced by our experimental setup, rather than a loss that is intrinsic to the device. In a real situation this loss may not be present. The reflection loss at the surface can be improved by using anti-reflection coating.

The total power conversion efficiency is obtained from the measured *J-V* curves and the calculated total incident power intensity from the blackbody source. The incident light power per unit area from the blackbody emitter is given by the equation:

$$I_{inc} = \left(\frac{r_a}{d_{sd}}\right)^2 \sigma(T_{bb}^4 - T_{amb}^4), \tag{4.3}$$

the distance between the blackbody emitter and the device, σ is the Stefan-Boltzmann constant, T_{bb} is the blackbody emitter temperature, and T_{amb} is the ambient temperature (taken to be 300 K).

A summary of the efficiency analysis done at 80 K for two different blackbody configurations is shown in Table 4.1. For the first case, we set T_{bb} = 1,200 K and d_{sd} = 30 cm, and for the second case we set T_{bb} = 1,323 K and d_{sd} = 9.5 cm. The *J-V* curve corresponding to the first configuration is shown in Fig. 4.5 (80 K curve). The estimated particle (electron or photon) flux loss and power loss from the different physical mechanisms is given in Table 4.1. The individual efficiencies for the two configurations are also given. Note that we carried out

this analysis under the assumption that the absorption of seven photons (one per stage) was required in order to deliver an electron to the external circuit. This neglects any "photoconductive gain" effects.

The efficiency η_{spec} was calculated from Planck's blackbody radiation law, assuming a bandgap of 0.31 eV at 80 K. The transmission loss at the cryostat window was evaluated by measuring the spectral transmittance of the CaF_2 window. The resultant efficiency η_{win} was found by integrating the product of this measured spectrum and the blackbody spectrum across above-bandgap energies. Because anti-reflection coating was not applied, the light reflection at the semiconductor-air interface was a major source of power loss. To determine this loss, we estimated the refractive index contrast between air and the semiconductor gives an interface reflectance of $R \approx 30\%$. It was not possible to break down η_{abs} and η_{coll} into constituent efficiencies. This was because the spectral-dependence of the absorption coefficient for SL absorber material is not accurately known, and there is evidence that the carrier collection is not perfect. Instead, we simply quote their product as a single efficiency.

	T_{bb} = 1200 K, r_a = 0.76 cm, d_{sd} = 30 cm			T_{bb} = 1323 K, r_a = 0.76 cm, d_{sd} = 9.5 cm		
Loss Mechanism	**Particle Loss (cm^{-2} s^{-1})**	**Power Loss (mW cm^{-2})**	**Efficiency**	**Particle Loss (cm^{-2} s^{-1})**	**Power Loss (mW cm^{-2})**	**Efficiency**
Below Bandgap Transmission	1.06×10^{17}	2.94	η_{spec} = 61.0%	12.9×10^{17}	36.7	η_{spec} = 67.0%
Window Transmission	1.1×10^{16}	0.71	η_{win} = 84.6%	1.6×10^{17}	10.5	η_{win} = 85.8%
Reflection	1.5×10^{16}	1.16	η_{strans} 70.0	2.3×10^{17}	19.2	η_{strans} = 70.0
Carrier Relaxation	0	0.99	η_{therm} = 63.6%	0	17.5	η_{therm} = 60.8%
Incomplete Absorption/Collection	2.0×10^{16}	0.99	$\eta_{abs}\eta_{coll}$ = 42.8%	2.7×10^{17}	13.6	$\eta_{abs}\eta_{coll}$ = 50.0%
Voltage Losses	0	0.24	η_{oc} = 67.7%	0	3.4	η_{oc} = 75.1%
Non-unity fill factor	2.5×10^{15}	0.28	FF = 44.6%	4.6×10^{16}	5.5	FF = 46.3%
Total	1.5×10^{17}	7.3	η_{tot} = 3.0%	2.0×10^{18}	106	η_{tot} = 4.3%

Table 4.1: Individual efficiency analysis of a blackbody-illuminated IC PV device for different blackbody settings at 80 K.

At 80 K, from the measured *J-V* curves, the value of η_{tot} for the device is 3.0% when illuminated by the blackbody emitter with settings T_{bb} = 1,200 K and d_{sd} = 30 cm, and 4.3% for

the case of T_{bb} = 1,323 K and d_{sd} = 9.5 cm. For the second configuration, the values of $\eta_{abs}\eta_{coll,}$ η_{oc}, and *FF* are all higher, and thus, all contribute to the higher overall efficiency. The larger η_{oc} for the second case is an expected result, due to the higher incident photon flux. The higher values for $\eta_{abs}\eta_{coll}$ and *FF* for T_{bb} = 1,323 K are more challenging to explain. Additional analysis (not documented in Table 4.1) showed that changes in r_a and d_{sd} gave the same values for $\eta_{abs}\eta_{coll}$ and *FF* (to two significant digits) for measurements taken at the same value of T_{bb}, but different values of η_{oc}. In these measurements, as expected, higher values of η_{oc} were observed when there were more incident photons. This comparison of individual efficiencies shows that the higher values of $\eta_{abs}\eta_{coll}$ and *FF* for T_{bb} =1,323 K are partially due to the spectral shape change for different T_{bb}, and are not a merely a result of different incident photon fluxes. Overall, the *FF* for both cases (45% and 46%) is fairly low compared to both the theoretical limit (>80%) and typical value (~70%) of TPV cells [4]. This suggests that there is significant room for improvement. This will require further exploration of the transport through parallel paths such as etched surfaces. A study of the current in these transport paths is presented below for the next set of PV devices.

The low value of $\eta_{abs}\eta_{coll}$ for both cases (42.8% and 50.0%) is mainly due to the incomplete absorption of photons. The total thickness of the seven absorbers was only about 1.1 μm. Although the carrier collection might not be perfect, the estimated η_{coll} is no lower than 80% for both cases. This assertion is based on the voltage-dependent photocurrent data presented earlier. The value of η_{coll} can be further enhanced with improved individual stage design to ensure better carrier collection or to suppress the photoconductive gain effects. Increasing the value of η_{abs} can be simply realized by increasing the absorber lengths or the number of stages. In addition, realizing the very high particle conversion efficiencies values predicted for IC PV

devices will require using absorbers of different lengths to ensure an equal amount of photon absorption in each stage. This sort of design is explored in the next section.

4.3 Wider-Bandgap Photovoltaic Devices

4.3.1 Structure Details of EB3911 and EB3917

The basic structure design for wafers EB3911 and EB3917 was similar to that of EB3337 and previous interband cascade PV devices discussed in Refs 12-14. Each stage had a SL absorber sandwiched between an electron barrier and hole barrier. The hole barrier was composed of seven digitally graded InAs/AlSb QWs. The electron barriers in these structures were composed of three GaSb/AlSb QWs, making it slightly thicker than EB3337, which had only a two-well electron barrier. The layer thickness sequence for the electron barriers in EB3911 and EB3917 was **15**/39/**15**/53/**15**/75, where the normal and bold numbers refer to the GaSb and AlSb layers, respectively. Like EB3337, the GaSb layers in both the absorber and electron barrier were doped p-type. However, the doping concentration used was a slightly lower value of 3.5×10^{16} cm^{-3}.

One difference with the prior work is that we utilize a SL period consisting of an InAs-GaSb-$Al_{0.8}In_{0.2}Sb$-GaSb layering sequence, rather than the standard InAs/GaSb SL. The thin (~7 Å) layer of $Al_{0.8}In_{0.2}Sb$ enables a wider absorber bandgap. The choice of $Al_{0.8}In_{0.2}Sb$ (lattice constant of 6.204 Å) also provides compensation to the tensile strain between the InAs (lattice constant of 6.058 Å) layers and the GaSb (lattice constant of 6.096 Å) substrate.

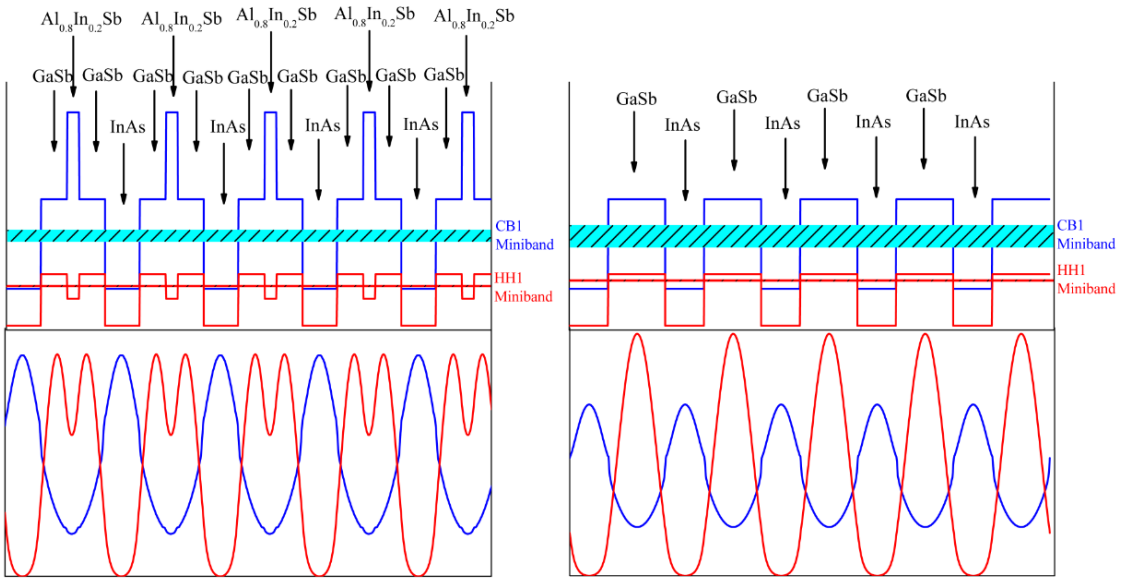

Figure 4.7: Band diagram and first electron and heavy hole minibands of both the modified type-II superlattice with $Al_{0.8}In_{0.2}Sb$ layer insertion and a normal Al-free SL with the same InAs and GaSb thickness in a single-period. On the lower part, the squared wavefunctions for the ground state of the conduction miniband (blue) and heavy hole minibands (red) are shown for both cases.

The effect of inserting this layer into the SL is illustrated in Fig 4.7. The band diagrams in the figure compare the modified SL design with that of the more conventional Al-free InAs/GaSb type-II SL. The ground state minibands for the conduction and heavy hole band are shown. The difference between the band-edges of these minibands forms the effective bulk bandgap of the SL. Below the band diagrams, the squared wavefunctions for the ground state of the conduction miniband (blue) and heavy hole minibands are shown for both cases. Note that the miniband dispersions and wavefunctions were calculated by assuming periodic boundary conditions (i.e. the "infinite superlattice" approximation). It is seen that by splitting the GaSb layer and adding a layer of $Al_{0.8}In_{0.2}Sb$, the band-edge of the lowest conduction miniband is pushed up in energy, and the edge of the highest heavy hole miniband is pushed down. This creates a larger effective bandgap for the SL, enabling the realization of interband cascade PV devices with bandgaps closer to the range of conventional TPV technology. In addition, the

enhanced spatial overlap between the electron and heavy hole wavefunctions should lead to stronger light absorption. This SL design is similar to an M-structure SL, which uses binary AlSb to achieve wider-bandgap [116].

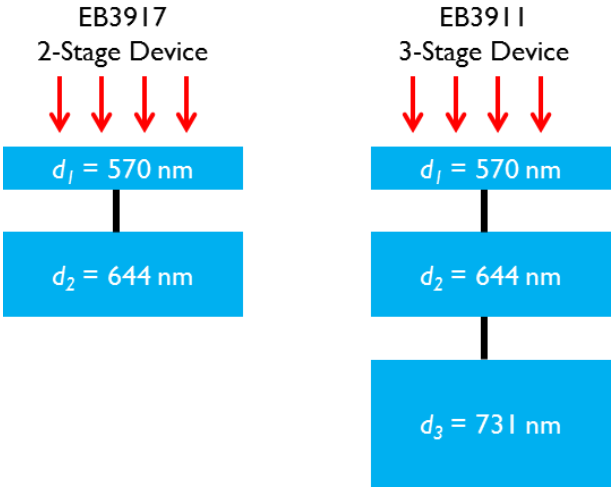

Figure 4.8: Structure designs for wafers EB3911 and EB3917. The absorber thicknesses were varied in order to achieve better photocurrent-matching between the stages.

Another novel feature of these two structures in comparison to EB3337 and previous IC PV devices is that the absorber thicknesses were varied across the structure in order to achieve a rough photocurrent-matching between the stages. The variation of the absorber thicknesses in the two structures is shown in Fig 4.8. The first two absorbers in both structures consisted of SLs with 100 and 113 periods respectively. This corresponds to absorber thicknesses of 570 nm and 644 nm. The third absorber SL in the wafer EB3911 had 130 periods, corresponding to a thickness of 741 nm.

4.3.2 Quantum Efficiency Calibration

The quantum efficiency calibration technique used for EB3911 and EB3917 was slightly different than the method described above for EB3337. One change in the procedure was the choice to use lower blackbody source temperatures of 500 K – 800 K. The procedure was modified due to the limited spectral range of the KBr beamsplitter used in the FTIR. With this

beamsplitter material, the relative spectral response obtained from the FTIR is not accurate for photon energies above 0.8 eV. In addition, rather than calibrating the spectra with separate blackbody measurements at each temperature, the calibrated quantum efficiency obtained for a device at 78 K was used as a reference spectrum to calibrate the quantum efficiency of that device at higher temperatures. This was done by finding the calibration factor, R_{cal}, which related the absolute spectral responsivity of the detector, $R(E)$, and relative responsivity R_{rel}(E) measured by the FTIR. This relationship is given as:

$$R(E) = R_{cal}R_{rel}(E). \tag{4.4}$$

Note that *R(E)* is defined as the ratio of the photocurrent that flows in the device and the optical power incident on the device. The responsivity is related to the η_{ext} by:

$$\eta_{ext}(E) = \frac{E}{e}R(E). \tag{4.5}$$

To find R_{cal} for a certain device, a lock-in amplifier was used to measure the photocurrent produced in the device at 78 K, while it was illuminated by the chopped blackbody source. In order to estimate the precision of R_{cal}, the photocurrent was measured for a variety of blackbody source apertures. In addition, the calibration was carried for different source temperatures of 500 K and 800 K. Comparing the results of each of these separate measurements, the uncertainty in R_{cal} was found to be about ~6% or less.

It should be noted that at high temperatures, when the device's resistance, R_{dev}, was comparable with the input impedance, R_{in}, of the pre-amplifier used, the following correction was applied to obtain the photocurrent:

$$I_{ph} = I_{pp}(1 + R_{in}/R_{dev}), \tag{4.6}$$

where I_{pp} is the measured peak-to-peak current and I_{ph} is the actual photocurrent. This correction is need because at high temperatures the device's resistance is reduced and is comparable with

the input impedance of the amplifier. Thus, the total current is split between the two paths. The value of R_{dev} was obtained by differentiating the measured current-voltage characteristics. For high temperature measurements, the correction factor in the ( ) in Eq. 4.5 can be fairly large. This would plausibly introduce additional uncertainty into the measurement due to the uncertainty in both R_{dev} and R_{in}. However, the good agreement between the direct photocurrent measurements and the photocurrent obtained by integrating the calibrated responsivity spectra seems to confirm that the method is sound. This correction had to be applied to convert both the signal from the FTIR and the signal from the device when illuminated by the blackbody.

4.3.3 Device Photovoltaic Properties

The photomask used to process the material from EB3911 and EB3917 into devices was different than the one used for EB3337. This one was designed to create square mesa devices with dimensions ranging from 0.2x0.2 mm^2 to 1.0x1.0 mm^2. The zero-bias EQE spectra for devices with dimensions of 0.4x0.4 mm^2 from EB3917 and EB3911 are shown in Fig. 4.9. The devices from both wafers have a 10% cutoff wavelength of ~3.0 μm, corresponding to a room temperature bandgap of about ~0.41 eV. As seen, the current-mismatching between stages causes the 2-stage device to achieve a higher EQE. This mismatch is fairly small for photon energies near the bandgap. The larger current mismatch at higher photon energies is likely because of the stronger absorption at higher energies.

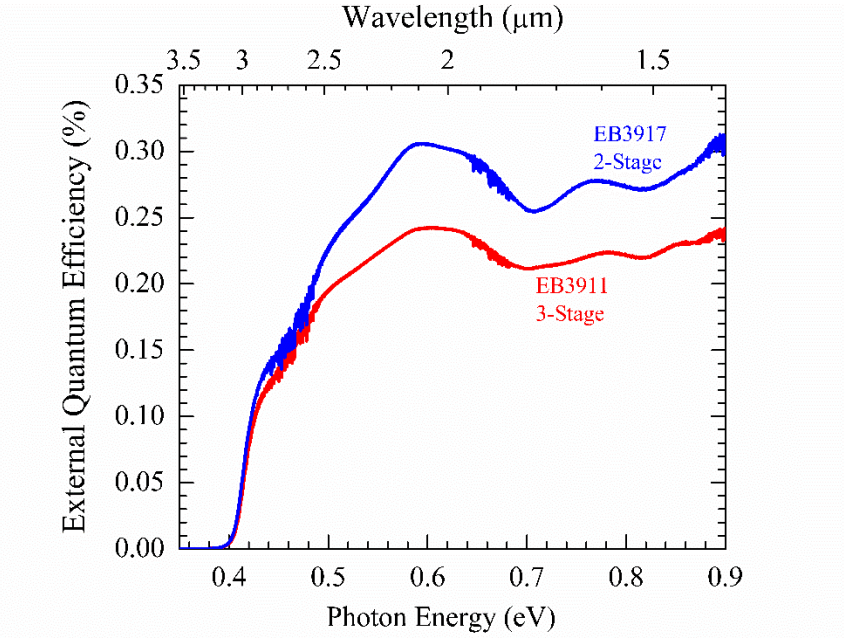

Figure 4.9: External quantum efficiencies for devices from wafers EB3911 and EB3917 at 300 K. The dimensions for both devices were 0.4x0.4 mm^2.

For the PV characterization of these devices, an interband cascade laser source was used. The laser provided the higher power needed for these devices to achieve comparable short-circuit densities to other TPV cells reported in the literature. The emission photon energy of the mid-infrared laser used was about ~0.42 eV. This was slightly higher than the absorber bandgap. Typical *J-V* curves for EB3911 and EB3917 are shown in Fig. 4.10 for temperatures of 300 K and 340 K. The devices from both wafers had mesa dimensions of 0.3x0.3 mm^2. The data was acquired while the devices were under illumination from the mid-infrared laser. The inset shows the emission spectrum of the laser used for the characterization compared to the electroluminescence (EL) spectrum of the PV device. Both the laser spectrum and the EL spectrum of the PV device have their spectral peaks near ~0.42 eV.

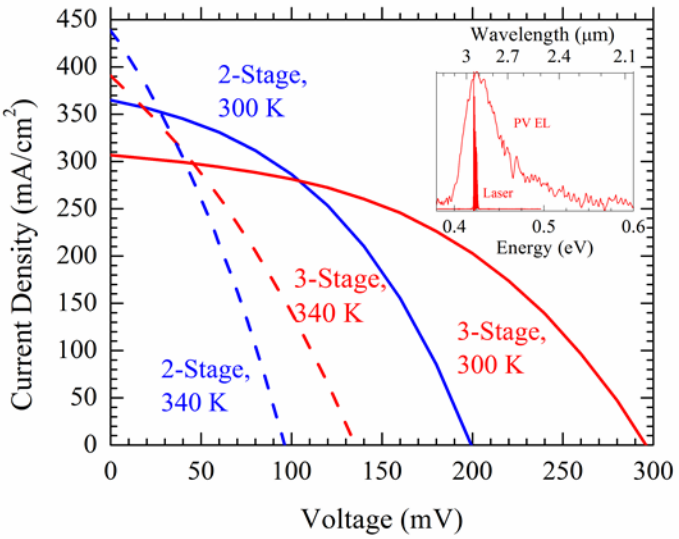

Figure 4.10: Measured J-V curves of devices from wafers EB3911 and EB3917 under illumination from a mid-infrared laser. Both devices had 300x300 μm^2 square mesas. The incident intensity was the same for each of the curves shown. The inset shows the emission spectrum of the laser used for characterization and the electroluminescence spectrum of the PV device acquired at 300 K.

The three-stage device was able to achieve higher values of open-circuit voltage (V_{oc}) and fill factor (FF) than the two-stage device, as expected. However, the short-circuit current density (J_{sc}) value was about ~16% lower in the three-stage device. This is due to the mismatch of photocurrent between the different stages. There were similar differences in the J_{sc} values obtained under blackbody illumination for the two- and three-stage devices. This indicates that better performance of the three-stage device should be possible simply by improving the photocurrent-matching between the stages. However, the photocurrent-matching was good enough that the three-stage devices achieved higher output powers under equivalent illumination conditions.

Both devices show an expected decrease in both V_{oc} and FF as the temperature was increased from 300 K to 340 K. However, it is noteworthy that there is a strong increase in the short-circuit current. This is due to the decrease in the bandgap (estimated to be ~10 meV from the cutoff the in the response spectra). This is noteworthy because it demonstrates the preservation of high carrier collection in IC PVs at high temperature.

Under laser illumination, the three-stage device had J_{sc} = 310 mA/cm^2, V_{oc} = 295 mV, and FF = 44%. This V_{oc} value is comparable to those of the GaSb-based TPV devices reported in Ref. 117, which ranged from 240-320 mV (with bandgap ranged from 0.50-0.55 eV), under a much higher incident light intensity (the reported J_{sc} is about an order of magnitude higher than that of our device). However, the FF values for those devices were 58-66%, which is significantly higher than our values. The source of a lower than expected fill factor is usually series resistance dissipation or shunting effects. The shape of the *J-V* curves at 300 K are actually consistent with what would be expected if there were shunting currents. A more detailed study of the possibility of surface shunting is carried out below.

Now we will discuss the efficiency with which the devices are able to convert the laser power. In this experiment, the spot size of the laser was larger than the device. Therefore, it was not known a priori how much laser power was actually incident on the cell during the experiment. However, this value can be estimated using the calibrated EQE, and the measured J_{sc}. The laser power, P_{inc}, for a laser emitting photons with energy E_{ph} is given as:

$$P_{inc} = \frac{E_{ph} J_{sc}}{e \eta_{\lambda}}, \tag{4.7}$$

where η_{λ} is the EQE of the cell at the lasing wavelength. Thus, the efficiency, *EFF*, with which a PV cell converts laser power can be expressed as:

$$EFF = \eta_{\lambda} FF \frac{V_{oc}}{(E_{ph}/e)}, \tag{4.8}$$

where we note that the term E_{ph}/e in the denominator is the photon energy in units of eV. The EQE of the 3-stage device is about ~8.0% at 0.42 eV, while that of the 2-stage device is ~9.2%. From this, the laser power incident on the 3-stage device is determined to be 1.6 W/cm^2, and the power incident on the 2-stage device is determined to be 1.7 W/cm^2. This difference is

reasonable due to the uncertainties in the EQE calibration and the laser alignment. For the 3-stage device the efficiency is found to be about ~2.5%, while that of the 2-stage device is found to be about ~1.9%. This was used previously to estimate the power efficiency of a device from EB3337 under laser illumination [114]. Under comparable power, the efficiency of that device was about ~0.6%. Note that the PV conversion efficiency will increase as the source power becomes stronger, due increases in the V_{oc} and FF.

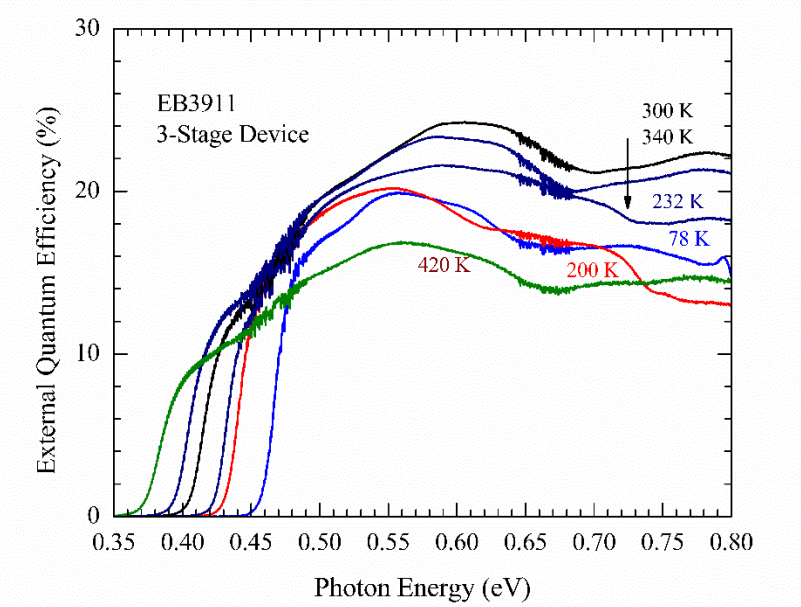

Figure 4.11 External quantum efficiency of device from 3-stage wafer EB3911 at different temperatures.

In order to get a better understanding of the underlying device physics, the photoresponse and dark current were studied as a function of temperature for devices from both structures. The EQE for a device from wafer EB3911 for is shown in Fig. 4.11 for a series of temperatures from 78 K to 420 K. The competing effects of bandgap-narrowing and shortening of the diffusion length can be seen by studying the temperature-evolution of the EQE curve. The bandgap-narrowing effect pushes the absorption edge to lower energies, and increases the overall absorption at energies well above the bandgap. However, the reduction of the diffusion length at

high temperature results in fewer excited carriers being collected. This effect is why the EQE at higher energies drops from 340 K to 420 K.

For applications, the relevant parameter of interest is the total current that flows in response to radiation from a source. Fig. 4.12 shows the photocurrent that would flow in devices from the two wafers when under illumination by a 1000 K blackbody source. These values were actually calculated from the calibrated quantum efficiencies, rather than directly measured. In this situation, the blackbody temperature was taken to be 1000 K, and it was assumed to be emitting from an aperture with radius of 0.762 cm. Note that the shape of the curve will not be changed by the choice of a different aperture size.

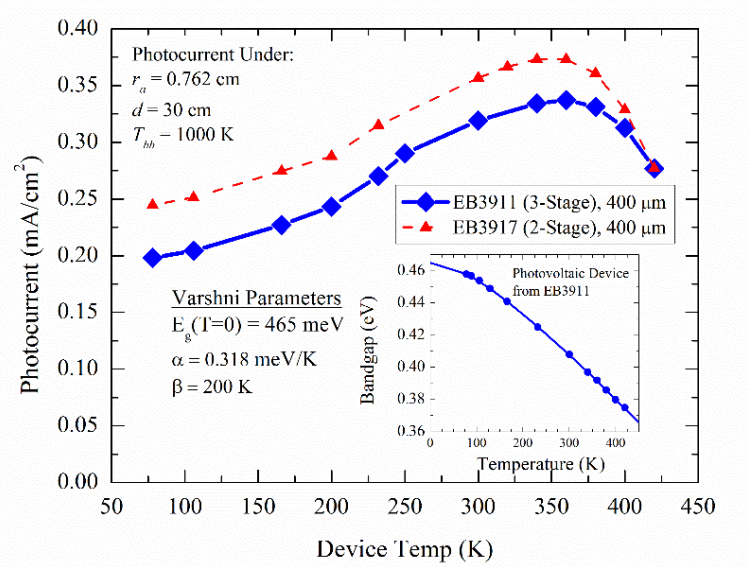

Figure 4.12: Temperature-dependence of photocurrent under a 1000 K blackbody in devices from EB3911 and EB3917. The values were calculated by integrating of the calibrated external quantum efficiency. The inset shows how the bandgap of a device from EB3911 changes with temperature. The Varshni parameters describing the temperature-dependence of the bandgap are shown.

From Fig. 4.12, it is seen that for both 2- and 3-stage devices, the photocurrent increases in the range of 78 K up to room temperature and slightly above. This is consistent with the laser measurements. A decrease in photocurrent is not seen until about 375 K. Even for temperatures

as high as 420 K a strong signal is maintained. This result suggests that at the operating temperature of 300 K, a minimal number of excited carriers are lost to recombination. This provides additional validation that the multiple-stage, short-absorber design should be able to overcome some of the obstacles typically associated with the conversion of mid-infrared radiation at room temperature.

The temperature-dependence of the dark current was also studied. This was done in the temperature range of 150-420 K. In this range, the thermal noise level was higher than the average background current, so no shielding of the devices was needed. The specific parameter that was studied was the zero-bias resistance-area product, R_oA. For single-absorber photovoltaic devices, R_oA is related to the magnitude of the expected saturation dark current, J_{sat}, by:

$$R_oA = \frac{k_bT}{qJ_{sat}}. \tag{4.9}$$

For a multiple-stage device with N_s stages, the value of R_oA is higher by a value of N_s.

The temperature-dependence of R_oA will be controlled by the main transport mechanism that governs the dark current. The expected temperature-scaling, if the current is bottlenecked by transitions across the absorber bandgap has the form:

$$(R_oA)^{-1} = CT^q e^{-E_a/k_bT}, \tag{4.10}$$

where C, q, and E_a are fitting parameters. The parameter E_a is referred to as the activation energy. In certain limits, the activation energy is expected to scale either as either E_{g0} or $E_{g0}/2$, where Eg_0 is the bandgap at zero Kelvin [118]. This value was found for the two samples by extrapolating the temperature-dependence of the absorber bandgaps. The extrapolation was done by using the Varshni formula [119]:

$$E_g(T) = E_{g0} - \frac{\alpha T^2}{\beta + T}, \tag{4.11}$$

where α, β, along with E_{g0} compose the Varshni parameters describing the temperature-dependence of a given semiconductor. The fitting of the temperature-dependent bandgap for a device from wafer EB3911 is shown in the inset to Fig. 4.12. The fitted parameters are also shown. These parameters were found to be a good fit for the devices processed from both wafers.

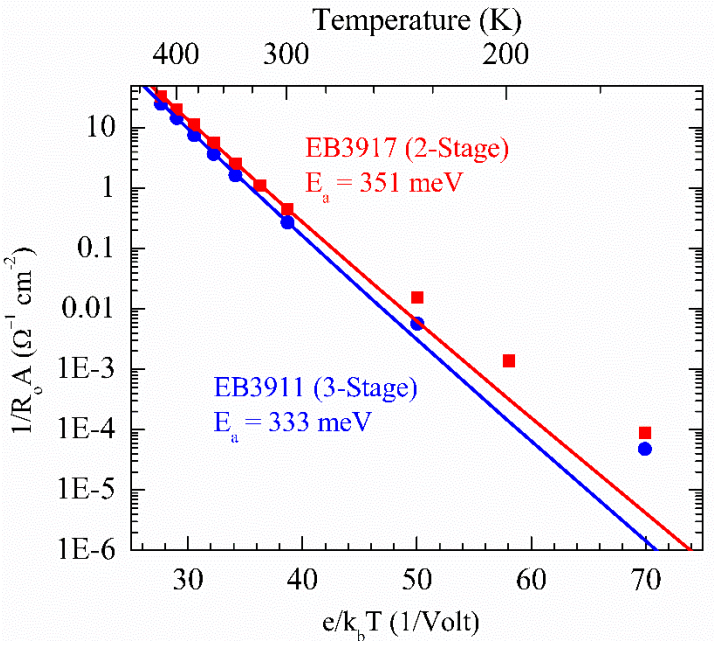

Figure 4.13: Arrhenius plot of measured $(R_oA)^{-1}$ over temperature range of 150-420 K for devices from EB3911 and EB3917. The activation energies correspond to the case of q=2 in Eq. 4.9.

An activation energy of E_{g0} is expected when the transport is diffusion limited. An activation energy of $E_{g0}/2$ is expected when the transport is dominated by the g-r mechanism in the depletion region. An activation energy lower than $E_{g0}/2$ typically indicates current conduction through leakage channels. Activation energies higher than the bandgap are typically not observed. The value of q is expected to be equal to 1 if the dark current scales with n_i (the generation-recombination limit) and equal to 2 if it scales with n_i^2 (diffusion limit). However, the temperature-modulation will also be influenced by the temperature-dependence of the carrier

lifetime, as well as the temperature-dependence of the diffusion coefficient if there is less than 100% collection of thermally generated carriers.

Arrhenius plots of the temperature-dependence of $(R_oA)^{-1}$ for devices from both wafers are shown in Fig. 4.13. The fitting was done for temperatures in the range of 240 K – 420 K. The result of fitting of the data to Eq. 4.9 is also shown for the case of q=2. As seen, for temperatures below 240 K, the $(R_oA)^{-1}$ for both devices is higher than what is predicted by the high temperature trend lines. This is because at lower temperatures, more of the current conduction is occurring through the non-ideal channels. The fitting results for two other devices from wafer EB3911 are summarized in Table 4.2 and those for four other devices from wafer EB3917 are summarized in Table 4.3. The tables present the fitting results for the cases of q=1, q=2, and q=3.

As expected, the R_oA values are higher for the 3-stage device, due to the additional stage. For both devices the fitted E_a values are between E_{g0} and $E_{g0}/2$ for the case of q=2. The largest fitted values are for q=1. Even for this choice of q, the fitted E_a values for EB3917 are over 50 meV less than E_{g0} for for EB3911 they are about 100 meV less than E_{g0}. They are also less than E_g at 300 K. From this comparison, it can stated that the transport in devices from both wafers is not completely determined by the diffusion mechanism. This is actually consistent with the results of a variable-area study presented below, which shows that there is significant current conduction along the perimeter of the devices. However, the data in Tables 4.2 and 4.3 do not indicate a correlation between device size and the fitted E_a. Thus, the surface leakage probably does not account for the sub-E_{g0} activation energy

An interesting observation is that the fitted values of E_a for the two-stage devices are higher than those of the three-stage devices. The difference in E_a for the devices from the two

wafers is about 30-40 meV. This variation is larger than what the author would expect from random sample-to-sample variations in material or processing quality. This suggests that the unknown mechanism causing the deviation from the diffusion limit may be related to transport between stages.

Wafer EB3917, 2-Stage E_{g0} = 465 meV		High Temperature Activation Energies		
Device	Mesa Edge	q=1	q=2	q=3
A	500 μm	388 meV	358 meV	328 meV
F	400 μm	382 meV	356 meV	326 meV
H	400 μm	381 meV	351 meV	320 meV

Table 4.2: Fitted values of activation energy for devices from sample EB3917. This sample had three stages and was designed for photocurrent-matching.

Wafer EB3911, 3-Stage E_{g0} = 465 meV		High Temperature Activation Energies		
Device	Mesa Edge	q=1	q=2	q=3
A	200 μm	357 meV	327 meV	297 meV
B	300 μm	343 meV	313 meV	282 meV
C	400 μm	363 meV	332 meV	302 meV
D	500 μm	372 meV	342 meV	311 meV
E	1000 μm	344 meV	314 meV	284 meV

Table 4.3: Fitted values of activation energy for devices from sample EB3911. This sample had two stages and was designed for photocurrent matching.

4.3.4 Influence of Surface Conduction

The elimination of leakage current channels is an important focus in optoelectronic device fabrication. One source that is often problematic in devices based on InAs [120] and similar materials such as InAs/GaSb SLs [121] is charge conduction along the surface. The termination of the crystal periodicity and the resulting dangling bonds create surface states. This extra charge leads to pinning of the Fermi level at the surface. In GaAs, this pinning is usually near the center of the bulk bandgap. In materials with low-lying conduction bands, such as InAs, the Fermi level can actually be pinned above the conduction band edge [122]. This is shown for a device with a p-type absorber in Fig. 4.14.

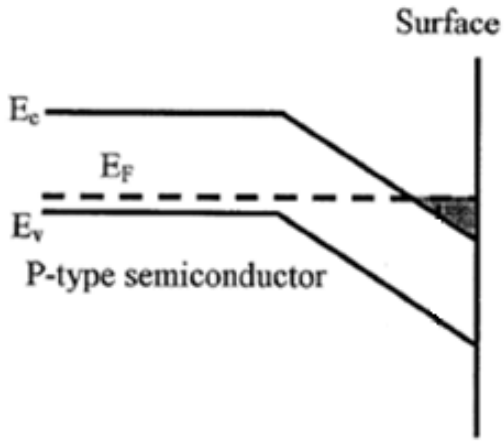

Figure 4.14: Pinning of Fermi level at the surface in p-type material such as InAs or InAs/GaSb SL that has a low-lying conduction band. Since the Fermi level is pinned above the conduction band, an inversion layer is formed on the surface. Figure is adopted from Ref. 121.

When the Fermi level is pinning above the conduction band edge, this can lead to the formation of an inversion layer at the surface. The inversion region creates a channel by which carriers can flow between the device contacts in a nearly-ohmic manner. The formation of an inversion layer is a well-known problem in InAs-based infrared detectors. Addressing this problem was part of the impetus for the original nBn design [33].

In PV energy-conversion devices, which operate in forward-bias, the surface shunting currents run opposite to the photocurrent. The net effect of this is a reduction of the reverse current at a given voltage. This leads to a reduction in the fill factor, and can also reduce the open-circuit voltage. It should be noted that there is a difference between surface conduction and surface generation-recombination. The later effect refers to the generation or recombination of an electron-hole pair.

In the above analysis of the devices from wafer EB3337, it was established that the transport was not diffusion-limited and there was some source of leakage current. One of the proposed leakage channels was along the surface. However, at the time a thorough examination of this was not carried out. In order to study this effect in the devices from EB3911 and EB3917,

a variable-area device analysis was conducted. A variable-area analysis exploits the fact that the percentage of surface vs. bulk conduction in a device changes as a function of the perimeter-to-area ratio of the device mesa.

For this experiment, several arrays of devices were cut from the processed material and mounted onto ceramic chip carriers. Each array contained 22 devices with mesa dimensions ranging from 0.2x0.2 mm^2 to 1.0x1.0 mm^2. The relationship between the device edge length, *r*, and the perimeter-to-area, *P/A*, ratio is given by $P/A = 4/r$. For each of the devices, the dark current at room temperature was measured at a reverse bias voltage of -200 mV. In reverse bias, the bulk generation current, J_{bulk}, and the surface current flow in the same direction. For ohmic surface conduction, the relationship between the total dark current, J_{tot}, and the device *P/A* is given by [123]:

$$J_{tot} = J_{bulk} + \frac{V}{\rho_{sw}} \frac{P}{A}, \tag{4.12}$$

where ρ_{sw} is the resistivity of the device sidewall.

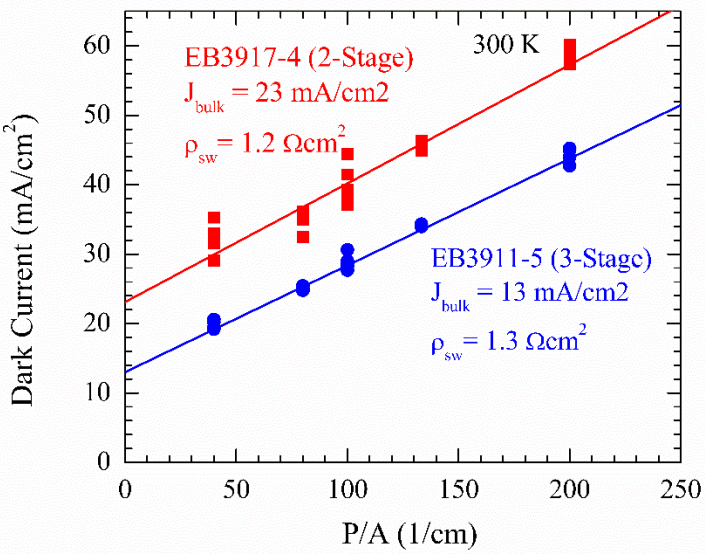

Figure 4.15: Dark current density as a function of device perimeter-to-area ratio from which bulk current density and sidewall resistivity from devices from wafers EB3911 and EB3917 are extracted. The dark current was measured at a reverse bias voltage of -200 mV.

The parameters J_{bulk} and ρ_{sw} for each of the device arrays were obtained by fitting the measured J_{tot} values to Eq. 4.11. The results for an array from EB3911 and an array from EB3917 are shown in Fig 4.15. As seen, the predicted linear relationship between J_{tot} and *P/A* was observed in both wafers. The extracted parameters indicate that the surface contribution to the total current is substantial. The percentage of total current that flows along the surface varies from about 30% for the large devices to as much as 70% for the smallest devices.

The fitting results for each of the device arrays that contained a large amount of working devices are tabulated in Table 4.4 for wafer EB3911 and Table 4.5 for wafer EB3917. The number of working devices that had dark current values included in the fits are also displayed in the tables. Some of the arrays (i.e. Array 1 from EB3911) did not have a large number of working devices and are thus not included in the su1.mmary. As seen, the extracted J_{bulk} values were larger for the 2-stage device arrays. This result is expected. For a 2-stage and 3-stage device under the same total bias voltage, the voltage applied to an individual stage will be less for the 3-stage device. This will lead to less generation current in these devices at a given voltage. The sidewall resistivity values are found to be larger for the 3-stage device arrays. The difference between the two is about 300 mΩ cm^2. Although this difference is small, there is a clear observable trend. The reason for this difference may be the fact that the three stage devices utilize a thicker overall structure.

	EB3911 (3-Stage) Device Arrays at V = -200 mV		
	Array 2	Array 4	Array 5
Devices	14	21	19
J_{bulk}	14 mA/cm^2	13 mA/cm^2	13 mA/cm^2
ρ_{sw}	1.3 Ωcm^2	1.4 Ωcm^2	1.3 Ωcm^2
% Surface (0.2 mm)	69%	69%	70%
% Surface (1.0 mm)	31%	31%	31%

Table 4.4: Fitting parameters obtained from wafer EB3911 of J_{tot} vs. P/A for 3 different arrays of devices.

	EB3917 (2-Stage) Device Arrays at V = -200 mV			
	Array 1	Array 2	Array 3	Array 4
Devices	15	11	18	19
J_{bulk}	16 mA/cm^2	18 mA/cm^2	20 mA/cm^2	23 mA/cm^2
ρ_{sw}	1.0 Ωcm^2	1.0 Ωcm^2	0.92 Ωcm^2	1.2 Ωcm^2
% Surface (0.2 mm)	71%	69%	67%	59%
% Surface (1.0 mm)	33%	31%	31%	23%

Table 4.5: Fitting parameters obtained from wafer EB3917 of J_{tot} vs. P/As for 4 arrays of devices.

The results presented establish that, in addition to the intrinsic current due to interband generation, there is additional current caused by surface conduction. Since the inversion layer conduction channel is expected to be Ohmic, it will also conduct leakage current in forward bias. As stated earlier, this current runs in the opposite direction as the photocurrent, and reduces the fill factor and open-circuit voltage. In order to check this, the photovoltaic properties of the devices discussed above were also checked. In this experiment, the devices were illuminated by the blackbody source. The illumination was kept fairly weak in order to avoid heating the devices. The results are shown in Fig 4.16, which shows the measured V_{oc} and J_{sc} values as a function of P/A ratio. As seen, in the smaller devices, where the perimeter conduction effect will be stronger, the open-circuit voltage is lower. The perimeter effects do not influence the value of the short-circuit current. The slightly lower value of J_{sc} for the 0.2x0.2 mm^2 devices is likely due to a fact that the metal contacts in the smaller devices take up a larger percentage of the top surface. The fact that P/A strongly influences V_{oc}, but not J_{sc} is consistent with what would be expected from surface shunting effects.

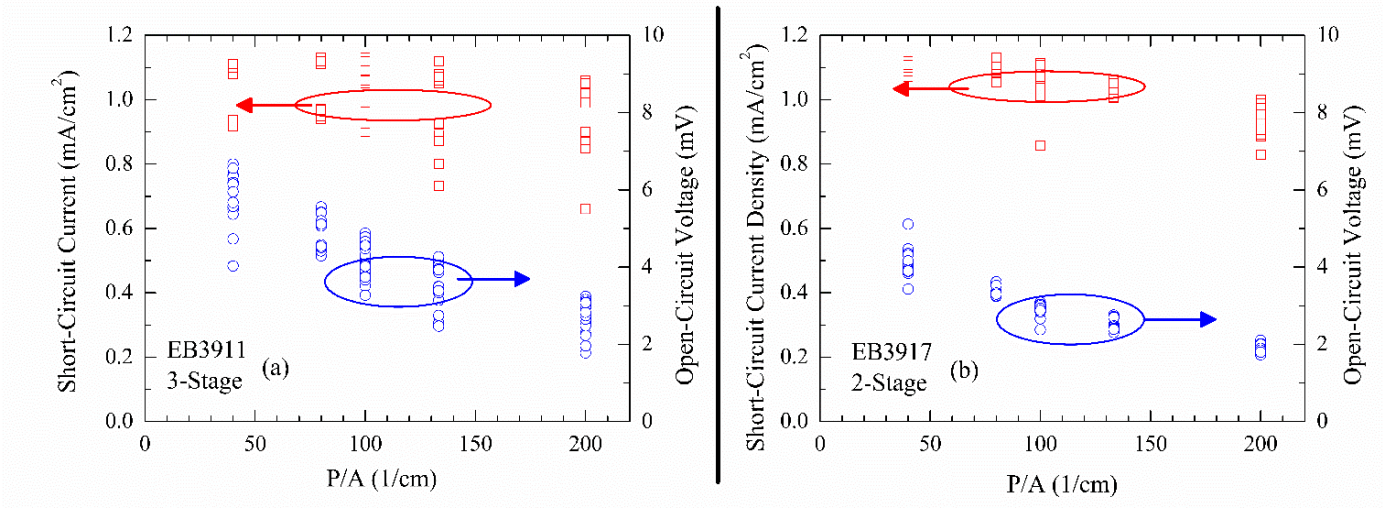

Figure 4.16: Dependence of short-circuit current density and open-circuit voltage on device perimeter-to-area ratio for devices from EB3917 and EB3911.

Chapter 5 : Experimental Comparison of Single- and Multiple-Stage MWIR Detectors

5.1 Introduction

In Chapter 3, a theoretical discussion was presented that detailed how an ICIP design can be beneficial for improving the sensitivity of photovoltaic detectors. At the end of that chapter, it was stated that a multiple-stage design may be particularly useful for improving the sensitivity of infrared detectors operating at high temperatures (> 200 K). This is because a reduction in quantum efficiency is typically observed in single-absorber detectors at these temperatures. This has been observed by several groups [124,125]. A reduced quantum efficiency at high temperature implies that photo-excited electrons that would be collected at low temperature are not collected at high temperature. An ICIP responds to this intrinsic limit on photocurrent by using multiple short-absorber stages to lower the detector noise. By using a multiple-stage architecture, the "wasted photons" that would excite uncollected electrons in single-absorber detectors are instead utilized to drive the photocurrent in the optically deeper stages.

In Chapter 4, it was shown that devices from wafer EB3337, which had cutoff wavelengths of ~5 μm at room temperature, had EQE values that increased as the temperature was raised from 78 K up to room temperature. The wider-bandgap devices from wafers EB3911 and EB3917 did not show a decrease in photocurrent until ~375 K. In addition, operation of an ICIP with a room temperature cutoff wavelength of ~6.2 μm at temperatures of 420 K has also been shown by the University of New Mexico [126]. These results are positive affirmations of the ability of multiple-stage devices to maintain a strong photoresponse at high temperature. What has been missing hitherto, both in this dissertation and the literature, is a direct experimental comparison of the temperature-dependence of the photocurrent and sensitivity of single- and multiple-stage detectors with similar designs. In this chapter, we present such a

comparison for a set of five detectors that use InAs/GaSb SL absorbers with MWIR cutoff wavelengths.

5.2 Structure Details for R100 Detector Series

The five wafers used to fabricate this series of MWIR detectors are denoted as R100, R101, R102, R103, and R104. The epitaxial structures were grown by Hao Ye at the University of Oklahoma. The growth of this set of samples was done within a two-week period in late March and early April of 2013. Thus, the growth conditions and material quality should be similar for all the samples.

Wafer	Number of Stages	Total Absorber Thickness	Stage Absorber Thickness
R100	1	1.32 μm	Single absorber was 1320 nm
R101	1	2.32 μm	Single absorber was 2320 nm
R102	15	2.32 μm	All stages were identical
R103	2	1.32 μm	605 nm, 710 nm
R104	3	1.32 μm	634 nm; 754 nm; 936 nm

Table 5.1: Design details for the ICIP wafers in this study.

The primary design difference between the five wafers was in the choice of the number of stages and absorber thickness. Wafers R100 and R101 were both single-stage devices, with total absorber thicknesses of 274 SL periods (~1.32 μm) and 484 SL periods (~2.32 μm), respectively. Wafer R102 was designed to have 15 identical stages. The absorbers in this structure were fairly short, consisting of 33 SL periods (~158 nm). Wafers R103 and R104 were multiple-stage devices, where the absorber thicknesses were varied across the structure in order to achieve a rough matching of the photocarrier generation rate in each stage. In these samples the optically deeper stages were made thicker, since light attenuation in the shallower stages causes fewer photons to be incident on these stages. The absorbers in the two stages in wafer R103 had 126 (~605 nm) and 148 (~710 nm) periods respectively. The absorbers in three stages in wafer R104 had 132 (~634 nm), 157 (~754 nm), and 195 periods (~936 nm), respectively.

Note that the total absorption thicknesses of R103 was equal to the absorber thickness of R100, and that the total absorption thicknesses of R101, R104, and R102 are also equivalent.

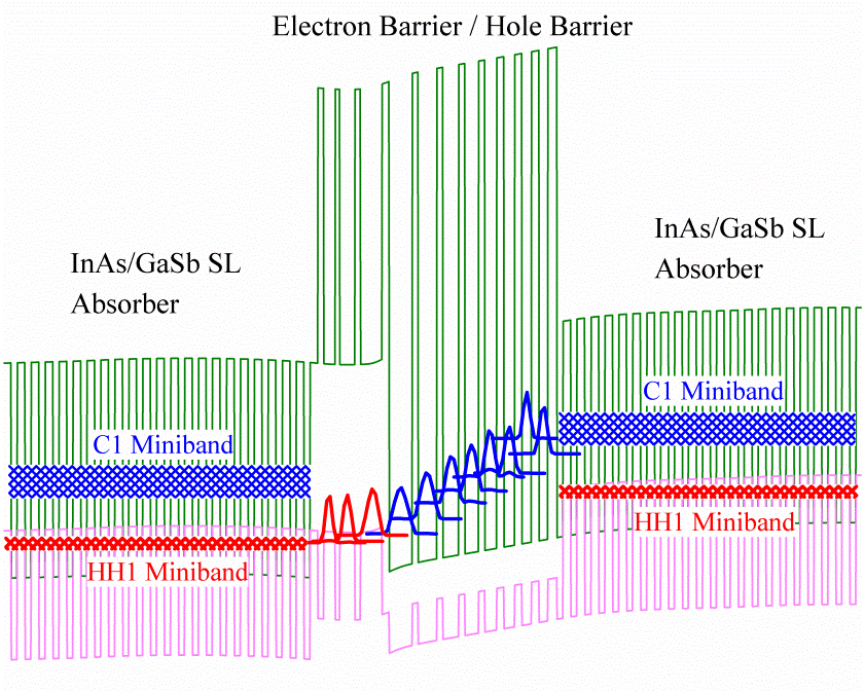

Figure 5.1: Calculated band profile of one stage of a detector from samples R103 under reverse bias. The blue and red rectangles in the absorber represent electron and hole minibands. The ground state energy levels and calculated wavefunctions for the QWs of the barrier regions are shown. The blue wavefunctions represent electron states in the conduction band of the hole barrier and red wavefunctions represent the hole states in the valence band of the electron barrier.

The calculated band profile for sample R103 under a reverse bias is shown in Fig. 5.1. The calculation procedure is similar to that described in Chapter 4 for sample EB3337. As before, it is seen that the voltage is primarily applied to the barrier regions. As noted above, the basic stage design for each of the samples is the same. The only change between the samples was in the choice of the number SL absorber periods, and the thickness of the electron barriers, which were made slightly thicker in the single-stage devices. The hole barrier consisted of a series of InAs/AlSb QWs, while the electron barrier consisted of a series of GaSb/AlSb QWs. Note that the several of the AlSb layers in the interior of the hole barrier actually had a very thin

layer of InSb grown in the center. This was done to ensure a local strain balance. This was not accounted for in the calculated bandstructure of Fig. 5.1. The electron barrier in the multiple-stage samples consisted of 3 total QWs, while those in the one-stage samples were made slightly thicker and consisted of 5 QWs. As seen in Fig. 5.1, the series of wells in both barriers were digitally graded so that the energy difference between the ground states of the electron and hole barriers is either nearly zero or within a thermal energy k_bT. This was done to ensure fast thermalization of the carriers in these two regions. The period of the absorber SL for each of the structures was composed of a 20.5 Å-thick InAs layer (7 ML) and a 27.5 –thick GaSb layer (9 ML). The GaSb-on-InAs interface was forced during the growth to be InSb type, while the InAs-on-GaSb interfaces did not have a forced interface type.

Some *p*-doping of the GaSb layers in the structure was done by introducing Be dopants, so that holes were the majority carriers in the absorber. However, in contrast to our previous designs, where the entire absorber region and electron barrier were doped, the samples studied here only had a partially doped absorber. The GaSb layers in the electron barrier, along with those in the 1/3 of the absorber closest to the electron barrier were doped p-type with an acceptor concentration of 3.5×10^{16} cm^{-3}. This introduction of a doping gradient was done as a precaution against detrimental band-bending in the absorber due to hole accumulation in the GaSb layers in the electron barrier [14].

The epitaxial growth sequence of a single stage consisted of the electron barrier being grown on top of the absorber, which was grown on top of the hole barrier. With this illumination geometry, the light is incident from the opposite side of the collection point. As noted in Chapter 3, this design choice actually results in a lower signal in situations where slow diffusion limits the carrier collection process.

5.3 Device Characterization Results and Analysis of R100 Series

5.2.1 Overview of Devices and Dark Current Analysis

Square mesa ICIPs were processed from the epitaxial material. The processing was done using the same wet-etch recipe described earlier. The photomask was the same as the one used to process the devices from wafers EB3911 and EB3917. Thus, the device mesas had edge lengths ranging from 0.2 mm to 1.0 mm. Arrays of devices were cut from the processed material, mounted on a heat sink, and wire bonded. Micrographs of the mounted and bonded square-mesa devices can be seen in Fig. 5.2. No anti-reflection coating was deposited, so an inherent 30% reflection loss of incoming photons are expected to be lost due to the index contrast between air and the planar semiconductor surface.

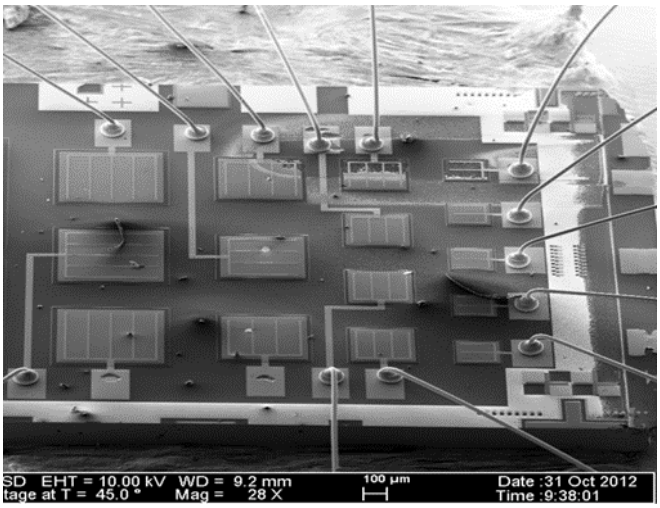

Figure 5.2: Micrograph of processed and wire-bonded detector samples taken using scanning electron microscopy. The image was provided by Dr. Lu Li.

The dark current-voltage characteristics of the device were measured for a range of temperatures. At low temperatures, a cold shield was used to block the extraneous background radiation. From the measured dark current-voltage curves, the R_oA values were extracted in order to determine the detector noise when operated under zero bias.

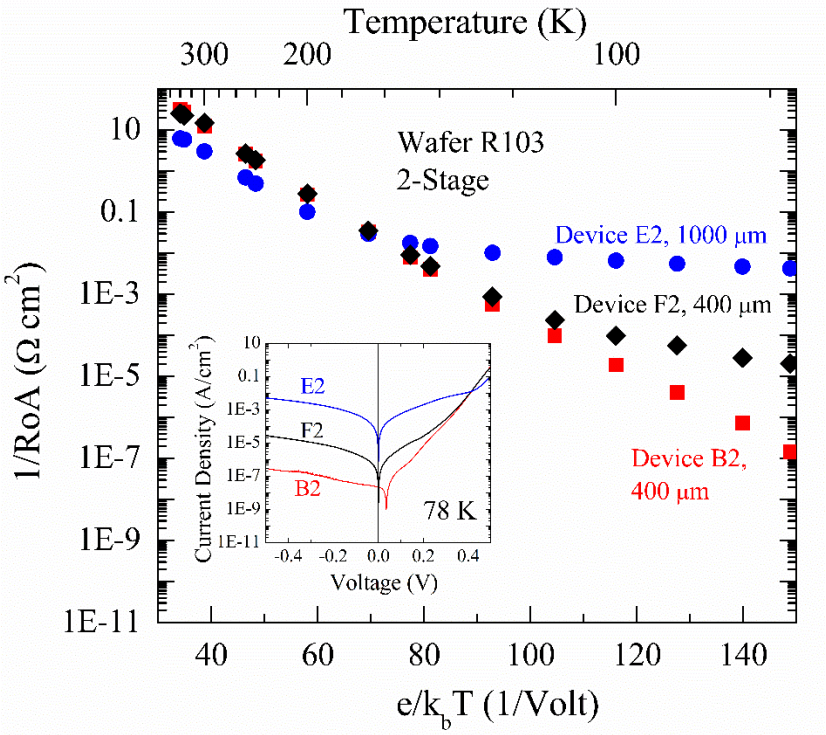

Figure 5.3: Arrhenius plot shown the temperature-dependence of $(RoA)^{-1}$ for three devices from wafer R103. R103 is a two-stage wafer designed for photocurrent-matching. The inset shows the dark current densities as function of voltage for the three devices at a temperature of 78 K.

At low temperatures, a strong variation in the dark current was observed for devices that were processed from the same wafer. This can be seen in Fig. 5.3 for a set of devices processed from wafer R103. The figure shows an Arrhenius plot comparing the $(R_oA)^{-1}$ of three devices from the same device array as a function of temperature. It can be seen that at low temperatures, the $(R_oA)^{-1}$ values vary by orders of magnitude from device-to-device. The dark current density of the devices also varies by orders of magnitude. The inset of the figure shows the dark *J-V* characteristics of the three devices acquired at 78 K. Typically, the dark current density of devices from the same wafer should not vary by more than one order of magnitude, even at low temperature where some non-uniformity between the devices would be expected.

As seen, the temperature-dependence of the $(R_oA)^{-1}$ for devices E2 and F2 is very weak at low temperature. In contrast, the dark current of device B2 is strongly dependent on temperature

over the whole temperature range. For this device, there is no "roll-over" in $(R_oA)^{-1}$ at low temperature, and the data for the whole 78-350 K temperature range would seemingly be well-fit by a single exponential function. The most logical explanation for this observation is that there is some leakage channel present in devices E2 and F2 that dominates the transport at low temperature. In device B2, this channel is not present. Thus, we can assert that the transport in this device is bottlenecked by the absorber interband transition across the whole temperature range. Unlike the surface issues discussed in Chapter 4, the leakage in devices E2 and F2 does not appear to be a perimeter effect, since there is no correlation between the *P/A* value of the devices and the $(R_oA)^{-1}$ values. Recent work has indicated this problem is most likely introduced during the SiO_2 deposition process [127]. In this experiment, the dark current of devices passivated with SiO_2 and Si_3N_4 was compared. The wafer used was an ICIP structure with a similar cutoff wavelength as the series of wafers discussed in this section. At 78 K, the devices passivated with SiO_2 had similar variations in the low temperature R_oA values as those presented above from R103. However, the devices passivated with Si_3N_4 (with heating) had dark current densities that were consistent within an order of magnitude. In addition, the dark current of the devices passivated with Si_3N_4 were generally found to be lower than those passivated with SiO_2. Thus, further improvement of the SiO_2 deposition is needed to resolve the observed non-uniformity in dark current.

At higher temperatures, it can be seen that there is more consistency in the values and temperature-dependence of the $(R_oA)^{-1}$ of different devices from wafer R103. Similar converging of the dark current for devices from the same wafer was seen in the other wafers. Thus, it is believed that the leakage current present at low temperature is not limiting the high temperature performance, which is what we are most interested in studying with this set of samples.

Sample	Total Absorption Thickness	Mesa Edge	E_g(0 K)	High Temp. Activation Energy		
				q=1	q=2	q=3
R100	1.32 μm	400 μm	303 meV	175 meV	158 meV	141 meV
R101	2.32 μm	300 μm	296 meV	166 meV	149 meV	132 meV
R102	2.38 μm	1000 μm	298 meV	166 meV	144 meV	122 meV
R103	1.32 μm	400 μm	296 meV	177 meV	155 meV	133 meV
R104	2.32 μm	200 μm	296 meV	186 meV	164 meV	141 meV

Table 5.2: Details on wafers used in study and representative devices from each wafer.

For the temperature-dependent performance study presented below, representative devices were chosen from each wafer. To avoid uncertainty introduced by the leakage current, the devices chosen were the ones that demonstrated the best performance at low temperature. The mesa sizes for the devices are shown in Table 5.2, along with the estimated E_{g0} values for each of the corresponding wafers. The temperature-dependence of the absorber bandgaps was estimated from the 10% cutoff wavelength of the relative response spectra, measured using the FTIR. The values of E_{g0} were found by fitting the temperature-dependent bandgaps to the Varshni formula, given in Eq. 4.10. The fitting result is shown in Fig. 5.4 for the device from wafer R101.

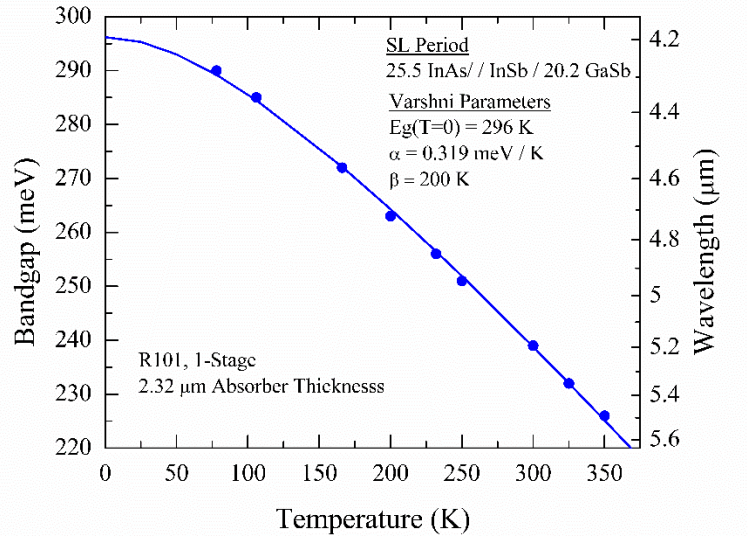

Figure 5.4: Temperature-depedent cutroff wavelength and estimated bandgap for device from wafer R101. The fitted Varshni parameters for the device are shown.

From Table 5.2, it can be seen that samples R101, R103, and R104 have zero-temperature bandgaps that are equal to three significant digits. In addition, the devices from these three wafers had fairly consistent bandgaps across the whole temperature range examined. The value of E_{g0} for R102 was about 2 meV higher, while that of R100 was about 7 meV higher. We believe that the difference in E_{g0} between R102 and the first three wafers devices is not significant enough to conclude that there are large differences in the absorber composition of that sample compared with the other three. However, as seen in more detail below, there was some unusual behavior exhibited by the devices from sample R100. Note that the structural characterization did not illuminate any significant differences in the material quality of R100 compared with the other samples.

Fig. 5.5 shows an Arrhenius plot of the temperature-dependent $(R_oA)^{-1}$ values obtained for the five representative devices from each sample. The temperature dependence was fit to Eq. 4.9. The fitted activation energies for the cases of q=1, q=2, and q=3 are shown in Table 5.2. The values displayed in Fig 5.5 correspond to the case of q=2. It can be seen that the temperature-dependent data for the devices from wafers R101, R103, and R104 can be well-fit using a single activation energy for the entire temperature range of 78 K – 350 K. The fitted values of E_a for the three samples are within 10 meV. For reference, the results are compared with the predicted R_oA value from "Rule 07" for MCT detectors [54]. Rule 07 is an equation that gives the approximate dark current that can be expected for a diffusion-limited MCT detector with a certain cutoff wavelength at a certain temperature. The formula was found by fitting the dark current data for a large number of MBE-grown MCT detectors. For the researchers working on InAs/GaSb SLs it provides a useful benchmark [11]. As seen, at high temperature, the ICIPs in this study are actually able to exceed MCT Rule 07. This is due to the fact that the

absorbers are shorter and because the devices utilize multiple stages. However, the ICIP R_oA data shows a weaker dependence on temperature than the Rule 07 curve. The fitted E_a values are fairly close, but slightly larger than $E_{g0}/2$. As noted in Chapter 4, this indicates that the dark current is scaling with n_i, rather than n_i^2. This indicates that the current is determined by the interband generation-recombination events, but that these events are occurring in a region of carrier depletion. This may indicate that the absorber is not a field-free region, as it was designed. Another possibility is that band bending on the device perimeter is causing a depletion region to form near the device surface.

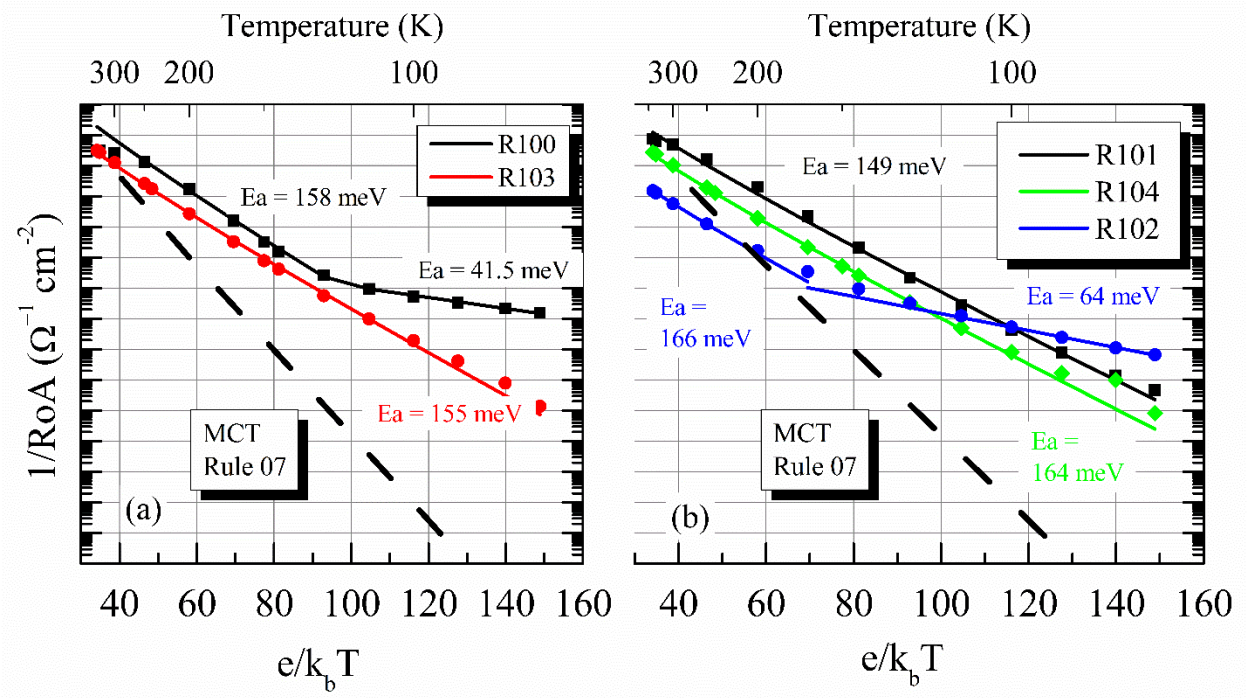

Figure 5.5: Arrhenius plot of measured $(R_oA)^{-1}$ is shown in (a) for the samples that had a total absorption thickness of 1.32 µm and in (b) for the samples that had a total absorption thickness of 2.32 µm. The fitting results correspond to the case of q=2. As a guide, the $(R_oA)^{-1}$ value predicted by MCT Rule 07 is also shown.

The devices from wafer R100 have exhibit an unusual temperature-dependence of $(R_oA)^{-1}$ at both low and high temperatures. For the temperature range of 140 K – 200 K, the data is well fit using a value of E_a~150-160 meV, which is near the fitted high temperature E_a for the other 4

wafers. At lower temperatures, a relatively temperature-insensitive dark current is observed. This high dark current at low temperature was observed in all the devices processed from this wafer. A temperature-insensitive dark current is also observed at high temperatures. This can be seen in the roll-over in $(R_oA)^{-1}$ for temperatures above ~250 K. A similar roll-over can be seen in the data from the other single-stage sample, R100, but only for temperatures above ~300 K. This observation for the single-stage samples is likely due to drop in diffusion length at high temperature, which in addition to limiting the photocurrent, will also limit the amount of thermally generated carriers that can be extracted. These combined factors of unusual temperature-dependent $(R_oA)^{-1}$ behavior and a deviation in the zero-temperature bandgap lead us to conclude that wafer R100 had a lower overall material quality than the other wafers.

For device R102, separate activation energies were used to fit the high-temperature and low-temperature data. The high-temperature value of E_a was similar to, but slightly smaller than the fitted E_a for samples R101, R103, and R104. Although there is some deviation, we believe the values are consistent enough to indicate that the high-temperature dark current mechanisms in the devices from R102 are the same as those for the longer-absorber detectors. At lower temperatures, the magnitude of the dark current decreases at a slower rate as the temperature is lowered. A roll-over in $(R_oA)^{-1}$, similar that that observed for devices E2 and F2 from R103 in Fig. 5.3, and the device from R100 in Fig. 5.5, can be seen for the R102 device at low temperatures. In devices E2 and F2, it was suspected the roll-over in $(R_oA)^{-1}$ was caused by some local imperfections in the fabrication quality, since there were other devices from that sample (such as B2) that showed temperature-dependence consistent with that at high temperature. However, like wafer R100, a roll-over in $(R_oA)^{-1}$ was observed for all the devices from wafer R102. In R100, this was believed to be due to a lower overall material quality.

However, unlike wafer R100, there is no other indication that wafer R102 has a lower material quality than R101, R103, or R104. In fact, the weak temperature-dependence of R_oA may be due to the connected to the multiple-stage, short-absorber design of that structure. Similar behavior at low temperature has been observed in devices from other structures with similar designs. This trend can be seen in the data presented in Appendix C. This Appendix summarizes the temperature-dependence of R_oA for all the MWIR ICIPs studied in this dissertation, along with those whose performance results were reported in Refs. 12-14. Most of the early ICIPs utilized seven-stage designs with relatively short (150-250 nm) absorbers. As seen, all these devices from wafers EB2700, EB2702, EB3337, IQE11A, IQE12A, and IQE13A all show a strong roll-over in $(R_oA)^{-1}$ at low temperature.

It is not currently clear whether this is caused by the multiple-stage nature of the device or by the fact that fairly short absorbers are used. The mitigation of this leakage current at low temperature could be an important topic in the development of high-speed ICIPs, which may need to be cooled in order to reach the sensitivities needed for certain applications.

5.3.2 Photocurrent and Response Spectra

The calibrated external quantum efficiency (EQE) and nominal spectral particle conversion efficiency of detectors from samples R101, R102, and R104 are shown in Fig. 5.6 for both 78 K and 300 K. These measurements were done at zero bias. Recall that the particle conversion efficiency of a detector corresponds to the EQE multiplied by the number of stages, since that number of absorbed photons is required in order to generate a full electron charge of signal in the external circuit. We refer to the curve in Fig 5.6 as the "nominal" spectral particle conversion efficiency, since we assume that there is no internal gain in the device. Note that for single-absorber detectors the particle conversion efficiency is equal to the EQE.

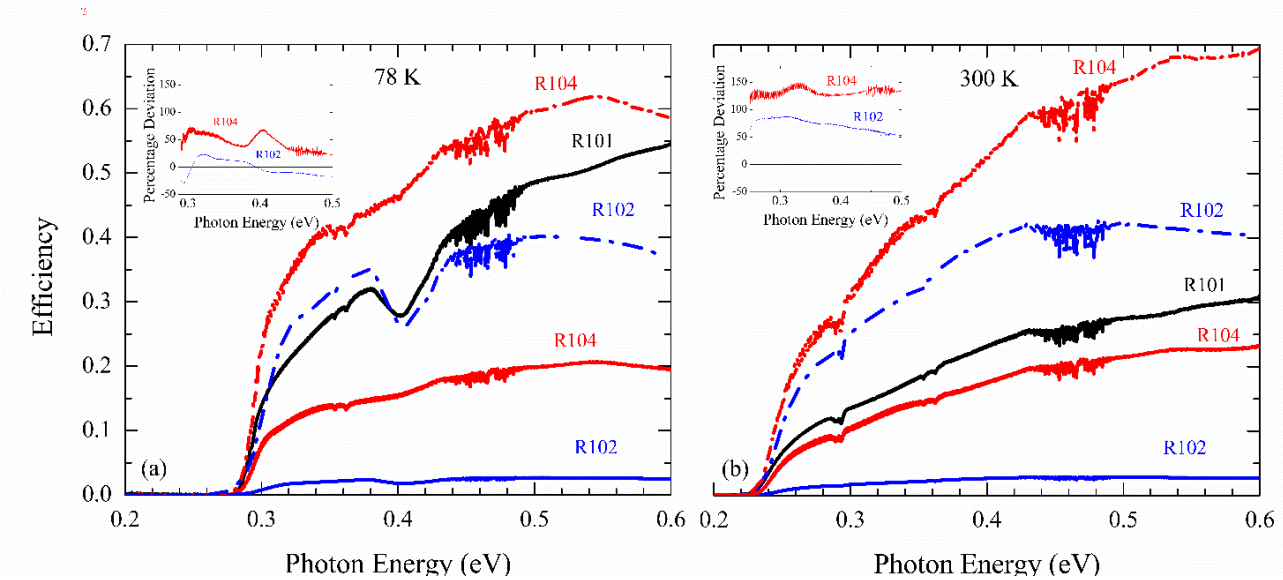

Figure 5.6: External quantum efficiency (solid line) and nominal particle conversion efficiency (dashed lines) of devices from samples R101, R104, and R102. The inset shows the deviation of particle conversion efficiency of the multiple-stage samples (R104 and R102).

In the limit where the diffusion length is long compared to the absorber thicknesses, we expect that the R101 device will have the highest particle conversion efficiency, followed by R104, and then R102. When the diffusion length is long compared to the absorber thickness, all electrons excited in the absorber will be converted to photocurrent. In this limit, the multiple-stage architecture is actually less efficient at using the incident photons, because of the requirement of current continuity across the device. The device from R104 can only match the particle efficiency of R101 if the photocurrent-matching between the three stages is perfect, which is not the case. The signal generated in sample R102 is limited by the photo-generation rate in the optically deepest stage, which leads a fairly weak overall signal. Gain in the multiple-stage samples can lead to a higher photo-response (but not necessarily a higher sensitivity since this will also compromise the noise reduction capability of multiple-stage devices).

The deviations of the nominal particle efficiencies of the multiple-stage devices from those of the single-stage device are shown in the Fig 5.6 insets. At 78 K, it is seen that while

R101 has the largest EQE, its nominal conversion efficiency is about 60% lower that of the device from R104, and also less than that of R102 at photon energies less than 0.39 eV. Thus, we tentatively conclude that there is some gain in the multiple-stage structures.

Interestingly, the quantum efficiency of the devices from wafer R102 tends to roll-over at shorter wavelengths, while the values for sample R101 and R104 continue to increase. This may be due to current-mismatching of the photocurrent generated by high-energy photons, which are more strongly absorbed.

5.3 Detectivity and Photocurrent

To evaluate the sensitivity, we utilize the convention of measuring the D* for a detector illuminated by a blackbody set to a temperature of 500 K [128]. For a detector at zero-bias illuminated by a source with power P_{inc} the detectivity, D^*, is given as:

$$D^* = \frac{I_{ph}}{P_{inc}} \sqrt{\frac{R_o A}{4 k_b T}}, \tag{5.1}$$

where I_{ph} is the photocurrent that flows under the given incident power. The D^* values for illumination by a 500 K blackbody source were obtained from the calibrated EQE spectra and the measured values of R_oA using Eq. 5.1.

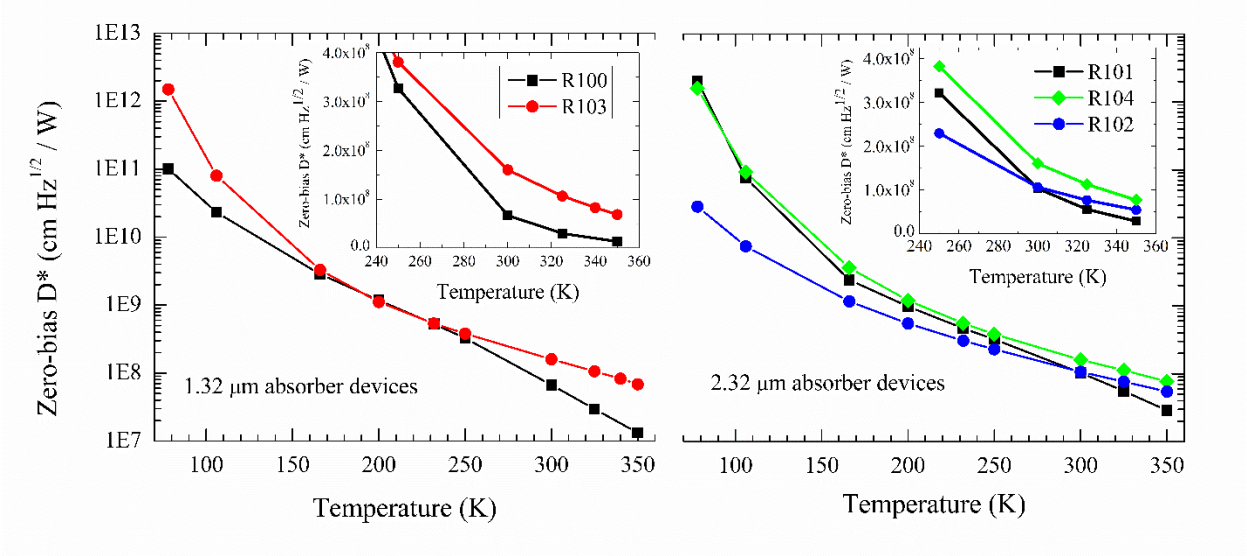

Figure 5.7: Temperature-dependent zero-bias detectivity measured under a 500 K blackbody is shown in (a) for the samples that had a total absorption thickness of 1.32 μm and in (b) for the samples that had a total absorption thickness of 2.32 μm. The insets of (a) and (b) compare the detectivity values of the 1.32-μm absorber and the 2.32-μm absorber devices at high temperature on a linear scale for detecitivity.

The temperature-dependence of *D** for each of the devices is shown in Fig. 5.7. In the figure, the temperature-dependence of detectors with the same overall absorber lengths are directly compared. As predicted, the shorter absorbers in the multiple-stage devices enable them to have a sensitivity that is much less sensitive to temperature than the single-stage devices. For wafers R100 and R103, which have an absorber thickness of 1.32 μm, the multiple-stage device achieves higher *D** values at both low and high temperature. We believe the reason that R103 has a better *D** than R100 at low temperature is the material quality difference between the two wafers, as detailed in the above discussion. The *D** values of the two are quite similar in the temperature range of 160 K – 230 K, which is notably the temperature range where R100 has a dark current temperature-dependence that is consistent with the other four wafers. At temperatures above 250 K, the sensitivities of the two devices diverge, with R100 showing a stronger decrease in *D** as the temperature increases.

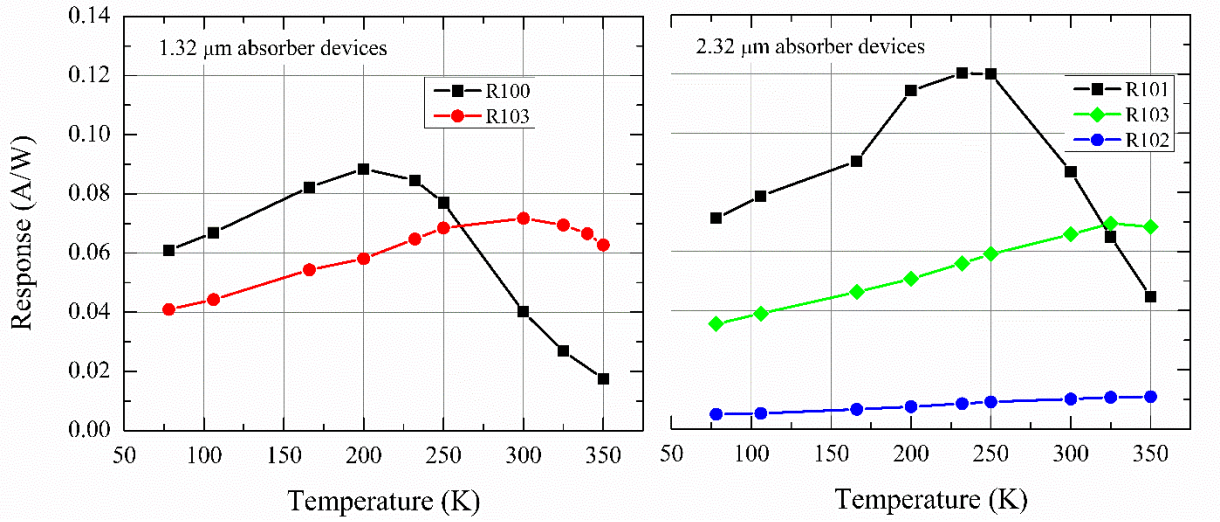

Figure 5.8: Temperature-dependent response (photocurrent divided by incident power) of MWIR ICIPs under a 500 K blackbody is shown in (a) for samples that had a total absorber thickness of 1.32 and in (b) for samples that had a total absorption thickness. Note that response is the photocurrent that flows in the device divided by the incident power.

The advantages offered by the multiple-stage architecture can be more clearly seen by comparing the temperature-dependence of the photocurrent. Fig. 5.8 shows the temperature-dependence of the detector response under a 500 K blackbody, which is the photocurrent that flows under that illumination divided by the incident power. For both samples R100 and R101, an increase in the photocurrent is observed at low temperatures, and after peaking shows a sharp decrease at high device temperatures. For R100, the decrease in photocurrent begins around 200 K, while for R101 it begins around 250 K. This is consistent with the earlier observation of the high temperature $(R_oA)^{-1}$ roll-over occurring at a lower temperature for R100 than R101. The devices from samples R103 and R104 show a monotonic increase in photocurrent with temperature up to about 325 K until the signal begins to drop. The devices from sample R102 show a constant rise in signal with increasing temperature, which is expected for devices with such short absorber lengths.

5.4 LWIR Interband Cascade

We believe that the multiple-stage approach may be even more advantageous for improving the sensitivity of detectors at longer wavelengths. Generally, for InAs/GaSb SLs, both the near-cutoff absorption coefficient and carrier lifetime will become smaller as the bandgap is made narrower. In particular, detectors with cutoff wavelengths in the LWIR atmospheric transmission window of 8-12 μm are of great technological interest.

Recently, we grew and fabricated photocurrent-matched two-stage and three-stage ICIPs with cutoff wavelengths near ~12.0 μm. The overall design structure of these detectors was similar that of our MWIR ICIP structures. The absorbers consisted of InAs/GaSb type-II SL material. The thickness of a single SL period in the absorber was about 66 Å. The InAs layer was designed to be ~40.3 Å and the GaSb layer was designed to be ~25.7 Å. As with the MWIR samples, an InSb interface was forced at the GaSb-on-InAs interface in order to provide strain compensation. The first two absorbers in both structures were composed of SLs with 86 and 96 periods respectively. These choices correspond to absorber thicknesses of 568 nm and 634 nm in the first two stages. The third absorber in the three-stage sample was composed of a SL with 112 periods, corresponding to a thickness of 739 nm.

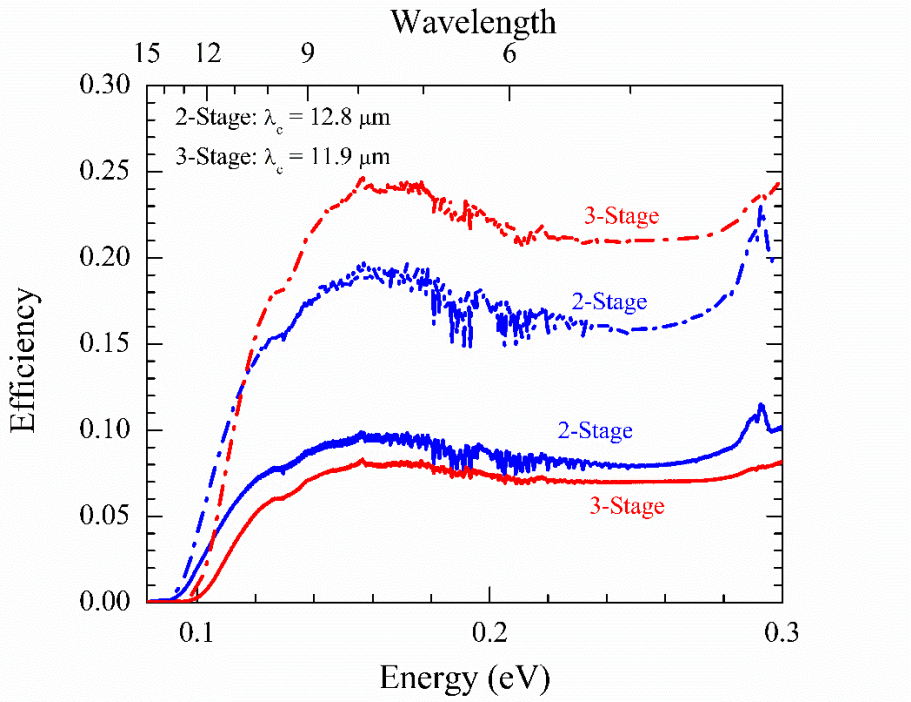

Figure 5.9: External quantum efficiency (solid line) and particle conversion efficiencies (dashed line) for 2-stage and 3-stage LWIR ICIPs

The EQE and particle conversion efficiency curves for zero-bias operation are shown in Fig. 5.9. As seen, the detectors are able to achieve a fairly good photoresponse at zero bias. This confirms that photovoltaic ICIPs with LWIR cutoffs can be achieved using the same basic stage design as has been used for the MWIR detectors. Since the absorber thicknesses of the two structures are the same, the two devices should have roughly the same EQE if the current-matching between stages was perfect. However, as seen, the two-stage device has a higher EQE value across the spectral range, indicating some current mismatching. The particle conversion efficiency was higher for the three-stage device though since it had a larger overall absorption thickness. The cutoff wavelengths between the two wafers are slightly different, despite the fact they were designed to have the same SL period. In addition, the observed R_oA values were low. This indicates some inconsistencies in the material growth process. This is also apparent from Nomarski microscopy analysis, which shows about an order of magnitude higher defect density

for the LWIR detector structures than the MWIR ICIPs. Thus, further optimization of the material is needed for improving the performance of LWIR ICIPs. It should be noted that the LWIR detectors were grown prior to the MWIR detectors described earlier, which indicates some improvement in the growth process.

Chapter 6 : Conclusions and Future Work

6.1 Dissertation Summary

The aim of this dissertation was to outline and demonstrate the advantages that photovoltaic devices based on interband cascade structures offer as an alternative to conventional single-absorber devices. Interband cascade photovoltaic devices are unique because of their multiple-stage nature. This sort of design is made possible by the type-II broken-gap alignment between InAs and GaSb. This alignment enables electrons to transition between the valence band of GaSb and the conduction band of InAs via elastic or low-energy inelastic scattering processes. In a multiple-stage structure, this creates a window through which electrons can pass from the absorber conduction band of one stage to the absorber valence band in the next stage. Thus, transport in these devices arises from a series of interband excitation and collection events, and several photons are required for an electron to traverse between the device contacts.

For photovoltaic devices, the multiple-stage design is useful because it allows the use of short absorbers. This ensures that excited photocarriers are collected before they recombine. The recombination of excited photocarriers is a well-known problem for narrow-bandgap semiconductor devices operating at high temperature. Another advantage of multiple-stage devices is that they have lower operating currents. In energy-conversion devices, this trade of lower current for higher voltage leads to less power dissipation across the contact resistance. In photodetectors, the lower operating current and higher device resistance reduces noise from parasitic sources such as the pre-amplifier.

In Chapter 3, we presented theory aimed at evaluating the carrier transport and noise in multiple-stage interband infrared detectors. The model follows from the picture that transport in the detector arises from the exchange of electrons between groups of thermalized states within

the device. In this picture, it is simple to evaluate the electronic noise, which arises from the stochastic variation of these exchanges. This approach highlights the inherent design tradeoff between the signal and thermal noise. For instance, in the case of bulk-like absorbers, both the photocurrent and thermal currents can be calculated from their respective generation rates using a Green's function, which is related to the design and material properties of the absorber.

The developed theory is general for multiple-stage photovoltaic devices. Here it was applied to identify the situations where the multiple-stage approach can be superior to single-absorber detectors. We considered the ultimate thermal-noise performance limit set by the diffusion-limited transport where the electric fields in each stage are confined to the barrier regions. We first investigated detectors optimized for high speed, with $d << 1/\alpha$ and $d << L_n$. For detectors in this limit, we derived an optimal number of stages in terms of α and d. This result suggests that the use of multiple-stages provides a means for achieving high-speed detectors without sacrificing as much sensitivity as would be required for a single-absorber device to achieve a similar response time. For applications where high speed is less important than sensitivity, the multiple-stage approach also provides a means for improving the performance by enhancing the carrier collection efficiency. Most notably, the ultimate performance limit of detectors operated at zero-bias is higher for multiple-stage devices, provided the absorbers are correctly designed to achieve an equal amount of absorbed and collected carriers in each stage. Our analysis of the potential improvement in detectivity of optimized detectors showed the multiple-stage approach should be beneficial (i.e. detectivity improvement of 1.5 or higher) when αL is < 0.2 for equal-absorber devices and when $\alpha L < 0.5$ for photocurrent-matched devices. It was also shown that photocurrent-matched detectors can improve the detector sensitivity in the strong-signal limit by enhancing the particle conversion efficiency.

In Chapter 4 we discussed the design and experimental characterization of a series of IC PV devices designed for radiative energy conversion. We examined devices utilizing InAs/GaSb superlattice (SL) absorbers and others using wider-bandgap InAs/$Al_{0.8}In_{0.2}Sb$/GaSb/$Al_{0.8}In_{0.2}Sb$ SLs. The thin layer of $Al_{0.8}In_{0.2}Sb$ enabled the latter devices to achieve a wider absorber bandgap. There were two wider-bandgap structures examined. One structure had two stages and the other had three stages. In both designs the absorber thicknesses were varied across the structure in order to achieve a rough matching of the photo-collection current in each stage. It was shown that at comparable laser powers, the wider-bandgap devices were able to achieve a better power conversion efficiency. The three-stage device had a higher efficiency than the two-stage due to a higher open-circuit voltage. However, for both sets of devices, the power conversion efficiency is found to be limited by a low fill factor. A variable-area analysis of a series of the wider-bandgap devices revealed the devices suffered from significant surface shunting effects. The shunting was also shown to limit the open-circuit voltage.

Chapter 5 presented an experimental study of the temperature-dependent performance of a set of MWIR interband cascade infrared photodetectors that utilized InAs/GaSb SL absorbers. In this study, we were primarily interested in how the photocurrent and the zero-bias detectivity varied with temperature for devices with different numbers of stages and absorber thicknesses. We found that the short-absorber devices had a photo-response that was less sensitive to temperature, and as a result were able to achieve better D^* values above 250 K than the single-stage devices. This verifies predictions that the photoresponse in short-absorber, multiple-stage devices would be less sensitive to increasing device temperature, and would have the potential to achieve higher sensitivities due to their inherently lower noise. This result shows that the multiple-stage architecture can produce sensitivity improvements for infrared detectors operating

at high temperature. To the author's knowledge, this is the first comparative study of single- and multiple-stage infrared detectors for which the main design features such as absorber material composition and barrier design were kept roughly the same. One unexpected factor in this study was the observation of high temperature activation energies close to half the extrapolated zero-temperature bandgap for devices from most of the samples.

6.2 Future Work

This section will address the broad challenges faced in the development of PV devices targeted for the conversion of mid-infrared radiation and also those issues more specific to interband cascade structures. First, I will address some of the more extrinsic challenges that are currently faced in the material growth and fabrication process. As discussed in this work, PV devices designed to efficiently convert mid-infrared radiation to electricity must be fairly thick in order to absorb most of the incident light. For devices using SL absorbers this implies that the epitaxial heterostructure will consist of many (> 1000) layers. When these sort of heterostructures are grown very thick, it becomes more challenging to maintain strain balancing, even with the close lattice-matching of InAs, GaSb, and AlSb. To the author's knowledge, the thickest absorber for a detector based on InAs/GaSb SL was 6 μm, and was grown by Northwestern University [129]. This device had a cutoff wavelength of ~12 μm at 77 K. Absorbers even thicker than this may be needed to achieve high quantum efficiencies, especially for LWIR detectors. For multiple-stage structures, the growth optimization may be more challenging, due to the extra barrier layers.

A second extrinsic challenge is to mitigate the surface effects that were observed in the energy-conversion devices presented in Chapter 4. These issues will most likely be encountered in ICIP fabrication as well. For conventional, deep-etched devices, this would involve

experimenting with different dielectric materials and deposition conditions. An alternative to the conventional passivation method of dielectric deposition is to utilize the self-passivation approach discussed in the introduction. Applied to IC PV devices, this method would utilize the wide-bandgap electron or hole barrier at the top of structure for passivation. Whether the electron or hole barrier is used would depend on the preferred illumination condition. With this approach, only the top contact layer would be etched. This is attractive for FPA applications, due to the fact that thicker structures are more difficult to etch and clean, especially when the device dimensions are as small as those needed for an FPA [10]. However, doing this with a multiple-stage SL-absorber device would more challenging due to the need to account for the effects of current-spreading, especially if one wants to achieve a photocurrent-matched device. The photocurrent-matching process in the design would need to account for both the lateral and vertical transport properties.

A third issue that must be resolved is the choice and optimization of the absorber material. The devices presented in this work used InAs/GaSb and $InAs/Al_{0.8}In_{0.2}Sb/GaSb/Al_{0.8}In_{0.2}Sb$ SL absorbers. As stated in Chapter 1, the InAs/GaSb SL is considered a promising material for mid-infrared PV devices. It was also noted that the defect-assisted interband transition time has been found to be unexpectedly short. Although this may also be considered an extrinsic problem, this short lifetime has been observed by multiple groups using material grown by different machines. Thus, resolving this issue will likely require more than some tweaks to the MBE growth steps. A series of time-resolved material studies have established a loose consensus that the short lifetime of InAs/GaSb SLs is related to the presence of Ga in the material [21-24]. There is also evidence that the lifetime is not caused by the SL nature of the material, as the lifetime has been found to be insensitive to the number of interfaces

[130]. However, there has not been any indication yet as to whether the defect issue can be mitigated. Thus, the fundamental material optimization of InAs/GaSb SLs is an area that requires further research.

The InAs/Ga(In)Sb SL is a natural absorber material for interband cascade PV devices. However, the use of other absorber materials is possible if they have the proper band alignment with the electron and hole barriers and can be lattice-matched to either a GaSb or InAs substrate. The alignment of the absorber with the hole barrier should be type-II with the absorber valence band edge falling in the bandgap of hole barrier. This means the absorber valence band edge should fall either within or slightly above the bandgap of InAs. The alignment of the absorber with the electron barrier should also be type-II. However, in this case the conduction band edge should fall within the bandgap of the electron barrier. This is the case if it falls in the bandgap of GaSb. If these conditions are met, an interband cascade type structure can be realized with an alternative absorber material. One alternative that may be possible is the Ga-free InAs/InAsSb SLs. This material has been demonstrated to have a longer non-radiative interband lifetime than InAs/GaSb SLs [23,24]. The disadvantage to this material it also has a fairly low mobility and absorption coefficient. However, a material with a long interband lifetime, but low mobility and absorption coefficient is the exact sort of material that can be improved with the multiple-stage design. The alignment of the valence band of an InAs/InAsSb SL and the hole barrier will be fairly small. This means that a grading of the electron barrier quantum wells, rather than the hole barrier quantum wells, should be used to relax the excited carriers to the next stage. This may lead to a higher inter-stage resistance because of the slow hole transition process.

There are many potential directions for the future development of IC PV energy-conversion devices. One reason for this is the immense versatility of the PV approach for

energy-conversion. The development of cells for non-solar applications is still very immature. Research into improving the source and spectral shaping technology is also ongoing. The progress in this ongoing work may change the parameters required for the optimum PV cell. For example, a reasonable next step in interband cascade PV research may seem to be to utilize absorbers with different bandgaps in order to achieve spectral splitting. This would only be useful if the radiation converted by the cell has a broadband distribution. The development of a good selective emitter that is able to convert the radiation emitted from a broadband source to a narrow spectral band would make the spectral splitting approach unnecessary. Since there are already many inherent losses in a TPV system, this may be the most promising path towards an efficient system for converting terrestrial radiation. Because of the uncertainties in the future development of TPV sources and spectral shaping technology, my recommendation for future work on interband cascade PV energy converters would be to concentrate on research that demonstrates some of the fundamental advantages the multiple-stage approach has over a converter cell that only has a single absorber.

One almost certain requirement for all potential IC PV energy-conversion applications is that the cell will need to be able to efficiently convert a large photon flux to electrical power. As stated earlier, in narrow-bandgap PV devices, this is problematic for single-absorber devices due to the large series resistance losses associated with the high current. The multiple-stage approach provides the means for mitigating this loss by trading a lower current for higher voltage without sacrificing the power output of the cell. However, this advantage has not been definitively established in practice. Thus, one fairly straightforward but important experiment that could be conducted is a comparison of the conversion efficiency of single- and multiple-stage cells with similar designs as a function of incident power from the source. At low incident

powers the efficiency in both cells would be expected to increase with power due to the increase in open-circuit voltage. At higher incident powers, the behavior of the two cells would be different. The efficiency of the single-absorber cell would strongly decrease due to series resistance effects. The efficiency of the multiple-stage device would continue to increase or at least fall off less rapidly with increasing power due to the reduced loss to series resistance. Such a result would unambiguously demonstrate the advantage that multiple-stage devices have in mitigating series resistance losses.

Another possible direction for future research on interband cascade energy-conversion cells is the optimization of the structure doping for the conditions under which these cells will operate. In this work, the absorbers of the energy-conversion devices were doped in a manner similar to the detector structures. However, the physics of these devices is different because they will operate at room temperature and under forward bias. Thus, the absorber contains a large number of excess carriers. The carrier densities will be similar to, but (in an ideal world only slightly) less than those of an ICL or interband cascade LED at the transparency voltage. Since recombination in ICLs near threshold is known to be limited by Auger recombination, it would be expected that forward-biased interband cascade PV devices would also be dominated by Auger recombination, rather than Shockey-Read-Hall processes. If this is the case, the doping must be altered accordingly. In a study presented in Ref. 62, it was found that the optimal threshold condition for ICLs was one where the electron and hole densities were roughly equal. This corresponds to the condition where the cross-section for multi-electron and multi-hole processes are roughly equal. If this is the case, the incorporation of carrier rebalancing would lead to an increase in the open-circuit voltage by reducing the Auger recombination rate at a

given voltage. For this design, the multiple-stage architecture would be beneficial because the carrier extraction would be limited by the slow hole diffusion process.

The path forward for ICIPs is a bit clearer than for their energy-conversion counterparts. Many of the general issues discussed above such as growth improvement, passivation improvement, and absorber material optimization are important topics for future ICIP research. In particular, high-quality growth of thick structures will be required for realizing better ICIPs with cutoff wavelengths in the LWIR and VLWIR regions of the spectrum. The potential for improvement with the use of multiple-stages is expected to be even better than in the MWIR region, due to the lower absorption coefficient and diffusion length.

As discussed in this dissertation, the ICIP concept is most promising for achieving semiconductor infrared detectors with better high temperature performance and for achieving better high speed detectors. One outstanding issue from this dissertation is the question of why the low-temperature activation energies appear to be inherently lower for the multiple-stage, short absorber devices. This could be a relevant question for high-speed ICIPs, since these detectors would conceivably use many stages with very short absorbers. In addition, they may need to be cooled to reach the sensitivities required for certain applications. Eliminating the leakage source that is causing the dark current to be less sensitive to temperature would potentially lower the cooling requirements for these detectors.

Another important topic for future ICIP research is the study of the high temperature physics in InAs/GaSb SL detectors. Most of the fundamental material studies have concentrated on studying the low-temperature recombination and transport properties. The physics of semiconductor devices is often fundamentally different at low and high temperature. As seen in this work, the performance at low temperature is often limited by extrinsic factors such as the

presence of defects or the fabrication quality. The high temperature performance is more likely to be governed by the intrinsic properties of the absorber material. One key issue that remains unresolved is why the minority carrier diffusion length of mid-infrared absorber materials drops at high temperature. This could be caused by either a drop in the non-radiative lifetime, or a drop in the effective diffusion coefficient. The latter effect is possible if the slow dynamics of the valence band carriers in the absorber play a limiting role in the high-temperature transport. This would be expected if the rising temperature makes the material more intrinsic. When this high-temperature device physics is better understood, the degree to which the multiple-stage approach can be beneficial can be better quantified for detectors using specific absorber materials.

References

[1] A. Rogalski, "Infrared detectors: an overview," Infrared Phys. Tech. **43**, 187-210 (2002).

[2] A. Rogalski, "Infrared detectors: status and trends," Prog. Quantum Electron. **27**, 59-210 (2003).

[3] D. Wilt, D. Chubb, D. Wolford, P. Magari, and C. Crowley, "Thermophotovoltaics for Space Power Applications," in *Proc. 7th Conf. Thermophotovoltaic Gener. Elect.*, 335-345 (2007).

[4] T. Bauer, *Thermophotovoltaics: Basic Principles and Critical Aspects of System Design*. Berlin, Germany: Springer, 2011.

[5] P. Würfel, "Solar energy conversion with hot electrons from impact ionization," Sol. Energy Mater. Sol. Cells **46**, 43-52 (1997).

[6] A.S. Gilmore, J. Bangs, and A. Gerrish, "VLWIR HgCdTe detector current-voltage analysis," J. Electron. Mater. **35**, 1403-1410 (2006).

[7] Q.K. Yang, F. Fuchs, J. Schmitz, and W. Pletschen, "Investigation of trap-assisted tunneling current in InAs/(GaIn)Sb superlattice long-wavelength photodiodes," Appl. Phys. Lett. **81**, 4757-4749 (2002).

[8] J.V. Li, R.Q. Yang, C.J. Hill, and S.L. Chuang, "Interband cascade detectors with room temperature photovoltaic operation," Appl. Phys. Lett. **86**, 101102 (2005).

[9] D.Z.-Y Ting, C.J. Hill, A. Soiblel, S.A. Keo, J.M. Mumolo, J. Nguyen, and S.D. Gunapala "A high-performance long wavelength superlattice complementary barrier infrared detector," Appl. Phys. Lett. **95**, 023508 (2009).

[10] B.-M. Nguyen, D. Hoffman, P.-Y. Delaunay, and M. Razeghi, “Dark current suppression in type II InAs/GaSb superlattice long wavelength infrared photodiodes with M-structure barrier,” Appl. Phys. Lett. **91**, 163511 (2007).

[11] I. Vurgaftman, C.L. Canedy, E.M. Jackson, J.A. Nolde, C.A. Affouda, E.H. Aifer, J.R. Meyer, A. Hood, A.J. Evans, and W.T. Tennant, “Analysis and performance of type-II superlattice infrared detectors,” Opt Eng. **50**, 061007 (2011).

[12] R.Q. Yang, Z. Tian, Z. Cai, J.F. Klem, M.B. Johnson, and H.C. Liu, “Interband-cascade infrared photodetectors with superlattice absorbers,” J. Appl. Phys. **107**, 054514 (2010).

[13] R.Q. Yang, Z. Tian., J.F. Klem, T.D. Mishima, M.B. Santos, and M.B. Johnson, “Interband cascade photovoltaic devices,” Appl. Phys. Lett. **96**, 063504 (2010).

[14] Z. Tian, R. T. Hinkey, R. Q. Yang, D. Lubyshev, Y. Qiu, J. M. Fastenau, W. K. Liu, and M. B. Johnson, “Interband cascade infrared photodetectors with enhanced electron barriers and p-type superlattice absorbers,” J. Appl. Phys. **111**, 024510 (2012).

[15] I. Vurgaftman, J.R. Meyer, and L.R. Ram-Mohan, “Band parameters for III-V compound semiconductors and their alloys,” J. Appl. Phys. **89**, 5815-5875 (2001).

[16] D. L. Smith and C. Mailhiot, “Proposal for strained type II superlattice infrared detectors,” J. Appl. Phys. **62**, 2545-2458 (1987).

[17] C.H. Grein, P.M. Young, and H. Ehrenreich, “Minority carrier lifetimes in ideal InGaSb/InAas superlattices,” Appl. Phys. Lett. **61**, 2905-2907 (1992).

[18] E. R. Youngdale, J. R. Meyer, C. A. Hoffman, F. J. Bartoli, C. H. Grein, P. M.Young, H. Ehrenreich, R. H. Miles, and D. H. Chow, "Auger lifetime enhancement in InAs—$Ga_{1-x}In_xSb$ superlattices," Appl. Phys. Lett. **64**, 3160-3162 (1994).

[19] D. Donetsky, S.P. Svensson, L.E. Vorobjev, and G. Belenky, "Carrier lifetime measurements in short-period InAs/GaSb strained-layer superlattice structures," Appl. Phys. Lett. **95**, 212104 (2009).

[20] D. Donetsky, G. Belenky, S. Svensson, and S. Suchalkin, "Minority carrier lifetime in type-II InAs-GaSb strained-layer superlattices and bulk HgCdTe materials," Appl. Phys. Lett. **97**, 052108 (2010).

[21] B. C. Connelly, G. D. Metcalfe, H. Shen, and M.Wraback, "Direct minority carrier lifetime measurements and recombination mechanisms in long-wave infrared type II superlattices using time-resolved photoluminescence," Appl. Phys. Lett. **97**, 251117 (2010).

[22] B.C. Connelly, G.D. Metcalfe, H. Shen, M. Wraback, C.L. Canedy, I. Vurgaftman, J.S. Melinger, C.A. Affouda, E.M. Jackson, J.A. Nolde, J.R. Meyer, and E.H. Aifer, "Investigation of trap states in mid-wavelength infrared type II superlattices using time-resolved photoluminescence," J. Electron. Mater. **42**, 3203-3210 (2013).

[23] E.H. Steenbergen, B.C. Connelly, G.D. Metcalfe, H. Shen, M. Wrabeck, D. Lubyshev, Y. Qiu, J.M. Fastenau, A.W.K. Liu, S. Elhamri, O.O. Cellek, and Y.-H. Zhang, "Significantly improved minority carrier lifetime observed in a long-wavelength infrared III-V superlattice comprised of InAs/InAsSb," Appl. Phys. Lett. **99**, 251110 (2011).

[24] B. V. Olson, E. A. Shaner, J. K. Kim, J. F. Klem, S. D. Hawkins, L. M. Murray, J. P. Prineas, M. E. Flatté, and T. F. Boggess, "Time-resolved optical measurements of minority carrier recombination in a mid-wave infrared InAsSb alloy and InAs/InAsSb superlattice," Appl. Phys. Lett. **101**, 092109 (2012).

[25] T. Schuler-Sandy, S. Myers, B. Klein, N. Gautum, P. Ahirwar, Z.-B. Tian, T. Rotter, G. Balakrishnan, E. Plis, and S. Krishna, "Gallium-free type II InAs/InAsSb superlattice photodetectors," Appl. Phys. Lett. **101**, 071111 (2012).

[26] H. S. Kim, O. O. Cellek, Z.-Y. Lin, Z.-Y. He, X.-H. Zhao, S. Liu, H. Li, and Y.-H. Zhang, "Long-wavelength infrared nBn photodetectors based on InAs/InAsSb type-II superlattices," Appl. Phys. Lett. **101**, 161114 (2012).

[27] H.C. Liu and H. Schneider, *Quantum Well Infrared Photodetectors* (Springer, Berlin 2005).

[28] L. Gendron, M. Carras, A. Huynh, V. Ortiz, C. Koeniguer, and V. Berger, "Quantum cascade photodetector," Appl. Phys. Lett. **85**, 2824-2826 (2004).

[29] H.C. Liu, R. Dudek, A. Shen, E. Dupont, C.Y. Song, Z.R. Waseilewski, and M. Buchanan, "High absorption (> 90%) quantum-well infrared photodetectors," Appl. Phys. Lett. **79**, 4237-4239 (2001).

[30] W. Shockley and W.T. Read, "Statistics of the Recombination of Holes and Electrons," Phys. Rev. **87**, 835-842 (1952).

[31] B. Laikhtman, "Trapping of free electrons in III-V superlattices," J. Appl. Phys. **112**, 093111 (2012).

[32] C.T. Sah, R.N. Noyce, and W. Shockley, "Carrier generation and recombination in pn junctions and pn junction characteristics," Proc. IRE **45**, 1228-1243 (1957).

[33] S. Maimon and G. W. Wicks, "nBn detector, an infrared detector with reduced dark current and higher operating temperature," Appl. Phys. Lett., **89**, 151109 (2006).

[34] P. Klipstein, "Depletionless photodiode with suppressed dark current and method for producing the same," Int. Patent No. WO/2005/004243.

[35] P. Klipstein, O. Klin, S. Grossman, N. Snapi, I. Lukomsky, M. Yassen, D. Aronov, E. Berkowitz, A. Glozman, O. Magen, I. Shtrichman, R. Frenkel, and E. Weiss, "High operating temperature XB*n*-InAsSb *bariode* detectors," Proc. SPIE **8268**, 82680U (2012).

[36] B.-M. Nguyen, "Theoretical design and material growth of type-II antimonide-based superlattices for infrared detection and imaging," Ph.D dissertation, Northwestern University (2010).

[37] J.W. Scott, C.E. Jones, E.J. Caine, and C.A. Cockrum, "Sub-pixel nBn detector," US Patent No. 8,044,435 B2.

[38] P.-Y. Delaunay, A. Hood, B.M. Nguyen, D. Hoffman, Y. Wei, and M.Razeghi, "Passivation of type-II InAs/GaSb double heterostructure ," Appl. Phys. Lett. **91**, 091112 (2007).

[39] E.H. Aifer, J.H. Warner, R.R. Stine, I. Vurgaftman, C.L. Canedy, E.M. Jackson, J.G. Tischler, J.R. Meyer, D.Y. Petrovykh, and L.J. Whitman, "Passivation of W-structured type-II superlattice long-wave infrared photodiodes," Proc SPIE, **6542**, 654203 (2007).

[40] T. Ashley and C.T. Elliott, "Non-equilibrium devices for infrared detection," Electron. Lett. **21**, 451-452 (1985).

[41] T. Ashley, C.T. Elliott, and A.T. Harker, "Non-equilibrium modes of operation for infrared detectors," Infrared Phys. **26**, 303-3015 (1986).

[42] A.M. White, "Auger suppression and negative resistance in low gap PIN diode structures," Infrared Phys. **26**, 317-324 (1986).

[43] T. Ashley, C.T. Elliott, N.T. Gordon, R.S. Hall, A.D. Johnson, G.J. Pryce, "Negative luminescence from In1-xAlxSb and CdHgTe diodes," Inf. Phys. Tech. **36**, 1037-1044 (1995).

[44] T. Ashley, A.B. Dean, C.T. Elliott, C.F. McConvill, G.J. Pryce, and C.R. Whitehouse, "Ambient temperature diodes and field-effect transistors in InSb/InAlSb," Appl. Phys. Lett. **59**, 1761- (1991).

[45] P.Y. Emelie, J.D. Phillips, S. Velicu, "Parameter evaluation of HgCdTe infrared photodiodes exhibiting Auger suppression," J. Phys. D **42**, 234003 (2009).

[46] M. Mauk and V.M. Andreev, "GaSb-related materials for TPV cells," Semicond. Sci. Technol. **18**, S191-S201 (2003).

[47] B. Wernsman, R. Siergiej, S.D. Link, R.G. Mahorter, M.N. Palmisiano, R.J. Wehrer, R.W. Schultz, G.P. Schmuck, R.L. Messham, S. Murray, C.S. Murray, F. Newman, D. Taylor, D.M. DePoy, and T. Rahmlow, "Greater than 20% Radiant Heat Conversion Efficiency of a Thermophotovoltaic Radiator/Module System Using Reflective Spectral Control," IEEE Trans. Electron. Dev. **51**, 512-515 (2004).

[48] M.W. Dashiell, J.F. Beausang, H. Ehsani, G.J. Nichols, D.M. Depoy, L.R. Danielson, P. Talamo, K.D. Rahner, E.J. Brown, S.R. Burger, P.M. Fourspring, W.F. Topper Jr., P.F. Baldasaro, C.A. Wang, R.K. Huang, M.K. Connors, G.W. Turner, Z.A. Shellenbarger, G. Taylor, J. Li, R. Martinelli, D. Donetski, S. Anikeev, and G.L. Belenky, "Quaternary InGaAsSb Thermophotovoltaic Devices," IEEE Trans. Electron. Dev **53**, 2879-2891 (2006).

[49] X. Liu, T. Tyler, T. Starr, A. Starr, N.M. Jokerst, and W.J. Padilla, "Taming the blackbody with infrared metamaterials as selective thermal emitters," *Phys. Rev. Lett.* **107**, 045901 (2011).

[50] W. Streyer, S. Law, J. Mason, D.C. Adams, G. Rooney, T. Jacobs, and D. Wasserman, "Selective Thermal Emission from Thin-Film Metasurfaces," *Proc. SPIE* **8808**, 88080V (2013).

[51] W. Shockley and H. Queisser, "Detailed balance limit of efficiency of p-n junction solar cells," J. Appl. Phys. **32**, 510-519 (1961).

[52] T. J. Coutts and J.S. Ward, "Thermphotovoltaic and photovoltaic conversion at high-flux densities," IEEE Trans. Electron. Dev. **46**, 2145-2153 (1999).

[53] P. Würfel, "The chemical potential of radiation," J. Phys. C: Solid State Phys. **15**, 3967-3985 (1982).

[54] W.E. Tennant, D. Lee, M. Zandian, E. Piquette, and M. Carmody, "MBE HgCdTe technology: a very general solution to IR detection, described by "Rule 07," a very convenient heuristic," *J. Electron. Mater.* **37**, 1406-1410 (2008).

[55] R.S. Turley and R.J. Nicolas, "Band gap dependent thermophotovoltaic device performance using the InGaAs and InGaAsP material system," J. Appl. Phys. **108**, 084516 (2010).

[56] R.Q. Yang, "Infrared laser based on intersubband transitions in quantum wells," Superlattices Microstruct. **17**, 77- (1995).

[57] J. Faist, F. Capasso, D.L. Sivco, C. Sirtori, A.L Hutchinson, and A.Y. Cho, "Quantum cascade laser," Science **264**, 553-556 (1994).

[58] R.Q. Yang, L. Li, L. Zhao, Y. Jiang, Z. Tian, H. Ye, R.T. Hinkey, C. Niu, T.D. Mishima, M.B. Santos, J.C. Keay, Matthew B. Johnson, and K. Mansour, "Recent progress in development of InAs-based interband cascade lasers," Proc. SPIE **8640**, 86400Q (2013).

[59] R.Q. Yang, B.H. Yang, D. Zhang, C.-H. Lin, S.J. Murray, H. Wu, and S.S. Pei, "High power mid-infrared interband cascade lasers based on type-II quantum wells" Appl. Phys. Lett. **71**, 2409 (1997).

[60] J.C. Keay, L. Li, D.B. Brunski, et al, "Suppression of slip-line defect formation in GaSb substrates during thermal desorption of oxide layers," Poster session presented at: *28th North American Molecular Beam Epitaxy* (2011).

[61] J.R. Meyer, C.A. Hoffman, F.J. Bartoli, and L.R. Ram-Mohan, "Type-II quantum-well lasers for the mid-wavelength infrared," Appl. Phys. Lett. **67**, 757-759 (1995).

[62] I. Vurgaftman, W.W. Bewley, C.L. Canedy, C.S. Kim, M. Kim, C.D. Merritt, J. Abell, J.R. Lindle, and J.R. Meyer, "Rebalancing of internally generated carriers for mid-infrared interband cascade lasers with very low power consumption," Nat. Commun. **2**, 585 (2011).

[63] I Vurgaftman, W.W. Bewley, C.L. Canedy, C.S. Kim, M. Kim, C.D. Merritt, J. Abell, and J.R. Meyer, "Interband cascade lasers with very low threshold powers and high output powers," IEEE J. Selected Topics on Quantum Electron. **19**, 1200210 (2013).

[64] Z.-B. Tian, T. Schuler-Sandy, and S. Krishna, "Electron barrier study of mid-wave infrared interband cascade photodetectors," Appl. Phys. Lett. **103**, 083501 (2013).

[65] S. Bandara, P. Maloney, N. Baril, J. Pellegrino, and M. Tidrow, "Doping dependence of minority carrier lifetime in long-wave Sb-based type-II superlattice infrared detectors," Opt. Eng. **50**, 061015 (2011).

[66] N. Baril, C. Billman, P. Maloney, E. Nallon, M. Tidrow, J. Pellegrino, and S. Bandara, "Optimization of thickness and doping of heterojunction unipolar barrier layer for dark

current suppression in long wavelength strain layer superlattice infrared detectors," Appl. Phys. Lett. **102**, 013509 (2013).

[67] W.R. Chan, P. Bermel, R. C. N. Pilawa-Podgurski, C. H. Marton, K. F. Jensen, J. J. Senkevich, J. D. Joannopoulos, M. Soljačić, and I. Celanovic, "Toward high-energy-density, high-efficiency, and moderate-temperature chip-scale thermophotovoltaics," Proc. Natl. Acad. Sci. U.S.A. 110, 5309-5314 (2013).

[68] J. Piotrowski, P. Brozozowski, and K. Jóźwikowski, "Stacked multijunction photodetectors of long-wavelength radiation," *J. Electron. Mater.* **32**, 672-676 (2003).

[69] W. Schottky, "Über spontane Stromschwankungen in verschiedenen Elektrizitätsleitern (English Translation: About spontaneous current fluctuations in several electrical conductors)," Ann. Phys. **57**, 541-567 (1918).

[70] W.A. Beck, "Photoconductive gain and generation-recombination noise in multiple-quantum-well infrared photodetectors," Appl. Phys. Lett. **63**, 3589-3591 (1993).

[71] C. Schönbein, H. Schneider, R. Rehm, and M. Walther, "Noise gain and detectivity of n-type GaAs/AlAs/AlGaAs quantum well infrared photodetectors," Appl. Phys. Lett. **73**, 1251-1253 (1998).

[72] J.H. Davies, P. Hyldgaard, S. Hershfield, and J.W. Wilkins, "Classical theory for shot noise in resonant tunneling" Phys. Rev. B. **46**, 9620-9633 (1992).

[73] P.O. Lauritzen, "Noise due to generation and recombination of carriers in p-n junction Transition Regions," IEEE Trans. Electron. Dev. **15**, 770-776 (1968).

[74] I.A. Maione, B. Pellegrini, G. Fiori, M. Macucci, L. Guidi, and G. Basso, "Shot noise suppression in p-n junctions due to carrier generation-recombination," Phys. Rev. B. **83**, 155309 (2011).

[75] C.T. Elliott and A.M. White, “Multiple heterostructure photodetector,” Patent No. US 5,068,524.

[76] T. Ashley, personal communication (2012).

[77] A. Rogalski, personal communication (2013).

[78] J. Piotrowski and A. Rogalski, “Comment on: ‘Temperature limits on infrared detectivities of InAs/InGaSb superlattices and bulk HgCdTe,” J. Appl. Phys. **80**, 2542-2544 (1996).

[79] J. Piotrowski and W. Gawron, “Ultimate performance of infrared photodetectors and figure of merit of detector material,” Infrared Phys. Tech. **38**, 63-68 (1997).

[80] Y. Blanter and M Büttiker, “Shot noise in mesoscopic conductors,” Phys. Rep. **336**, 1-165 (2000).

[81] A. Delga, M. Carras, L Doyennette, V. Trinité, A. Nedelcu, and V. Berger, “Predictive circuit model for noise in quantum cascade detectors,” Appl. Phys. Lett. **99**, 252106 (2011).

[82] A. Delga, M. Carras, V. Trinité, V. Guériaux, L. Doyennette, A. Nedelcu, H. Schneider, and V. Berger, “Master equation approach of classical noise in intersubband detectors,” Phys Rev. B **85**, 245414 (2012).

[83] A. Delga, L. Doyennette, M. Carras, V. Trinité, and P. Bois, “Johnson and shot noise in intersubband detectors,” Appl. Phys. Lett. **102**, 163507 (2013).

[84] W. Shockley, “Currents to conductors induced by a moving point charge,” J. Appl. Phys. **9**, 635-626 (1938).

[85] S. Ramo, “Currents induced by electron motion,” Proc. IRE **27**, 584-585 (1939).

[86] B. Pellegrini, "Electron charge motion, induced charge, energy balance, and noise" Phys. Rev. B **34**, 5921-5924 (1986).

[87] R. Landauer, "Solid-state shot noise," Phys. Rev. B **47**, 16427-16432 (1993).

[88] T. Ashley and N.T. Gordon, "Higher operating temperature, high performance infrared focal plane arrays," Proc. SPIE **5359**, 89-100 (2004).

[89] V.M. Cowan, C. Morath, S. Myers, N. Gautam, and S. Krishna, "Low temperature noise measurement of an InAs/GaSb-based nBn MWIR detector," Proc. SPIE **8012**, 801210 (2011).

[90] R. Rehm, A. Wörl, and M. Walther, "Noise in InAs/GaSb type-II superlattice photodiodes," Proc. SPIE **8631**, 86311M-1 (2013).

[91] S. Tobin, S. Iwasa, and T. Tredwell, "1/f noise in (Hg, Cd)Te photodiodes," IEEE Trans. Electron. Dev. **27**, 43-48 (1980).

[92] R.Landauer, "Mesoscopic noise: Common sense view," Physica B **227**, 156-160 (1996).

[93] C. Koeniguer, G. Dubois, A. Gomez, and V. Berger, "Electronic transport in quantum cascade structures at equilibrium," Phys. Rev. B **74**, 235325 (2006).

[94] A. Buffaz, A. Gomez, M. Carras, L. Donyennette, and V. Berger, "Role of subband occupancy on electronic transport in quantum cascade detectors," Phys. Rev. B **81**, 075304 (2010).

[95] C. Donolato, "A reciprocity theorem for charge collection," Appl. Phys. Lett. **46**, 270-272 (1985).

[96] C. Donolato, "An alternative proof of the generalized reciprocity theorem for charge collection," J. Appl. Phys. **66**, 4524-4525 (1989).

[97] T. Markvart, "Relationship between dark carrier distribution and photogenerated carrier collection in solar cells," IEEE Trans. Electron. Devices **43**, 1034-1036 (1996).

[98] M.A. Green, "Generalized relationship between dark carrier distribution and photocarrier collection in solar cells," J. Appl. Phys. **81**, 268-271 (1997).

[99] M.A. Green, "Do built-in fields improve solar cell performance" Prog. Photovolt. Res. Appl. **17**, 57-66 (2009).

[100] J. Schwinger, L.L. Deraad, K.A. Milton, and W.-Y. Tsai, *Classical Electrodynamics*, (Westview Press, New York, 1998).

[101] M.B. Reine, A.K. Sood, and T.J. Tredwell, in *Semiconductors and Semimetals,* edited by R.K. Willardson and A.C. Beer (Academic, New York, 1981), Vol. 18, p. 201.

[102] B. Satpati, J.B. Rodriguez, A. Trampert, E. Tournié, A.Joullié, and P. Christol, "Interface analysis of InAs/GaSb superlattice grown by MBE," J. Crystal Growth **301/302**, 889-892 (2007).

[103] Y. Livneh, P.C. Klipstein, O. Klin, N. Snapi, S. Grossman, A. Glozman, and E. Weiss, "k•p model for the energy dispersions and absorption spectra of InAs/GaSb type-II superlattices," Phys. Rev. B **86**, 235311 (2012).).

[104] R. Rehm, M. Walther, J. Schmitz, F. Rutz, J. Fleiβner, R. Scheibner, J. Ziegler, "InAs/GaSb superlattices for advanced infrared focal plane arrays," Infrared Phys. Tech. **52**, 344 (2009).

[105] E.H. Aifer, J.G. Tischler, J.H. Warner, I. Vurgaftman, W.W. Bewley, J.R. Meyer, C.L. Canedy, and E.M. Jackson, "W-structured type-II superlattice long-wave infrared photodiodes with high quantum efficiency," Appl. Phys. Lett. **89**, 053519 (2006).

[106] S. Mou, J.V. Li, and S.L. Chuang, "Quantum efficiency analysis of InAs-GaSb type-II superlattice photodiodes," J. Quantum Electron. **45**, 737 (2009).

[107] L. Höglund, A. Soibel, D.Z-Y. Ting, A. Khoshakhlagh, C.J. Hill, and S.D. Gunapala, "Minority carrier lifetimes and photoluminescence studies of antimony-based superlattices," Proc. SPIE **8511**, 851106 (2012).

[108] P. Martyniuk, J. Wróbel, E. Plis, P. Madejczyk, W. Gawron, A. Kowalewski, S. Krishna, A. Rogalski, "Modeling of midwavelength infrared InAs/GaSb type-II superlattice detectors," Opt. Eng. **52**, 061307 (2013).

[109] J. Piotrowski, "Uncooled operation of IR photodetectors" Opto-Electron. Rev. **12**, 111-122 (2004).

[110] B.V. Olson, L.M. Murray, J.P. Prineas, M. Flatte, J.T. Olesberg, and T.F. Boggess, "All-optical measurement of vertical charge carrier transport in mid-wave infrared InAs/GaSb type-II superlattices," Appl. Phys. Lett. **102**, 202101 (2013).

[111] O.D. Miller, "Photonic Design: From Fundamental Solar Cell Physics to Computational Inverse Design," Ph.D dissertation, University of California, Berkeley (2012).

[112] B.A. Foreman, "Elimination of spurious solutions from eight-band kp theory," Phys. Rev. B **56**, R12748-R12751 (1997).

[113] F. Rossi, *Theory of semiconductor quantum devices microscopic modeling and simulation strategies* (Springer, Berlin 2011).

[114] H. Lotfi, R.T. Hinkey, L. Li, R.Q. Yang, J.F. Klem, and M.B. Johnson, "Narrow-bandgap photovoltaic devices operating at room temperature and above with high open-circuit voltage," Appl. Phys. Lett. **102**, 211103 (2013).

[115] R. Winston, J. Minan, and P. Benitez, Nonimaging Optics. Boston, MA, USA: Elsevier, 2005.

[116] A.M. Hoang, G. Chen, A. Haddadi, S.A. Pour, and M. Razeghi, "Demonstration of short wavlenegth infrared photodiodes based on type-II InAs/GaSb/AlSb superlattices," Appl. Phys. Lett. 100, 211101 (2012).

[117] C.A. Wang, H.K. Choi, S.L. Ransom, G.W. Charache, L.R. Danielson, and D.M. Depoy, "High quantum-efficiency 0.5 eV GaInAsSb/GaSb thermophotovoltaic devices," Appl. Phys. Lett. **75**, 1305-1307 (1999).

[118] P.C. Klipstein, Y. Gross, D. Aronov, M. ben Ezra, E. Berkowicz, Y. Cohen, R. Fraenkel, A. Glozman, S. Grossman, O. Klin, I. Lukomsky, T. Markowitz, L. Shkedy, I. Shtrichman, N. Snapi, A. Tuito, M. Yassen, and E. Weiss, "Low SWaP MWIR detector based on XBn Focal Plane Array," Proc. SPIE 8404, 87041S (2013).

[119] Y.P. Varshni, "Temperature dependence of the energy gap in semiconductors," Physica (Amsterdam) **34**, 149 (1967).

[120] J. Pedrazzani, "Characteristics of InAs-Based nBn Photodetectors Grown by Molecular Beam Epitaxy," Ph.D. Dissertation, University of Rochester (2010).

[121] S. Mou, "Theory and experiment of antimony-based type-II superlattice infrared photodetectors," Ph.D Dissertation, University of Illinois Urbana-Champaign (2007).

[122] L.F.J. Piper, T.D. Veal, M.J. Lowe, C.F. McConville, "Electron depletion at InAs free surfaces: Doping-induced acceptorlike gap states," Phys. Rev. B **73**, 195321 (2006).

[123] J.A. Nolde, R. Stine, E.M. Jackson, C.L. Canedy, I. Vurgaftman, S.I. Maximenko, C.A. Affouda, M. Gonzalez, E.H. Aifer, and J.R. Meyer, "Effect of the oxide-semiconductor interface on the passivation of hybrid type-II superlattice long-wave infrared photodiodes," Proc SPIE **7945**, 79451Y (2011).

[124] M. Razeghi, A. Haddadi, A.M. Hoang, E.K. Huang, G. Chen, S. Bogdanov, S.R. Darvish, F. Callewaert, and R. McClintock, "Advances in antimonide-based type-II superlattices for infrared detection and imaging at Center for Quantum Devices," Inf. Phys. Tech. **59**, 41-52 (2013).

[125] M.J. Hobbs, F. Bastiman, C.H. Tan, J.P.R. David, S. Krishna, and E. Plis, "Uncooled MWIR InAs/GaSb type-II superlattice grown on GaAs substrate," Proc. SPIE **8899**, 889906 (2013).

[126] N. Gautum, S. Myers, A.V. Barve, B. Klein, E.P. Smith, D.R. Rhinger, L.R. Dawson, and S. Krishna, "High operating temperature interband cascade midwave infrared detector based on type-II InAs/GaSb strained layer superlattice," Appl. Phys. Lett. **101**, 021106 (2012).

[127] L. Li, H. Lotfi, L.Lei, et. al., unpublished results.

[128] P.-Y. Emelie, "HgCdTe Auger-Suppressed Infrared Detectors Under Non-Equilibrium Operation," Ph.D Disseration, University of Michigan (2009).

[129] B.-M. Nguyen, D. Hoffman, Y. Wei, P.-Y. Delaunay, A. Hood, and M. Razeghi, "Very high quantum efficiency in type-II InAs/GaSb superlattice photodiode with cutoff wavelength of 12 μm," Appl. Phys. Lett. **90**, 231108 (2007).

[130] S.P. Svensson, D. Donetsky, D. Wang, P. Maloney, and G. Belenky, “Carrier lifetime measurements in InAs/GaSb strained layer superlattice structures,” Proc. SPIE **7660**, 76601V (2010).

[131] K.A. Milton, Mathematical Methods of Physics, Physics 5013 lecture notes (2006).

Appendix A: Derivation of Shockley-Ramo Experession for Instantaneous Current Under Fixed Potentials

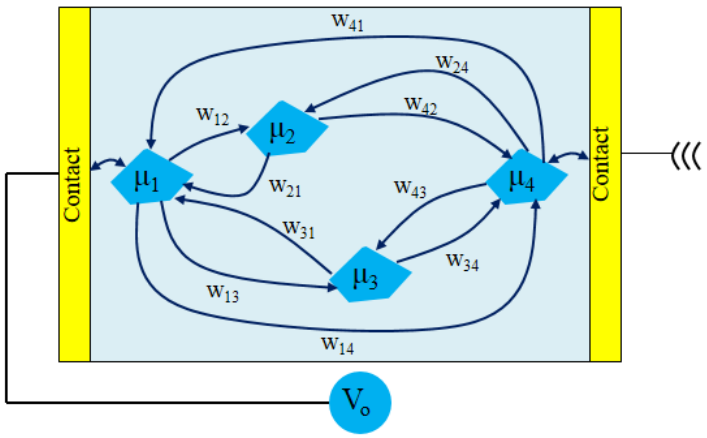

Figure A.1: Schematic of an arbitrary semiconductor device where electron transport can be modeled as thermalized reservoirs exchanging electrons.

Let us consider a system such as that in Fig. A.1. The system is composed of a semiconductor structure between two metal conductors, which we will denote as conductor 1 and conductor 2. Conductor 1 has a charge of q and voltage V. Conductor 2 is grounded. The electrons in the device interior are grouped into different reservoirs, each with a separate chemical potential, denoted as μ_i for the i^{th} reservoir. The amount of work to assemble this configuration at constant temperature and pressure is given by the Gibbs' free energy:

$$G = qV + \sum_i n_i \mu_i, \tag{A.1}$$

where n_i is the total number of electrons in the i^{th} reservoir. For now, we assume that all quantities in Eq. A.1 are able to vary with time. The inducement of signal in the external circuit is a two-step process. First, the environment (composed of the lattice, local electromagnetic field, etc…) induces an electron to transition from one reservoir to another. This transition event obviously causes a change in the total Gibbs' free energy. However, the total Gibbs' free energy of the system should be constant with time. Thus, any change in the Gibbs' free energy of the internal electrons will be compensated by the inducement of charge on conductor 1 and

energy transferred to or from the external circuit to ensure that $dG/dt=0$. The assertion that the Gibbs' free energy should be constant with time comes from the same principle as Green's reciprocity theorem [53], which was used in the original proof by Shockley [23]. The total power delivered to the circuit due to the inducement of charge on conductor 1 is equal to $-V\,dq/dt$ and can be expressed as:

$$P_{circ} = \sum_i (n_i \dot{\mu}_i + n_i \dot{\mu}_i) + q\dot{V}, \tag{A.2}$$

where a dot over a quantity indicates its time-derivative. In this expression, we have allowed all the relevant quantities to fluctuate with time. Henceforth, the time-dependence of quantities will be explicitly indicated. Also, we will now assume that the voltage of conductor 1 is fixed to the value V_o, and that consequently there is also no time-variation in the chemical potentials. The value of $\dot{n}_i(t)$ can be written as:

$$\dot{n}_i(t) = \sum_j \left[w_{ji}(t) - w_{ij}(t)\right]. \tag{A.3}$$

This leads to the following expression for instantaneous power under constant potential:

$$P_{circ}(t) = \sum_{i,j} w_{ij}(t)(\mu_j - \mu_i), \tag{A.4}$$

which is seen to be similar to the equation for the Joule power dissipation across a resistor. The instantaneous current flowing in the circuit can be found by simply dividing $P_{circ}(t)$ by V_o:

$$i(t) = e\sum_{i,j} w_{ij}(t)\alpha_{ij}, \tag{A.5}$$

where the definition of α_{ij} is the same as in the text. This result indicates that a charge flow through the external circuit occurs when there is energy transfer between the internal electrons and the environment. Thus, we preserve the physics of the original formulation, which found

that the instantaneous current at a given time depended on the work done on the internal electrons of the device

Appendix B: Derivation of Green's Function Solution, Boundary Conditions, and Carrier Collection Probability

Here it is shown how to solve for the diffusion equation Green's function $G_m(x,x')$ and the corresponding carrier collection probability $f_c(x)$ needed to calculate the current flow in the m^{th} stage. The solution method for the Green's function follows the techniques of Refs. 100 and 131. For simplicity, we will drop the *m* subscript indicating the stage. We assign the coordinates x=0 to be the edge of the m^{th} absorber closest to the top of the structure. We denote the absorber thickness as *d*, so the absorber extends from x=0 to x=*d*. The equation for the minority carrier density in the absorber under an arbitrary generation profile $g(x)$ is given as:

$$\left[\frac{d^2}{dx^2} - \frac{1}{L_n^2}\right] n(x) = -\frac{g(x)}{D_n}, \tag{B.1}$$

We can find the spatial profile of the minority carrier density for a given generation profile by solving for the Green's function, governed by the equation:

$$\left[\frac{d^2}{dx^2} - \frac{1}{L_n^2}\right] G(x,x') = \delta(x-x'), \tag{B.2}$$

To find the relationship between $n(x)$ and $G(x,x')$, we multiply Eq. B.1 by $G(x,x')$ and Eq. B.2 by $n(x)$. We integrate the difference of the two equations over the length of the absorber:

$$\begin{aligned} &\int_0^d dx' \left[G(x,x') \frac{d^2}{dx'^2} n(x') - \frac{n(x')d^2}{dx'^2} G(x,x') \right] \\ &\qquad = -\int_0^d dx' G(x,x') \frac{g(x')}{D_n} - \int_0^d dx' n(x') \delta(x-x'), \end{aligned} \tag{B.3}$$

where we have utilized the reciprocity relationship for the Green's function $G(x,x') = G(x',x)$. Applying the one-dimension Green's theorem and rearranging terms, we can evaluate $n(x)$ as:

$$n(x) = -\int_0^d dx' G(x,x') \frac{g(x')}{D_n} + \left[n(x') \frac{d}{dx'} G(x,x') + G(x,x') \frac{d}{dx'} n(x') \right]_{x'=0}^{x'=d} , \tag{B.4}$$

The boundary conditions for the carrier density are:

$$n(x)|_{x=0} = n_o e^{\beta_m eV/k_b T} , \tag{B.5}$$

at x=0, and:

$$\left. \frac{dn(x)}{dx} \right|_{x=d} = -\frac{S_{eb}}{D_n} [n(d) - n_o] , \tag{B.6}$$

at x=d, as given in the text. Following the conventional approach, we chose the boundary conditions for the Green's function to be homogenous. With this choice, the types of boundary conditions for the Green's function (i.e. Dirichlet, Neumann, or mixed) are the same as that of the carrier density. The boundary conditions are:

$$G(x,x')\Big|_{x=0} = 0$$

$$\left[\frac{dG(x,x')}{dx'} + \frac{S_{eb}}{D_n} G(x,x') \right]_{x=d} = 0, \tag{B.7}$$

where we have again used the reciprocity relationship for $G(x,x')$ so that the boundary conditions are defined for x. With our choice of Green's function boundary conditions, the solution of $n(x)$ simplifies to:

$$n(x) = -n(x'=0) \left[\frac{d}{dx'} G(x,x') \right]_{x'=0} - n_o \frac{S_{eb}}{D_n} G(x,x')|_{x'=d} - \int_0^d dx' G(x,x') \frac{g(x')}{D_n} , \tag{B.8}$$

We can physically interpret the three terms on the right hand side of Eq. B.8 as the contributions to $n(x)$ from three separate sources. The first term represents carrier injection at $x'=0$, the second term represents carrier generation from the absorber-electron barrier interface at $x'=d$, and the third term gives the contribution from internal generation in the bulk of the absorber.

A closed-form expression for the Green's function can be found by solving Eq. B.2 with the boundary conditions of Eq. B.7. First, we must find general solutions for $G(x,x')$ in the regions $x<x'$ and $x>x'$, where the inhomogeneous term in Eq. B.2 is equal to zero. These general expressions are given as:

$$G_<(x,x') = C_1(x')\sinh\left(\frac{x}{L_n}\right) \qquad (x<x'),$$
$$G_<(x,x') = C_2(x')\left[e^{-(d-x)/L_n} + \frac{1+S_{eb}L_n/D_n}{1-S_{eb}L_n/D_n}e^{(d-x)/L_n}\right] \qquad (x<x'), \tag{B.9}$$

where $G_<(x,x')$ specifies the Green's function in the region where $x<x'$, and $G_>(x,x')$ specifies the Green's function in the region where $x>x'$. The functions $C_1(x')$ and $C_2(x')$ are arbitrary functions of x' that are determined by the matching conditions for the two solutions at $x=x'$. These matching conditions are found by integrating Eq. B.2 over an infinitesimal length centered at $x=x'$. They are given as:

$$\left[\frac{d}{dx}G_>(x,x') - \frac{d}{dx}G_<(x,x')\right]_{x=x'} = 1,$$
$$[G_>(x,x') - G_<(x,x')]_{x=x'} = 0 \tag{B.10}$$

Thus, we see that the Green's function is continuous across $x=x'$, but it's derivative is discontinuous. By applying the matching conditions and solving for $C_1(x')$ and $C_2(x')$, we obtain the Green's function in the two regions as:

$$G_<(x,x') = -L_n \sinh\left(\frac{x}{L_n}\right)\left[\frac{\cosh\left[\frac{(d-x')}{L_n}\right] + \left(\frac{S_{eb}L_n}{D_n}\right)\sinh\left[\frac{(d-x')}{L_n}\right]}{\cosh\left(\frac{d}{L_n}\right) + \left(\frac{S_{eb}L_n}{D_n}\right)\sinh\left(\frac{d}{L_n}\right)}\right],$$

$$G_<(x,x') = -L_n \sinh\left(\frac{x'}{L_n}\right)\left[\frac{\cosh\left[\frac{(d-x)}{L_n}\right] + \left(\frac{S_{eb}L_n}{D_n}\right)\sinh\left[\frac{(d-x)}{L_n}\right]}{\cosh\left(\frac{d}{L_n}\right) + \left(\frac{S_{eb}L_n}{D_n}\right)\sinh\left(\frac{d}{L_n}\right)}\right] \quad \text{(B.11)}$$

The total Green's function can be concisely expressed as:

$$G(x,x') = -L_n \sinh\left(\frac{x_<}{L_n}\right)\left[\frac{\cosh[(d-x_>)/L_n] + \left(\frac{S_{eb}L_n}{D_n}\right)\sinh[(d-x_>)/L_n]}{\cosh(d/L_n) + \left(\frac{S_{eb}L_n}{D_n}\right)\sinh(d/L_n)}\right], \quad \text{(B.12)}$$

where $x_<$ represents the lesser value of x and x' and $x_>$ represents the greater value. For the specific case where there is no illumination and the generation rate is just the spatially uniform thermal generation rate $g(x) = \Gamma_{th}$, the carrier distribution function is given by:

$$n(x) = n_o\left[1 + \frac{\cosh[(d-x)/L_n] + \left(\frac{S_{eb}L_n}{D_n}\right)\sinh[(d-x)/L_n]}{\cosh(d/L_n) + \left(\frac{S_{eb}L_n}{D_n}\right)\sinh(d/L_n)}\left(e^{eV/k_bT} - 1\right)\right], \quad \text{(B.13)}$$

It is now convenient to define a carrier collection probability $f_c(x)$, which gives the probability that a carrier generated at point x in the absorber will diffuse to the collection point at x=0 before recombining. It is defined as:

$$\Gamma = \int_0^d dx\, f_c(x) g(x), \quad \text{(B.14)}$$

where Γ is the total generation particle current in a stage that runs as a result of the carrier generation rate g(x). We reiterate that $g(x)$ is an arbitrary generation rate, so Eq. B.14 applies for both radiative and non-radiative generation. The relationship between f_c(x) and $G(x,x')$ can be found by considering the case of zero illumination, and is given by:

$$f_c = \left[-\frac{d}{dx}G(x,x')\right]_{x'=0}. \tag{B.15}$$

A sketch of the spatial dependence of both $|G(x,x')|$ and $f_c(x)$ is shown in Fig. B.1. In the calculation, the absorber length was set equal to the minority carrier diffusion length. We show the profile for the two extreme values of $S_{eb} = 0$ and $S_{eb} = \infty$. The dark carrier density is related to the carrier collection probability by:

$$n(x) = n_o\left[1 + f_c(x)\left(e^{\frac{eV}{k_bT}} - 1\right)\right], \tag{B.16}$$

which provides a simple and useful relationship for connecting the light and dark behavior of a device.

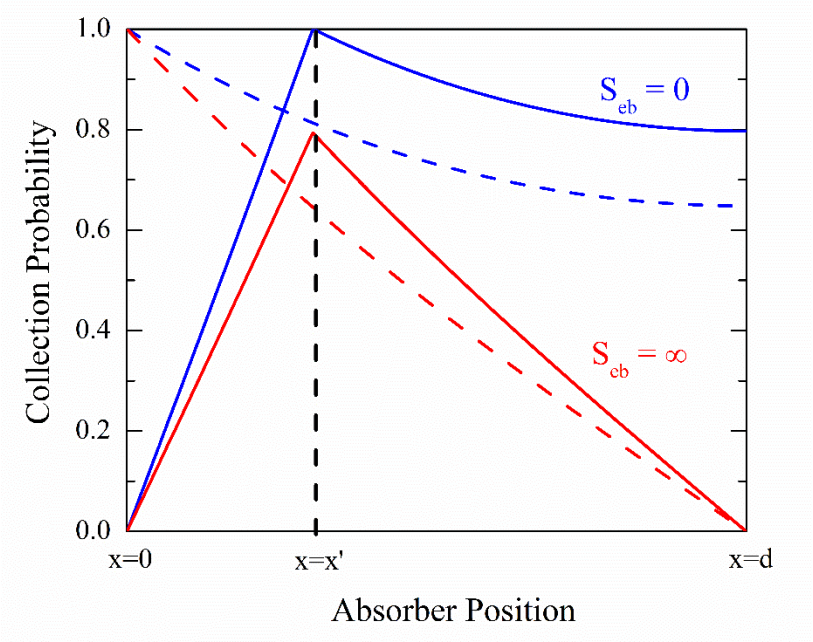

Figure B.1: Spatial dependence of Green's function and carrier collection probability across the absorber for the cases of S_{eb}=0 and S_{eb}=∞. The absorber length was set equal to the minority carrier diffusion length.

Appendix C: Activation Energy Database for MWIR Interband Cascade Infrared Photodetectors

This appendix summarizes the temperature-dependence of $(R_oA)^{-1}$ values for MWIR ICIP wafers grown and characterized in the time period of 2008-2013. This data was acquired by differentiating the measured current-voltage characteristics acquired under shielding. Details on the growth and design of each structure are indicated in Table C.1. Also displayed in the table are the absorber bandgaps at 80 K, which were estimated from the measured response, and the R_oA values measured at 80 K. Arrhenius plots showing the temperature-dependence of the measured $(R_oA)^{-1}$ values and the corresponding fits to Eq. 4.10 for the case of q=2 are shown in Figs. C.1 - C.11. The activation energies acquired from the fits are also shown in Table C1. The specific device from which the data was acquired is given in each figure, along with the temperature ranges over which the fitting was performed. To aid in making comparisons of the data of devices from different samples, all the $(R_oA)^{-1}$ data is plotted on the same logarithmic scale with limits from $1.0\text{x}10^{-10}$ $(\Omega\text{cm}^2)^{-1}$ to 100 $(\Omega\text{cm}^2)^{-1}$. The two solid lines in each plot represent the fitting to Eq. 4.10 at high and low temperatures. The dashed lines show the extrapolation of the high temperature $(R_oA)^{-1}$ dependence to low temperature. The difference between the dashed line and the low temperature data provides a guide for how strongly the low-temperature detector performance is influenced by leakage current. Devices which have a strong variation are believed to be strongly limited by leakage current at low temperatures. As noted in the text, with some exceptions such as R100, which had poor material quality, the trend in $(R_oA)^{-1}$ for longer-absorber (> 500 nm) devices tend to be more consistent across the entire temperature range than multiple-stage, short-absorber (< 250 nm) detectors. Notably, none of the short-absorber devices have a low-temperature activation energy greater than 100 meV.

Wafer	N_S	80 K E_g	Absorber Thickness	R_oA (80 K)	R_oA (300 K)	High Temp E_a	Low Temp. E_a
EB2700	7	0.24 eV	All 150 nm	$4.3\text{x}10^4$ Ωcm^2	0.11 Ωcm^2	149 meV	73 meV
EB2702	7	0.24 eV	All 150 nm	$4.2\text{x}10^4$ Ωcm^2	$7.7\text{x}10^{-2}$ Ωcm^2	164 meV	--
IQE11A	7	0.31 eV	All 150 nm	$8.6\text{x}10^6$ Ωcm^2	1.9 Ωcm^2	228 meV	73 meV
IQE12A	7	0.31 eV	All 150 nm	$2.7\text{x}10^6$ Ωcm^2	1.3 Ωcm^2	268 meV	52 meV
IQE13A	7	0.31 eV	All 250 nm	$1.5\text{x}10^7$ Ωcm^2	0.73 Ωcm^2	249 meV	63 meV
EB3337	7	0.31 eV	All 160 nm	$3.7\text{x}10^8$ Ωcm^2	3.0 Ωcm^2	253 meV	84 meV
R100	1	0.30 eV	1320 nm	$5.3\text{x}10^3$ Ωcm^2	$2.4\text{x}10^{-2}$ Ωcm^2	160 meV	25 meV
R101	1	0.29 eV	2320 nm	$2.2\text{x}10^6$ Ωcm^2	$2.1\text{x}10^{-2}$ Ωcm^2	149 meV	134 meV
R102	15	0.29 eV	All 160 nm	$1.5\text{x}10^5$ Ωcm^2	1.7 Ωcm^2	144 meV	52 meV
R103	2	0.29 eV	605 nm; 710 nm	$7.2\text{x}10^6$ Ωcm^2	$8.0\text{x}10^{-2}$ Ωcm^2	155 meV	128 meV
R104	3	0.29 eV	634 nm; 754 nm; 936 nm	$1.2\text{x}10^7$ Ωcm^2	$9.7\text{x}10^{-2}$ Ωcm^2	164 meV	131 meV

Table C.1: Summary of design details and temperature-dependence of R_oA for MWIR ICIPs characterized in time period of 2008-2013. .

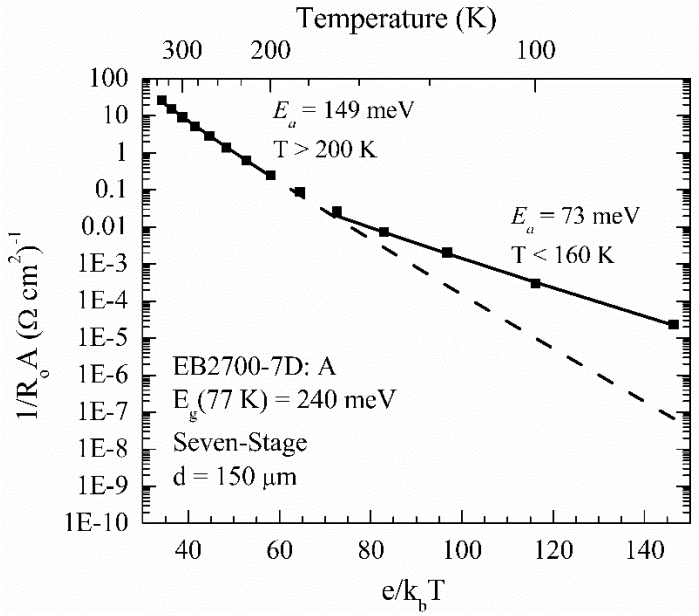

Figure C.1: Arrhenius plot of measured $(R_oA)^{-1}$ for a device from wafer EB2700. The data was originally published in Ref. 12. The two solid lines show fitting of the data to Eq. 4.10 in the temperature ranges of T > 200 K and T < 160. The dashed line shows the extrapolation of the $(R_oA)^{-1}$ behavior observed at high temperature to the whole temperature ranged studied.

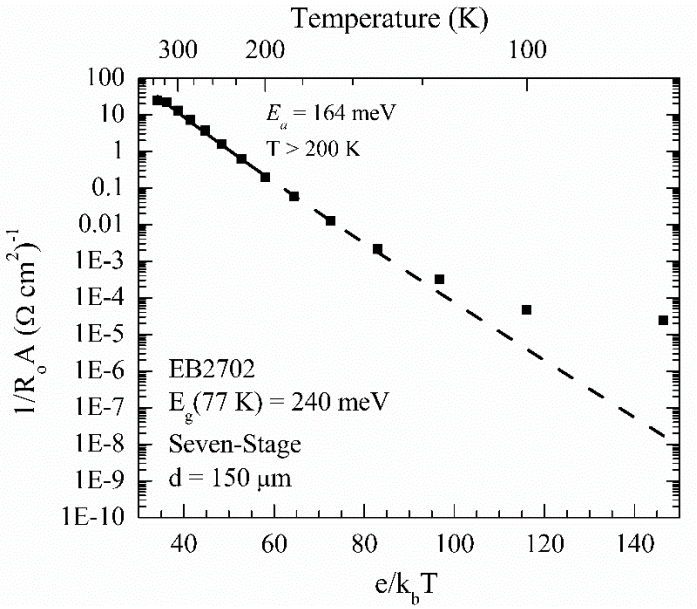

Figure C.2:Arrhenius plot of measured $(R_oA)^{-1}$ for a device from wafer EB2702. The data was originally published in Ref. 12. The solid line shows fitting of the data acquired at temepratures above 200 K to Eq. 4.10. The dashed line shows the extrapolation of the $(R_oA)^{-1}$ behavior observed at high temperature to the whole temperature ranged studied.

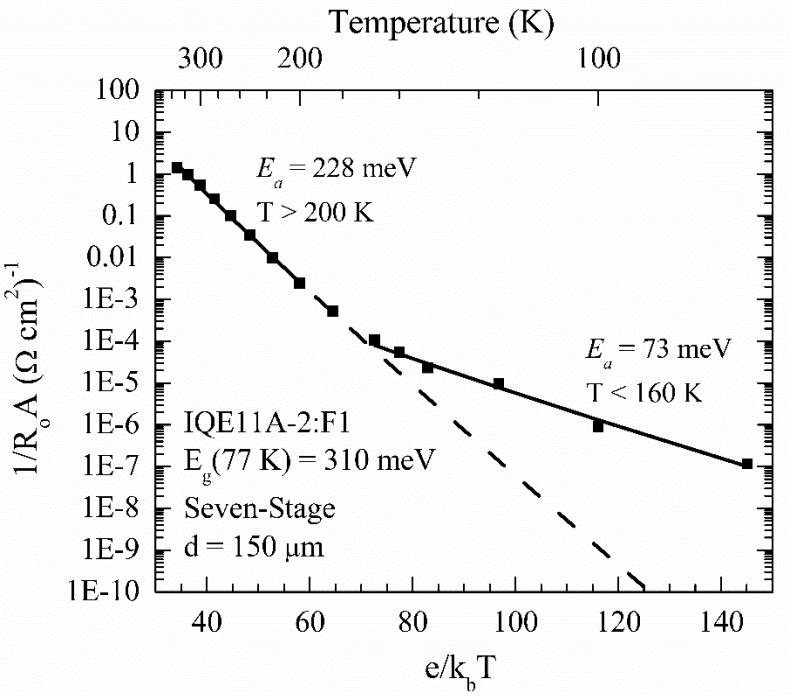

Figure C.3: Arrhenius plot of measured $(R_oA)^{-1}$ for a device from wafer IQE11A. The data was originally published in Ref. 14. The two solid lines show fitting of the data to Eq. 4.10 in the temperature ranges of T > 200 K and T < 160 K. The dashed line shows the extrapolation of the $(R_oA)^{-1}$ behavior observed at high temperature to the whole temperature ranged studied.

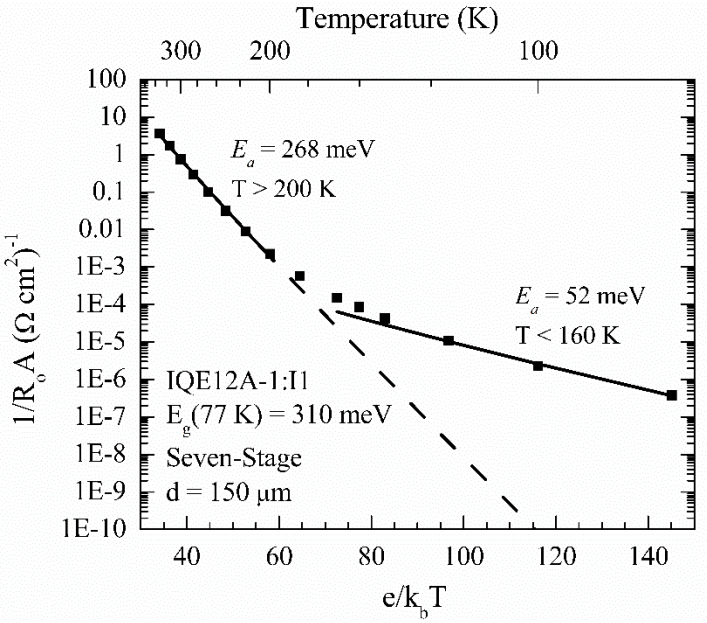

Figure C.4: Arrhenius plot of measured $(R_oA)^{-1}$ for a device from wafer IQE12A. The data was originally published in Ref. 14. The two solid lines show fitting of the data to Eq. 4.10 in the temperature ranges of T > 200 K and T < 160 K. The dashed line shows the extrapolation of the $(R_oA)^{-1}$ behavior observed at high temperature to the whole temperature ranged studied.

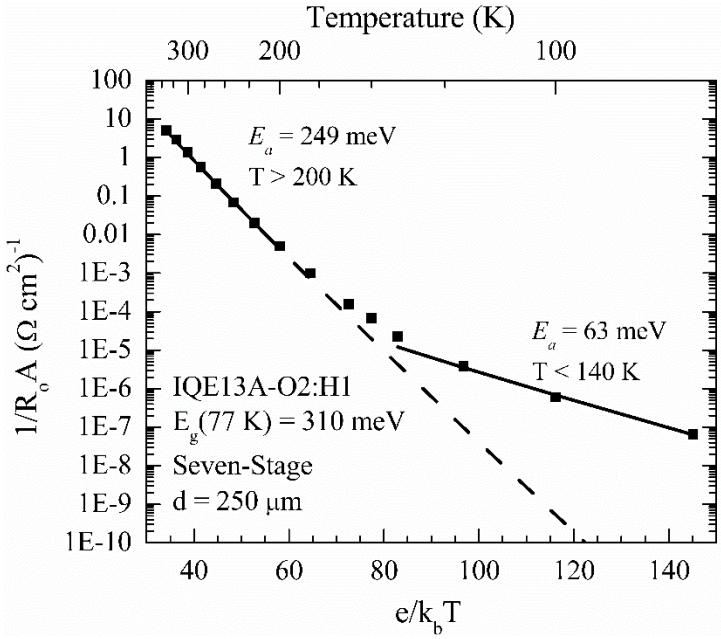

Figure C.5: Arrhenius plot of measured $(R_oA)^{-1}$ for a device from wafer IQE13A. The data was originally published in Ref. 14. The two solid lines show fitting of the data to Eq. 4.10 in the temperature ranges of T > 200 K and T < 140 K. The dashed line shows the extrapolation of the $(R_oA)^{-1}$ behavior observed at high temperature to the whole temperature ranged studied.

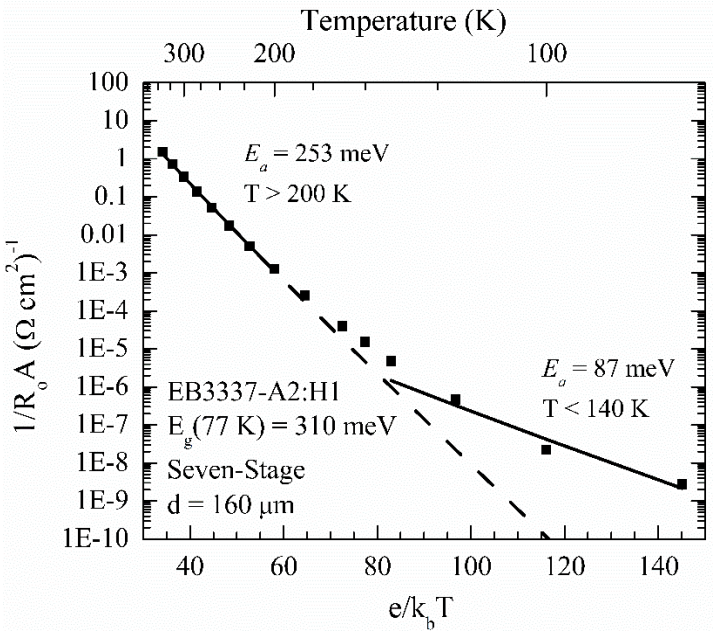

Figure C.6: Arrhenius plot of measured $(R_oA)^{-1}$ for a device from wafer EB3337. The two solid lines show fitting of the data to Eq. 4.10 in the temperature ranges of T > 200 K and T < 140 K. The dashed line shows the extrapolation of the $(R_oA)^{-1}$ behavior observed at high temperature to the whole temperature ranged studied.

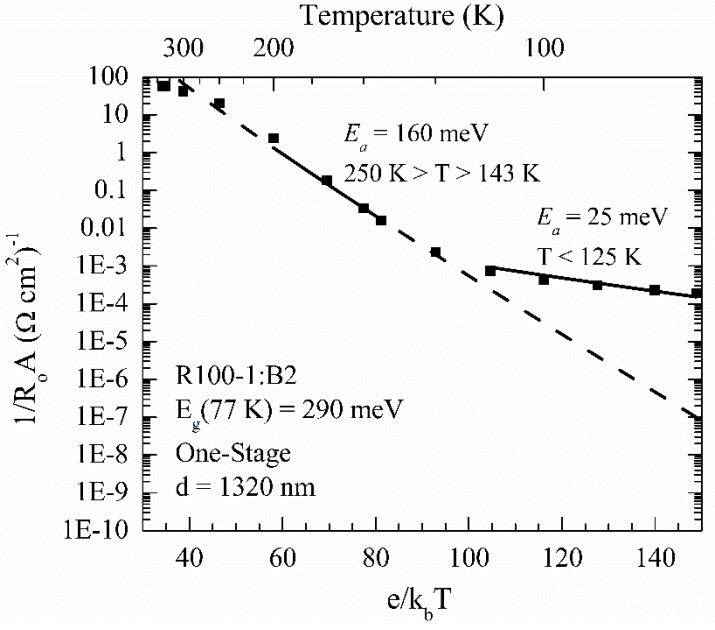

Figure C.6: Arrhenius plot of measured $(R_oA)^{-1}$ for a device from wafer R100. The two solid lines show fitting of the data to Eq. 4.10 in the temperature ranges of 250 K > T > 143 K and T < 125 K. The dashed line shows the extrapolation of the $(R_oA)^{-1}$ behavior observed at high temperature to the whole temperature ranged studied.

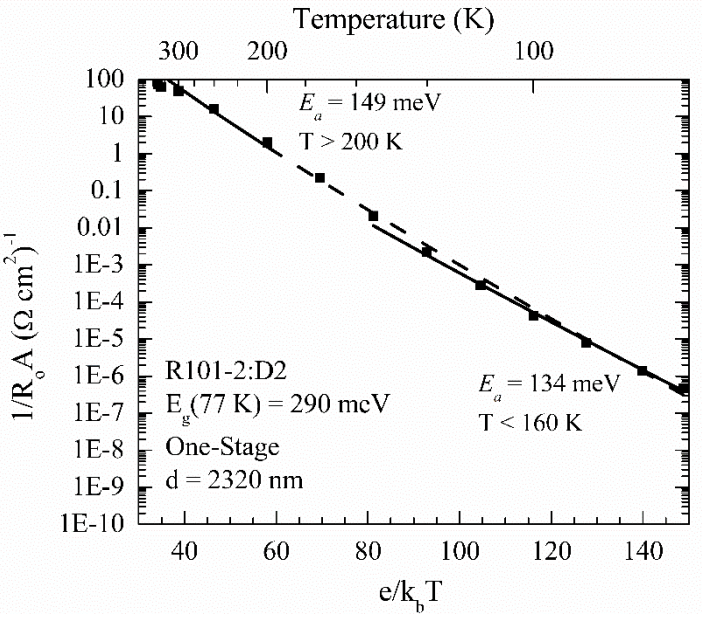

Figure C.7: Arrhenius plot of measured $(R_oA)^{-1}$ for a device from wafer R101. The two solid lines show fitting of the data to Eq. 4.10 in the temperature ranges of T > 200 K and T < 160 K. The dashed line shows the extrapolation of the $(R_oA)^{-1}$ behavior observed at high temperature to the whole temperature ranged studied.

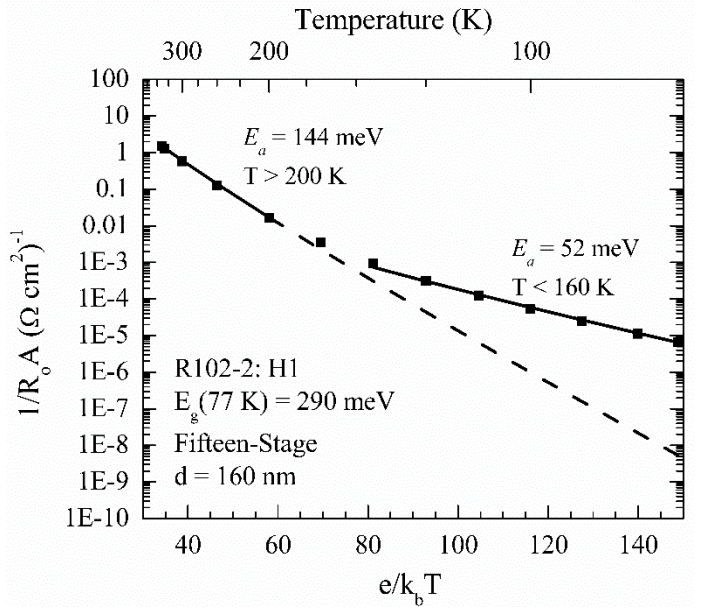

Figure C.8: Arrhenius plot of measured $(R_oA)^{-1}$ for a device from wafer R102. The two solid lines show fitting of the data to Eq. 4.10 in the temperature ranges of T > 200 K and T < 160 K. The dashed line shows the extrapolation of the $(R_oA)^{-1}$ behavior observed at high temperature to the whole temperature ranged studied.

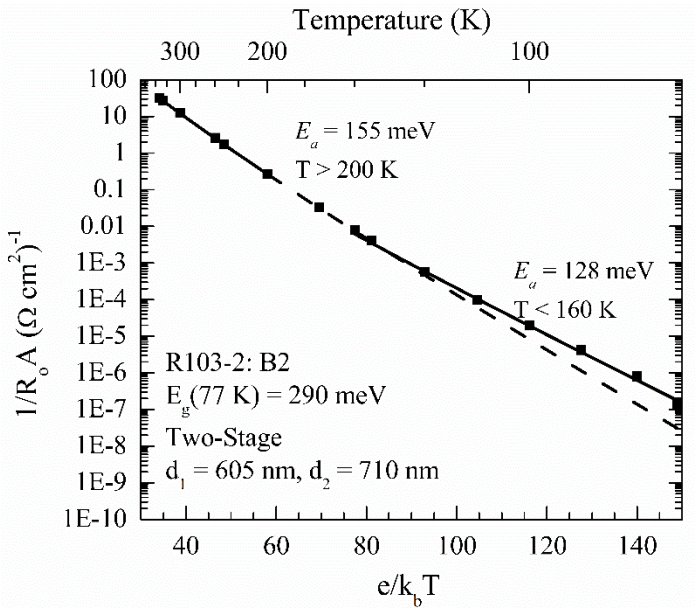

Figure C.9: Arrhenius plot of measured $(R_oA)^{-1}$ for a device from wafer R103. The two solid lines show fitting of the data to Eq. 4.10 in the temperature ranges of T > 200 K and T < 160 K. The dashed line shows the extrapolation of the $(R_oA)^{-1}$ behavior observed at high temperature to the whole temperature ranged studied.

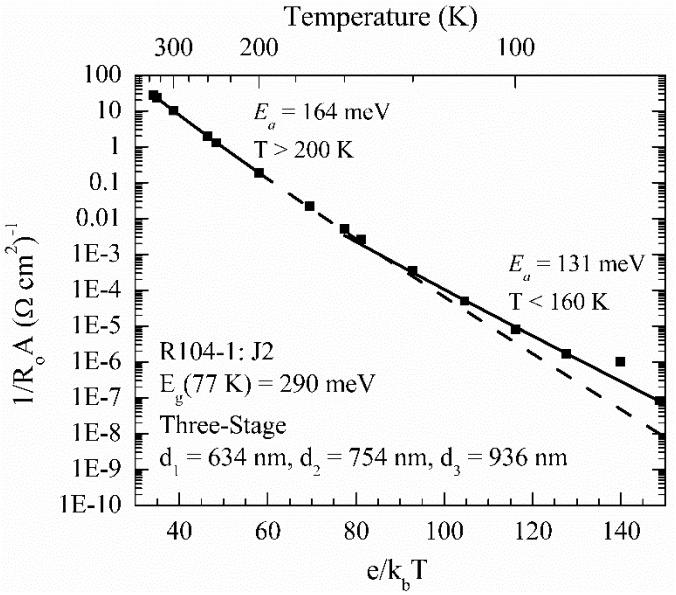

Figure C.10: Arrhenius plot of measured $(R_oA)^{-1}$ for a device from wafer R104. The two solid lines show fitting of the data to Eq. 4.10 in the temperature ranges of T > 200 K and T < 160 K. The dashed line shows the extrapolation of the $(R_oA)^{-1}$ behavior observed at high temperature to the whole temperature ranged studied.